

# **DETERMINATION OF COMPOSITION FLUCTUATIONS AND THEIR INFLUENCES ON PROPERTIES OF SOME PZT CERAMICS**

A Thesis Submitted  
in Partial Fulfilment of the Requirements  
for the Degree of

**MASTER OF TECHNOLOGY**

*by*

**SAMBIT KUMAR SAHA**

*to the*

**MATERIALS SCIENCE PROGRAMME  
INDIAN INSTITUTE OF TECHNOLOGY, KANPUR**

**AUGUST, 1990**

09 APR 1991

MSP-1990-M-SAM-DET

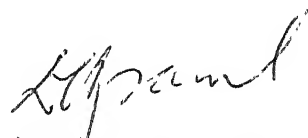
CENTRAL LIBRARY  
INDIAN KANPUR

Acc. No. A.110682

## CERTIFICATE

This is to certify that this work on 'DETERMINATION OF COMPOSITION FLUCTUATIONS AND THEIR INFLUENCES ON PROPERTIES OF SOME PET CERAMICS' by Sambit K. Saha has been carried out under my supervision and that this has not been submitted elsewhere for a degree.

August 1990.



(D.C. Agrawal)  
Professor

Materials Science Programme  
Indian Institute of Technology  
Kanpur

*Dedicated to my sister , Sanghamitra*

*" Queen of her species ".*



## ACKNOWLEDGEMENTS

I express my profound gratitude to Prof. D.C. Agrawal for his excellent guidance throughout the course of my work.

I am extremely grateful to Dr. K.M. Rai for allowing me to have free access to all the facilities for piezoelectric measurement.

I also express my appreciation for the help extended to me by Mr. B. Sharma, Mr. B.K. Jain, Mr. U.S. Singh, Mr. P.K. Pal and Mr. U.S. Lal of ACMS and Mr. Rehman of the Dept of Metallurgical Engineering.

I warmly thank Shiulidi, Santanuda, Manavendra and Sanjoy for the 'n' number of ways in which they helped me in my work.

A lot of thanks are also due to Rangan, Moma, Subhasish Caumyenda, Mimda, Kak and Bhaskar for providing invaluable assistance to assemble this thesis.

I also thank Mr. S.N. Pradhan for converting the scrawls in my manuscript to neat typewritten work along with Sumit and Murlidharan who did a lot of hard work correcting the proofs.

Among my friends who I have not already thanked; Ramani, Ajai, Pramod and Sanjay J. deserve special mention for making the laboratory so lively and cheerful.

## CONTENTS

List of Tables		i
List of Figures		iv
Abstract		ix
CHAPTER 1	Introduction to piezoelectricity and piezoelectric materials	1
1.1	Piezoelectricity.	1
1.2	Piezoelectric crystals and the Ferroelectric Subclass.	2
1.3	The Antiferrelectricity Concept	4
1.4	The piezoelectric effect in ceramics.	5
1.5	Piezoelectric constants.	8
1.6	The Lead-Zirconate-Titanate system.	14
1.7	Mechanical properties of the Lead-Zirconate-Titanate system.	20
CHAPTER 2	Effect of processing parameters on the microstructure and composition fluctuations of Pb(Ti,Zr)O <sub>3</sub> compositions.	33
CHAPTER 3	Determination of inhomogeneity in Lead-Zirconate-Titanate Ceramics by X-ray diffraction.	47
3.1	Introduction .	47
3.2	Measure of line width.	49
3.3	Shape of the X-ray line profile.	50

3.4	Correction due to the spectral width of the incident beam.	52
3.5	The powder diffractometer.	53
3.6	The instrumental weight functions.	56
3.7	Correction due to instrumental factors.	60
CHAPTER 4	The present work.	70
CHAPTER 5	Experimental procedure.	72
5.1	Sample preparation .	72
A.	Raw materials	72
B.	Preparation of packing powder.	73
C.	Preparation of lead-zirconate-titanate samples.	74
5.2	X-ray diffraction analysis.	77
A.	Measurement of lattice parameters	78
B.	Measurement of composition fluctuation.	80
5.3	Scanning electron microscopy.	81
5.4	Piezoelectric property measurements	82
A.	Measurement of Strain Coefficient( $d_{33}$ )	82
B.	Measurement of resonance and antiresonance frequencies.	84
5.5	Vickers Hardness	84
5.6	Density and Porosity Measurement	85
CHAPTER 6	Results and discussions.	89
6.1	X-ray diffraction analysis.	129

A.	Lattice parameters.	129
B.	Composition fluctuation .	129
6.2	Scanning electron microscopy.	131
6.3	Piezoelectric properties.	133
A.	The strain coefficient, $d_{33}$ .	133
B.	Resonance and antiresonance frequencies.	134
6.4	Density and porosity.	135
6.5	Vickers hardness.	136
CHAPTER 7	Conclusions and suggestions for further work.	138
REFERENCES		140
APPENDIX		145

## LIST OF TABLES

Table	1.1	Fraction of single crystal polarisation and distortion for various phases on application of poling fields.	9
Table	5.1 A.	Details of chemicals used in experiments.	72
	5.1 B.	Chemical composition of atmosphere powder .	73
	5.1 C.	Chemical composition of fabricated PZT specimens.	74
	5.1 D.	Calcination and sintering conditions for the specimen sets.	75
	5.2	Conditions of operation for X-ray diffraction.	78
Table	6.1 A.		
	i)	Lattice parameters of PZT specimens calcined at various temperatures.	90
	ii)	Lattice parameters of PZT specimens calcined at various time.	91
	iii)	Lattice parameters of PZT specimens sintered at various temperatures.	92
	iv)	Lattice parameters of PZT specimens sintered at various time.	93
	6.1 B.		
	i)	Composition fluctuation of specimens calcined at various temperatures.	94

ii)	Composition fluctuation of specimens calcined at various time.	94
iii)	Composition fluctuation of specimens sintered at various temperatures.	95
iv)	Composition fluctuation of specimens sintered at various time.	95
6.2		
i)	Average grain diameters of specimens calcined at various temperatures.	96
ii)	Average grain diameters of specimens calcined at various time.	96
iii)	Average grain diameter of specimens sintered at various temperatures.	97
iv)	Average grain diameter of specimens sintered at various time.	97
6.3		
i)	Strain coefficient of specimens calcined at various temperatures.	98
ii)	Strain coefficient of specimens calcined at various time.	98
iii)	Strain coefficient of specimens sintered at various temperatures.	99
iv)	Strain coefficient of specimens sintered at various time.	99
6.4		
i)	Density and porosity of specimens calcined at various temperatures.	100
ii)	Density and porosity of specimens calcined at various time.	100

iii)	Density and porosity of specimens sintered at various temperatures.	101
iv)	Density and porosity of specimens sintered for various time.	101
6.5		
i)	Vickers hardness data of specimens calcined at various temperatures	102
ii)	Vickers hardness data of specimens calcined for various time.	102
iii)	Vickers hardness data of specimens sintered at various temperatures.	103
iv)	Vickers hardness data of specimens sintered for various time.	103

## LIST OF FIGURES

<u>Figures</u>		<u>Page</u>
Fig. 1.1	Interrelationships of piezoelectrics and subgroups on the basis of internal crystal symmetry.	25
Fig. 1.2	The perovskite structure as typified by $\text{BaTiO}_3$ above its Curie point.	26
Fig. 1.3	Lattice parameters of $\text{BaTiO}_3$ as function of temperature.	27
Fig. 1.4(a)	The equivalent circuit of a piezoelectric body near a fundamental resonance.	28
Fig. 1.4(b)	Reactance of a piezoelectric resonator compared with a capacitor of equal at low frequency. (dotted curve).	29
Fig. 1.5	$\text{PbTiO}_3$ - $\text{PbZrO}_3$ sub-solidus phase diagram.	29
Fig. 1.6	Unit cell distortion at room temperature for the $\text{PbTiO}_3$ - $\text{PbZrO}_3$ system.	30
Fig. 1.7	Phases in the system $\text{PbO-TiO}_2\text{-PbO:ZrO}_2$ as a function of firing temperature.	31
Fig. 1.8	Calcination reaction diagram for $\text{Pb}(\text{Zr}_{0.50}\text{Ti}_{0.50})\text{O}_3$ .	32
Fig. 2.1	Flowsheet of the mixed oxide (MO process) for fabrication of PZT ceramics.	42



Fig. 2.2	Laminar, unconnected pore in PZT microstructure.	43
Fig. 2.3	Laminar, connected pore in PZT microstructure.	44
Fig. 2.4	Porosity as a function of sintering temperature for unmodified and modified $\text{Pb}(\text{Zr}_{0.525}\text{Ti}_{0.475})\text{O}_3$ solid solutions.	45
Fig. 2.5	Lead oxide activity as a function of reciprocal temperature.	46
Fig. 3.1	Relation between lattice constants and composition of $\text{Pb}(\text{Zr}_x\text{Ti}_{1-x})\text{O}_3$ .	63
Fig. 3.2	Line breadth measures of diffraction profiles.	63
Fig. 3.3	Angular separation of the $K\alpha$ doublet as a function of $2\theta$ for three common radiations.	64
Fig. 3.4	Curves for correcting line breadths for $K\alpha$ -doublet broadening.	65
Fig. 3.5	Parafocussing arrangement used in the powder diffractometer.	66
Fig. 3.6	Optical arrangement in a diffractometer with a 'line' X-ray source and soller slits to limit axial divergence.	67
Fig. 3.7	Instrumental weight functions for diffractometers employing (A) low resolution and (B) high resolution geometry computed for $2\theta = 24^\circ$ $\mu = 34\text{cm}^{-1}$ .	68
Fig. 3.8	Curves for correcting X-ray diffractometer line breadths due to instrumental broadening.	69

Fig. 5.1(a)	Crucible assembly during calcination.	87
Fig. 5.1(b)	Crucible assembly during sintering.	87
Fig. 5.2	Fixture used for poling PZT specimens.	88
Fig. 6.1	XRD plot of $\text{Pb}(\text{Zr}_{0.5}\text{Ti}_{0.5})\text{O}_3$ from $2\theta = 20^\circ$ to $2\theta = 70^\circ$ .	104
Fig. 6.2	XRD plot of $\text{Pb}(\text{Zr}_{0.5}\text{Ti}_{0.5})\text{O}_3$ at $0.6^\circ/\text{min}$ scan	105
Fig. 6.3	Scanning electron micrographs of PZT sample calcined at $760^\circ\text{C}/1$ hr. and sintered at $1260^\circ\text{C}/1$ hr.	106
Fig. 6.4	Scanning electron micrograph of PZT sample calcined at $860^\circ\text{C}/1$ hr. and sintered at $1260^\circ\text{C}/1$ hr.	106
Fig. 6.5	Scanning electron micrograph of PZT sample calcined at $860^\circ\text{C}/1$ hr. and sintered for 1 hr sintering temperatures a) $1100^\circ\text{C}$ b) $1260^\circ\text{C}$ c) $1350^\circ\text{C}$ .	107
Fig. 6.6	Scanning electron micrographs of PZT samples calcined at $860^\circ\text{C}/1$ hr and sintered at $1260^\circ\text{C}$ for a) 1 hr. b) 4 hr.	108
Fig. 6.7	Scanning electron micrograph of PZT samples calcined at $860^\circ\text{C}/1$ hr. and sintered at $1260^\circ\text{C}$ for a) 1 hr. b) 7 hr.	109
Fig. 6.8	Plot from Impedance analyser showing reactance as a function of frequency.	110
Fig. 6.9	Effect of calcination and sintering times on the $C_T/a_T$ axial ratio.	111
Fig. 6.10	Effect of calcination and sintering temperatures on the $C_T/a_T$ axial ratio.	112

Fig. 6.11	Plot of $\beta \cos \theta$ vs $\sin \theta$ for PZT samples calcined at various temperatures for 1 hr. and sintered at 1260°C/ 1 hr.	113
Fig. 6.12	Plot of $\beta \cos \theta$ vs $\sin \theta$ for PZT samples calcined for various times at 860°C and sintered at 1260°C/ 1 hr.	114
Fig. 6.13	Plot of $\beta \cos \theta$ vs $\sin \theta$ for PZT samples calcined at 860°C/ 1 hr. and sintered at various temperatures for 1 hr.	115
Fig. 6.14	Plot of $\beta \cos \theta$ vs $\sin \theta$ for PZT samples calcined at 860°C/ 1 hr. and sintered at 1260°C for various times.	116
Fig. 6.15	Effect of calcination and sintering times on the composition fluctuation of $\text{Pb}(\text{Zr}_{0.5}\text{Ti}_{0.5})\text{O}_3$ .	117
Fig. 5.16	Effect of calcination and sintering temperatures on the composition fluctuation of $\text{Pb}(\text{Zr}_{0.5}\text{Ti}_{0.5})\text{O}_3$ .	118
Fig. 6.17	Effect of calcination and sintering times on the piezoelectric strain coefficient of $\text{Pb}(\text{Zr}_{0.5}\text{Ti}_{0.5})\text{O}_3$ .	119
Fig. 6.18	Effect of calcination and sintering temperatures on the piezoelectric strain coefficient of $\text{Pb}(\text{Zr}_{0.5}\text{Ti}_{0.5})\text{O}_3$ .	120
Fig. 6.19	Variation of standard deviation of piezoelectric strain coefficient, $d_{33}$ as a function of composition fluctuation.	121

Fig. 6.20	Variation of piezoelectric strain coefficient, $d_{33}$ as a function of composition fluctuation.	122
Fig. 6.21	Effect of calcination and sintering times on the density of $\text{Pb}(\text{Zr}_{0.5}\text{Ti}_{0.5})\text{O}_3$ .	123
Fig. 6.22	Effect of calcination and sintering temperature on the density of $\text{Pb}(\text{Zr}_{0.5}\text{Ti}_{0.5})\text{O}_3$ .	124
Fig. 6.23	Effect of calcination and sintering times on the porosity of $\text{Pb}(\text{Zr}_{0.5}\text{Ti}_{0.5})\text{O}_3$ .	125
Fig. 6.24	Effect of calcination and sintering temperatures on the porosity of $\text{Pb}(\text{Zr}_{0.5}\text{Ti}_{0.5})\text{O}_3$ .	126
Fig. 6.25	Effect of calcination and sintering times on the Vickers hardness of $\text{Pb}(\text{Zr}_{0.5}\text{Ti}_{0.5})\text{O}_3$ .	127
Fig. 6.26	Effect of calcination and sintering temperatures on the Vickers hardness of $\text{Pb}(\text{Zr}_{0.5}\text{Ti}_{0.5})\text{O}_3$ .	128

## ABSTRACT

$\text{Pb}(\text{Zr}_x\text{Ti}_{1-x})\text{O}_3$  piezoelectric ceramic specimen sets with  $x=0.50$  were prepared by the mixed oxide route under various calcination and sintering conditions in the presence of a  $\text{ZrO}_2$  rich PZ+Z atmosphere powder (27 mole %  $\text{PbO}$  and 73 mole %  $\text{ZrO}_2$ ).

The composition fluctuation of each specimen set was measured, employing the X-ray line profile analysis technique. The fluctuation decreased from 16.71% to 3.84% and from 4.22% to 1.40% on increasing the calcination temperature from  $760^\circ\text{C}$  to  $960^\circ\text{C}$  (calcination time- 1 hr) and calcination time from 1 hr to 5 hrs (calcination temperature =  $860^\circ\text{C}$ ) respectively. The sintering temperature and time were  $1260^\circ\text{C}$  and 1 hr in each case. Increasing the sintering temperature from  $100^\circ\text{C}$  to  $1260^\circ\text{C}$  lowered the inhomogeneity from 26.6% to 4.22% but a higher sintering temperature of  $1350^\circ\text{C}$  increased the inhomogeneity to 21.2%. Increasing the sintering time from 1 hr to 7 hrs also increased the homogeneity from 4.22% to 33%. The apparent anomaly in the composition fluctuation data is due to zirconia precipitation from the PZT solid solution. Scanning electron micrographs of these specimens confirmed the precipitated Zirconia phase. Also each of the prepared specimens showed the existence of both

the tetragonal and rhombohedral phases.

The piezoelectric strain coefficients,  $d_{33}$  of these specimens were also determined. The values ranged from 114.7 to 177.3  $\text{CN}^{-1}$  with specimens of lower composition fluctuations showing better  $d_{33}$  values on the average. It was also observed that the fluctuations in the measured  $d_{33}$  values correlate well with the composition fluctuation.

The Vickers hardness increased from 5.7 to 114.29 and from 15.13 to 27.53 on increasing the calcination temperature from 760°C to 960°C and the calcination time from 1 to 5 hrs. Each of these sets was sintered at 1200°C for 1 hr. Thus with decrease in composition fluctuation, the Vickers hardness ( $H_V$ ) improved in this case. However samples which were sintered at high temperature (1350°C) or long periods (7 hrs) and which contained the highest amount of precipitated  $\text{ZrO}_2$  showed a partial recovery in hardness values inspite of their high composition fluctuation. This could have been possibly due to the strengthening action of precipitated  $\text{ZrO}_2$ .

## CHAPTER 1

### INTRODUCTION TO PIEZOELECTRICITY AND PIEZOELECTRIC MATERIALS

#### 1.1 Piezoelectricity:

Piezoelectricity is a property possessed by a select group of materials which literally means pressure electricity. Cady [1] defined it as 'electric polarisation produced by mechanical strain in crystals belonging to certain classes, the polarisation being proportional to the strain and changing sign with it'. Two effects are observed in piezoelectricity- the direct and the converse. The direct effect is the creation of an electric charge by the application of stress on the piezoelectric solid. The charge is proportional to the force, and is therefore of opposite sign for compression and tension. In terms of dielectric displacement ' $D$ ' (charge  $Q$  per unit area) and stress ' $T$ ' we may write

$$D = \frac{Q}{A} = dT \quad (d \text{ expressed in coulombs/Newton}) \dots (1.1)$$

The converse effect is manifested when an applied field ' $E$ ' produces a proportional strain ' $S$ ', expansion or contraction depending on the polarity.

$$S = dE \quad (d \text{ expressed in meters/volt}) \dots (1.2)$$

For both effects, the proportionality constant is the piezoelectric constant ' $d$ ' which is numerically identical in both cases.

$$d = \frac{D}{T} = \frac{S}{E} \quad \dots\dots (1.3)$$

## 1.2 Piezoelectric Crystals and the Ferroelectric Subclass:

The materials which show the piezoelectric phenomena belong to either of 20 specific classes of the 32 point groups into which all crystalline materials are divided. Each of the piezoelectric point groups lack a centre of symmetry. A further subgroup can be made, consisting of those ten classes which contain a unique polar axis ( an electric dipole moment) in the unstrained condition. This is the pyroelectric subclass, Fig. 1.1 summarises the inter relationship of piezoelectrics and subgroups on the basis of internal crystal symmetry.

To visualise piezoelectricity, it is useful to consider a crystal each unit cell of which has a dipole. A dipole results from a difference between the centre of the positive charges and the centre of the negative charges in a unit cell. In piezoelectric but non pyroelectric crystals the dipolar moments are arranged in several compensating directions such that there is no net crystal dipole. When a pressure is applied, one of the directions is favoured and a net crystal dipole is created. For example, in quartz a principal direction along which a pressure will generate a charge is the 'a' axis ( or 'X' axis). Because, there are three such axes, symmetrically spaced  $120^\circ$  apart in a plane,



a uniform hydrostatic stress will affect each axis equally; the net charge will be zero. But a pressure applied to an individual 'a' axis compresses one dipole at the expense of the other two; charge is created.

Ferroelectricity is defined as reversibility in a polar crystal of the direction of the electric dipole by means of an applied electric field. Since it requires polarity in a crystal, it can occur only in the pyroelectric crystal classes. However the existence of a dipole does not guarantee that it can be reversed by an electric field; it could require a field greater than the breakdown field, or there might be an asymmetric and irreversible arrangement of the atoms. Tourmaline and hexagonal CdS are pyroelectric, but not ferroelectric. Thus we see that even if pyroelectrics are piezoelectric, pyroelectricity is a fundamental phenomenon distinct from piezoelectricity because it rests on different symmetry conditions and ferroelectricity is an empirical distinction between one type of pyroelectric crystal and another on the basis of experimental observation of the reversibility of dipoles by means of an external electric field.

To allow the dipoles to change direction, the 'energy hump' between the two directional states must be low. This means that the non polar state is only slightly less stable, so that on raising the temperature above a certain critical value the material transforms to the

non polar form from the polar ferroelectric. This critical temperature ' $T_0$ ' is called the Curie temperature and above it the dielectric constant of the material obeys the Curie-Weiss law.

$$K-1 = \left( \frac{C}{T-T_0} \right) \quad \dots\dots (1.4)$$

Above the Curie temperature the material is said to exhibit paraelectric behaviour.

### 1.3 The Antiferroelectricity Concept:

A related term that should be defined at this point is antiferroelectricity. The concept rose when it was suspected that certain materials showing a high dielectric constant peak at the Curie temperature and obeying the Curie - Weiss law above it could be non-polar, rather than ferroelectric below the inversion temperature. Kittel [2] developed the theory of antiferroelectricity and defined an antiferroelectric to be a material whose subcells show a polar arrangement, but in which adjacent subcells are oppositely polarised, giving a net zero polarisation and a centre of symmetry. This is in direct contrast to the subcell arrangement in ferroelectric materials where each subcell in an individual domain is polarised in the same direction.

The high dielectric constant frequently associated with the antipolar arrangement made the concept of

antiferroelectricity useful. Jona . et al [3] recognised this and they stated that an antipolar crystal has free energy comparable to a polar crystal. The antiferroelectric crystal therefore like its ferroelectric counterpart obeys the Curie-Weiss law above the Curie temperature. Experimental evidence on  $\text{PbZrO}_3$ , and possibly other antiferroelectrics as well have shown that the compensating antipolar arrangement need not exist in all three directions. In  $\text{PbZrO}_3$ , the arrangement is antipolar in two directions, but a net polarity was reported, in the third direction [4] which is not switchable. Thus antiferroelectricity does not preclude the existence of a separate non-reversible dipole.

#### 1.4 The Piezoelectric effect in Ceramics:

A ceramic is an agglomeration of small crystals, fitted together in a random way. As a ceramic gets cooled from the high temperature paraelectric state to the ferroelectric state, the unit cell deforms usually with a lengthening in the direction of the polar axis. Intergranular stresses are minimised by the formation of domains, regions within each grain that have common orientation of the spontaneous dipole. The polarisation direction of domains are basically high temperature symmetry axes ( such as  $\langle 001 \rangle$ ,  $\langle 110 \rangle$  or  $\langle 111 \rangle$ ). Angles between the dipoles of adjacent domains are those between the symmetry axes, e.g.  $90^\circ$ ,  $180^\circ$ ,  $71^\circ$ , etc, modified slightly by the ferroelectric deformation. Crystallographically, domain structure

is a type of twinning.

The most important piezoelectric ceramics crystallise in the perovskite structure. This structure may be described as a simple cubic unit cell with a large cation (A) on the corners, a smaller cation (B) in the body center, and oxygens (O) in the centres of the faces (Fig. 1.2). The structure is a network of corner linked oxygen octahedra, with the smaller cation filling the octohedral holes and the largercation filling the dodecahedral holes [5]. A wide variety of cations can be substituted in the perovskite structure [6].The relationship

$$t = (R_A + R_O) / \sqrt{2}(R_B + r_O) \quad \dots (1.5)$$

describes the ideal perovskite structure where  $t=1.0$  and  $R_A$ ,  $R_B$  and  $R_O$  indicate the ionic radius of the large cation, small cation and anion respectively. In practice those structures whose tolerance factor  $t=0.95$  to  $1.0$  are cubic; those with lower values are slightly distorted but non-ferroelectric, and those with ' $t$ ' over  $1.0$  tend to be ferroelectric. Polarisability of the ions is also an influential parameter. While considering this 'hardsphere' model of ions in contact, it is also necessary to consider that the bonding is not necessarily completely ionic [7].

Why the perovskite structure favours polarisation in the crystal lattice is best explained by

considering the case of Barium Titanate.  $\text{BaTiO}_3$ , on cooling through its Curie point, transforms from the cubic to the tetragonal structure by elongating along a cube axis ( Fig. 1.3). The other two cube axes contract. The centers of the positive and negative charges do not coincide thereafter local dipoles are created throughout the crystal promoting ferroelectricity. The unit cells in each domain align in the same direction giving rise to a net polarisation in the domain. As there are six possible directions for the polar tetragonal axis in the crystal, a rather complicated twinning or domain pattern results. The resulting domain pattern is a function of the stresses created at the Curie point, uncompensated surface charges and physical imperfections. To make the ceramic piezoelectric, an electric field must be applied to switch the polar axes of the crystallites in the ceramic ferroelectric to those direction allowed by symmetry which are nearest to that of the electric field . The poling treatment partially detwins the ceramic by eliminating much of the domain structure. Subsequently the ceramic resembles a pyroelectric single crystal by way of having a net dipole moment and responding linearly to an applied electric field or mechanical pressure like a single crystal as long as the field or pressure is well below that needed to switch the polar axis.

As the original crystallographic directions of the grains in the ceramic were oriented at random, it

is evident that the line-up of polar axes cannot be as perfect as in a single crystal of the material. A good indication of this dipole alignment is the measured value of polarisation. Baerwald,[8] assuming a random initial orientation of the grains and domains, and as complete a dipole alignment as is allowed by the grain orientations, had calculated the fraction of the single crystal polarization that can be realised in pseudocubic ceramics of various types. The results are shown in Table 1.1. With a larger number of allowable polar directions, the maximum deviation of the polar axis of a grain from the average polar direction will be smaller and the lowering of the polarisation will be minimised, assuming optimum alignment. The proportion of the single crystal distortion which is realised as strain in a fully oriented ceramic is also given in Table 1.1.

### 1.5 Piezoelectric Constants:

The piezoelectric constant ' $d$ ' which relates the dielectric displacement ' $D$ ' to the strain ' $S$ ' is probably the most fundamental for conveying the concept of piezoelectricity. Another constant which finds frequent usage in piezoelectric literature is ' $g$ '. It gives the field produced by a stress. The ' $g$ ' constant is related to the ' $d$ ' constant by the permittivity.

TABLE 1.1

FRACTION OF SINGLE CRYSTAL POLARISATION AND DISTORTION  
FOR VARIOUS PHASES ON APPLICATION OF POLING FIELDS.

Crystal Symmetry and polar axis	Number of equivalent directions	Fraction of single crystal polarisation that can be realised ideally.	Fraction of single crystal distortion that can be realised ideally
Tetragonal [001]	6	0.831	0.368
Orthorhombic [110]	12	0.912	Not calculated
Rhombohedral [111]	8	0.866	0.424

$$g = \frac{d}{\epsilon'} = \frac{d}{K\epsilon_0} \quad \dots (1.6)$$

'K' is the relative dielectric constant of the material.

Additional piezoelectric constants which are only occasionally used are 'e' which relates stress 'T' to field 'E', and 'h' which relates strain 'S' to field 'E'.

$$T = -eE \quad \dots (1.7)$$

$$E = -hS. \quad \dots (1.8)$$

Another constant which gives the measurement of the strength of a piezoelectric effect is the electromechanical coupling factor k. It is defined as

$$k = \frac{\text{electrical energy converted to mechanical energy}}{\text{input electrical energy}} \\ = \frac{\text{mechanical energy converted to electrical energy}}{\text{input mechanical energy}}. \quad \dots (1.9)$$

Jaffe et al [9] defined the piezoelectric constants as partial derivatives evaluated at constant stress (subscript T), constant field (subscript E), constant displacement (subscript D) or constant strain (subscript S). These may be thought of as 'free', 'shortcircuit', 'opencircuit' and 'clamped' respectively. The actual definitions are



$$d = \left( \frac{\partial S}{\partial E} \right)_T = \left( \frac{\partial D}{\partial T} \right)_E \quad \dots (1.10a)$$

$$g = \left( -\frac{\partial E}{\partial T} \right)_D = \left( \frac{\partial S}{\partial D} \right)_T \quad \dots (1.10b)$$

$$e = \left( -\frac{\partial T}{\partial E} \right)_S = \left( \frac{\partial D}{\partial S} \right)_E \quad \dots (1.10c)$$

$$h = \left( -\frac{\partial T}{\partial D} \right)_S = -\left( \frac{\partial E}{\partial S} \right)_D \quad \dots (1.10d)$$

The effect of symmetry on the piezoelectric matrices relating strain and electric field were worked out by Voigt and fully discussed by Cady [1]. The initially isotropic piezoelectric ceramic on poling has its isotropy destroyed in the direction of the poling field. However the isotropy is maintained in the plane normal to the poling field direction. The symmetry of the poled ceramic is therefore considered as  $\infty mm$  (cylindrical polar symmetry).

The equations of state relating the electric and elastic variables can be written in a general form as follows

$$D = dT + \epsilon^T E \quad (\text{Direct piezoelectric effect}) \dots (1.11a)$$

$$S = S^E T + dE \quad (\text{Converse piezoelectric effect}) \dots (1.11b)$$

The elastic, dielectric and piezoelectric properties are orientation dependent in all piezoelectric media. For the symmetry of ceramics ( $\infty mm$ ), the general equation is replaced by a specific set of equations.

$$D_1 = E_1 E_1 + d_{15} T_5 \quad \dots (1.12a)$$

$$D_2 = E_1 E_2 + d_{15} T_4 \quad \text{Direct effect} \dots (1.12b)$$

$$D_3 = E_3 E_3 + d_{31} (T_1 + T_2) + d_{33} T_3 \quad \dots (1.12c)$$

$$S_1 = S_{11}^E T_1 + S_{12}^E T_2 + S_{13}^E T_3 + d_{31} E_3 \quad \dots (1.13a)$$

$$S_2 = S_{11}^E T_2 + S_{12}^E T_1 + S_{13}^E T_3 + d_{31} E_3 \quad \dots (1.13b)$$

$$S_3 = S_{13}^E (T_1 + T_2) + S_{33}^E T_3 + d_{33} E_3 \quad \text{Converse effect} \dots (1.13c)$$

$$S_4 = S_{44}^E T_4 + d_{15} E_2 \quad \dots (1.13d)$$

$$S_5 = S_{44}^E T_5 + d_{15} E_1 \quad \dots (1.13e)$$

$$S_6 = S_{66} T_6 \quad \dots (1.13f)$$

The subscript 3 refers to the poling axis and 1 and 2 refer to arbitrarily chosen orthogonal axes in the plane normal to 3. Subscripts 4, 5 and 6 refer to the shear stress and strain in planes normal to the 1, 2 and 3 axes, respectively. Also by conventional notation, the first subscript of the 'd' constant gives the electrical direction (field or electric displacement) while the second gives the component of mechanical deformation.

Both static and dynamic methods of measurement are used to evaluate the various piezoelectric constants. A scheme for such measurements can be obtained from Appendix 1.

The details are provided in [5] and [10] . Only the resonance method has been included here to emphasise its superiority over other methods of measurement.

Simple measurements of resonant and antiresonant frequencies are used to evaluate piezoelectric effects. Elastic bodies show numerous resonances, the most pronounced are those where the body can just accomodate one half wavelength of a standing elastic wave. The piezoelectric effect is a convenient way to excite such elastic waves, to permit observation of the interaction of the mechanical resonance with the electric behaviour. This is best seen in the equivalent circuit idealised for a single resonance (Fig.1.4). The values of  $L$  and  $C_1$  are such that at the resonant frequency ' $f_r$ ' the impedances  $2\pi f_r L$  and  $-1/2\pi f_r C_1$  are opposite in sign and equal in magnitude, and the total impedance of this branch is given only by the mechanical resistance ' $R$ ', which is comparatively quite small. This mechanical branch is however in parallel with the electric capacitance ' $C_0$ '. The frequency of minimum impedance or 'resonance', ' $f_r$ ' is that of a standing wave under 'zero field' conditions. For applied frequencies above ' $f_r$ ' the mechanical branch becomes inductive. When the series impedance of this branch becomes opposite and equal to the impedance of ' $C_0$ ', the impedance of the crystal reaches a maximum since opposite currents flow in the two branches. This condition of parallel resonance, however, means constant charge on the crystal. The frequency of maximum impedance or 'antiresonance' ' $f_a$ ', is therefore

that of a standing wave under open-circuit conditions.

## 1.6 The Lead-Zirconate-Titanate System:

Ceramics of piezoelectric  $\text{Pb}(\text{Ti},\text{Zr})\text{O}_3$  solid solutions, have achieved wide usage in recent years because of their superior properties. The ferroelectric nature of these materials was established in Japan early in the 1950's. Since then intensive work on this system has been carried out throughout the world.

A current version of the  $\text{Pb}(\text{Ti},\text{Zr})\text{O}_3$  phase diagram is shown in Fig 1.5. Substitution of  $\text{Zr}^{+4}$  for  $\text{Ti}^{+4}$  in  $\text{PbTiO}_3$  reduces, the tetragonal distortion (Fig.1.6) and ultimately causes the appearance of another ferroelectric phase of rhombohedral  $R3m$  symmetry. The boundary between the tetragonal and rhombohedral forms is nearly independent of temperature (morphotropic). Still more  $\text{Zr}^{+4}$  cause the appearance of the orthorhombic antiferroelectric  $\text{PbZrO}_3$  phase with a small field of stability of a tetragonal antiferroelectric phase near the Curie point. Its exact extent is rather impurity sensitive.

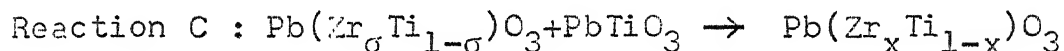
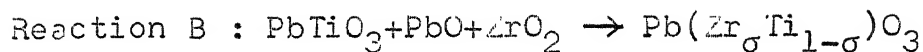
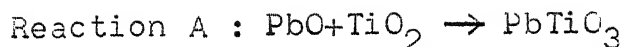
The rhombohedral ferroelectric phase actually divides into two phases . Although both appear to be simple cell rhombohedral by X-ray diffraction, neutron diffraction studies indicate a multiple rhombohedral cell for the low temperature phase.

Though early literature on the subject indicated the tetragonal - rhombohedral phase boundary as narrow and vertically straight<sup>with</sup> a particular Zr/Ti ratio, later research has revealed that it is not so. Mabud [11] from X-ray diffraction photographs established that the MPB is not a narrow and vertically straight boundary but a region whose width depends on the firing time and temperature. He also suggested that where two phases coexist, there were islands of rhombohedral regions scattered in the tetragonal matrix and tetragonal regions scattered in the rhombohedral matrix though he could not infer from his study whether they were of the same composition or not. Hanh et al [12], a year earlier had also postulated that the MPB is a two phase region of measurable width. Their conclusions were based on the splitting of the (200) reflections into three lines, two due to the tetragonal structure and the other due to the rhombohedral one. In their X-ray analysis they used a X-ray diffractometer and  $\text{CuK}\alpha$  radiation. They were able to relate their postulate with results obtained from dielectric measurements. It was also established that the coexistence of the tetragonal and rhombohedral phases occur due to composition fluctuation in the  $\text{Pb}(\text{Ti}, \text{Zr})\text{O}_3$  solid solution [13]. Kala [14] theorised that the relaxation of internal stresses which arise due to contraction or

dilation of lattice parameters in  $\text{Pb}(\text{Ti},\text{Zr})\text{O}_3$  solid solution during temperature changes or application of an external electric or mechanical fields is a primary reason for the coexistence of phases. Ari-Gur et al [15], by means of X-ray diffraction determined directly the coexistence region near the MP change of PZT. Like [12] they also considered the splitting of the (200) reflection. They also found that the morphotropic phase change is a first order transition, a function of temperature and chemical potential and not the concentration as was often supposed previously.

The sustained interest in the coexistence region of PZT ceramics is because of the excellent electromechanical properties of these materials near the MPB. The dielectric, elastic and piezoelectric properties of some PZT compositions near the MPB has been included in Appendix 2 (10) .

The solid state reactions occurring prior to and during the formation of  $\text{Pb}(\text{Ti},\text{Zr})\text{O}_3$  solid solution was also investigated by a host of researchers. Matsuo et al [16] stated that the reaction begins by formation of a highly tetragonal lead titanate solid solution into which the remaining  $\text{PbO}$  and  $\text{ZrO}_2$  react to form  $\text{Pb}(\text{Ti},\text{Zr})\text{O}_3$ .



They provided a diagram (Fig. 1.7) relating the mole fraction of each phase in the system  $\text{PbO}:\text{TiO}_2\text{-PbO}:\text{ZrO}_2$  as a function of the firing temperature. Significant deficiency of PbO due to PbO volatilisation cause the presence of free  $\text{ZrO}_2$ , as well as the  $\text{Pb}(\text{Ti},\text{Zr})\text{O}_3$  solid solution as is seen from the scheme of reaction. Incomplete reaction also results in the presence of a free  $\text{ZrO}_2$  or PbO second phase.

Like Matsuo et al [16], Gesemann et al [17] and Harris [17] also did not observe formation of  $\text{PbZrO}_3$  as an intermediate phase. But Ohno et al [18] reported that PZT solid solution is synthesised after formation of both PT and PZ. Mori et al [17] reported formation of PZ as an intermediate phase only when the  $\text{ZrO}_2$  content of the mixture was greater than 60 mole %. Similarly Yamaguchi et al [19] found that a ball-milled oxide mixture shows no presence of PZ as an intermediate phase, whereas precipitation mixing results in PZ formation. Thus it is sufficiently clear that the formation of the PZ phase is dependent on the particular raw materials <sup>being</sup> used, being governed chiefly by the particle size and the reactivity of the raw material. Venkatramani et al [20]'s work substantiates this observation. They

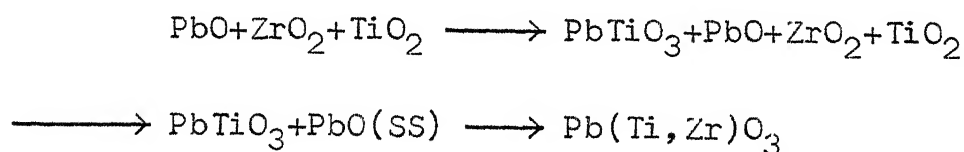
reported that if ultrafine, high purity chemically prepared  $\text{ZrO}_2$  is used in place of commercial  $\text{ZrO}_2$ , PZ phase will be present along with  $\text{PbTiO}_3$ . The altered sequence of reaction is attributed to the enhanced reactivity of  $\text{ZrO}_2$  due to its ultrafiness and hence large surface area.

Chandratreya et al [17] also ascertained the reaction sequence for the formation of PZT solid solution. Reagent grade massicot  $\text{PbO}$ ,  $\text{TiO}_2$  (99.9% pure) and reactor grade unstabilised  $\text{ZrO}_2$  was used in the investigation. Samples of ternary mixtures with  $\text{ZrO}_2/\text{TiO}_2 = 65/35$  were subjected to XRD analysis after quenching from several temperatures. Specimens quenched from  $580^\circ$  and  $665^\circ\text{C}$  showed peaks for  $\text{PbTiO}_3$  but no detectable peaks for  $\text{PbZrO}_3$  or  $\text{Pb}(\text{Ti},\text{Zr})\text{O}_3$ . PZT solid solution formation initiated at about  $715^\circ\text{C}$  but by  $785^\circ\text{C}$  it was virtually complete. No peaks attributable to  $\text{PbZrO}_3$  alone were observed, indicating that no significant amount of  $\text{PbZrO}_3$  was formed. Yet the formation of small amounts of  $\text{PbZrO}_3$  was not ruled out, due to the difficulty in interpretation of X-ray patterns. Above the Curie temperatures,  $\text{PbTiO}_3$  and  $\text{PbZrO}_3$  form a continuous solid solution of cubic structure. When cooled to room temperature, the solid solution can exist in one of three structures: tetragonal, rhombohedral or orthorhombic, depending on the  $\text{Zr}/\text{Ti}$  ratio. As a result



XRD patterns are complex, involving overlaps and shifts of peaks due to solid solution formation. The conclusion of this investigation was  $\text{PbTiO}_3$  forms first and on increasing temperature  $\text{ZrO}_2$  takes part in the reaction. The three reactants  $\text{PbO}$ ,  $\text{ZrO}_2$  and  $\text{PbTiO}_3$  then form a reactive system in which perovskite formation occurs at two interfaces  $\text{ZrO}_2/\text{PbO}$  and  $\text{ZrO}_2/\text{PbTiO}_3$ . A coupled reactive exchange of  $\text{Zr}^{+4}$  and  $2\text{Pb}^{+2}$  at  $\text{ZrO}_2/\text{PbTiO}_3$  and  $\text{Ti}^{+4}$  and  $2\text{Pb}$  at the  $\text{PbTiO}_3/\text{PbO}$  interfaces followed by a counter diffusion of  $\text{Zr}^{+4}$  and  $\text{Ti}^{+4}$  within the perovskite lattice set up the formation of the stoichiometric PZT solid solution.

Based on their calcination reaction studies of the  $\text{PbO-ZrO}_2\text{-TiO}_2$  ternary system Hankey et al [21] provide the following reaction scheme.



The phase  $\text{PbO(SS)}$  is defined as a tetragonal solid solution of  $\text{PbO}$ ,  $\text{PbTiO}_3$  and  $\text{ZrO}_2$ . This work substantiates the basic reactions as described by Speri[22]. The calcination reaction diagram for  $\text{Pb(Zr}_{0.5}\text{Ti}_{0.5})\text{O}_3$  regions as functions of calcination conditions are shown in Fig. 1.8 [20].

## 1.7

The mechanical strength and hardness of piezoelectric ceramics is a factor that must be considered in the design of transducers and other piezoelectric devices. Many applications involve electrically or thermally induced stresses as well as possible mechanical loads due to vibration. Materials like lead zirconate titanate and barium titanate fail in a brittle manner from pre-existing flaws, typical pores and pore clusters, machining-induced cracks, and inclusions. The presence of these small (typically 20-100 $\mu$ m) defects in ceramics leads to the magnification of applied stresses at these sites.

The present understanding of the strength and hardness processes in piezoelectric ceramics is therefore dependent largely on developments in fractography. In the case of small cracks at the surface of these materials or in conjunction with pores, the science of linear elastic fracture mechanics is used to model fracture. Linear elastic fracture mechanics define a term known as the stress intensity factor,  $K_I$ . It is a measure of the stresses near the cracks and is the driving force for crack extension. In the absence of environmental effects, increasing the stress on the body to a critical value 'S' will cause the flaw to grow rapidly to failure.

$$K_{IC} = YSC^{1/2} \quad \dots \quad (1.14)$$

Where Y is a constant determined by flaw location and C is the depth of the crack.

$K_{IC}$  is a material property that depends on the chemistry, crystal structure and microstructure of the ceramic.

Fracture toughness is generally determined by putting a crack or flaw of known size into the material and applying a load until the crack grows to failure. Among numerous techniques used to determine  $K_{IC}$  the double-cantilever and the indentation techniques are more important.

#### Double-Cantilever Beam Technique (23):

A crack is initiated at the centre of the specimen, and the specimen is loaded in air in a test machine by the application of bending moments to arms bonded to the top of the specimen. The stress intensity factor is calculated from the applied load and the geometry of the specimen. ' $K_{IC}$ ' is taken as the point where there is a precipitous drop in load.

#### Indentation Technique:

Indentation techniques are discussed in [24,25, 26]. Two different procedures are used. In the first a flaw is

introduced into the polished surface of a material using a conventional Vickers tester[27]. The cracks emanating from the hardness impression are measured. ' $K_{IC}$ ' is calculated from the crack length and the indentation load [24]. In the second method, a Vickers indenter is used to place a flaw in the surface of a bar or plate of material. This specimen is subsequently broken in flexure. ' $K_{IC}$ ' is got from fracture strength  $\sigma$ , the indentation load  $P$ , the hardness  $H$  and elastic modulus  $E$  of the material [25].

$$K_{IC} = 0.59 \frac{E}{H}^{1/8} (\sigma P^{1/3})^{3/4} \dots (1.15)$$

Typical values of  $K_{IC}$  for barium titanate and lead zirconate titanate are summarised in [29]. The differences in  $K_{IC}$  between the various materials is due to intrinsic chemical bond differences as well as to differences in microstructure.

Microstructure has an effect on the fracture energy ( $\gamma$ ) of ferroelectrics like  $BaTiO_3$ . The maximum  $\gamma$  takes place at the grain size at which the contribution to toughening due to twinning and microcracking is balanced by the linking of microcracks. The process follows a model developed by Rice et al [29] for the fracture energy of noncubic ceramics. The microstructural aspect of crack propagation in ceramics is discussed elaborately in (30,31,32,33). When measured in the cubic symmetry state the fracture energy is independent of grain size. The fracture toughness of materials such as PZT is dependent on whether testing is performed in the paraelectric (cubic) state or the ferroelectric state. In the

ferroelectric state, twin crack and / or crack microcrack interactions give rise to an increase in  $K_{IC}$  above that in the cubic material.

In PZT,  $K_{IC}$  is also dependent on the Zr/Ti ratio. The minimum in  $K_{IC}$  occur at phase transitions where the contribution of microcracking to toughness is reduced.

Cooling from the paraelectric to the ferroelectric phase introduces internal stress in the ceramics. Internal stresses are also induced by the application of dc field or aging changes, Okazaki [34] has indicated a procedure for calculating such stresses. These stresses when present increase the strength of  $BaTiO_3$  like ceramics [35].

The subject of subcritical crack propagation and time dependent deformation in unpoled PZT was investigated by Koepke et al [36]. Their study was based on double torsion and stress relaxation techniques. Slow crack growth in PZT is sensitive to both chemical and electrical testing environments. Moisture and high ac or dc fields applied perpendicular to the crack plane enhance crack propagation in unpoled PZT. The stress relaxation data can be treated in terms of an analysis of thermally activated deformation.

Even though ceramics are brittle materials, prior to fracture, <sup>they</sup> undergo a certain amount of plastic deformation. The Vickers hardness ( $H_V$ ) gives a measure of the plastic deformation or slip undergone by these ceramics [37]. Plastic deformation involves pulverisation and slip and rotation of the fragments as they continue to adhere to each other. Plastic deformation which is caused by dielectric

is dependent primarily on the microstructure which is usually controlled during processing. Porosity, grain size and the amount and distribution of phases affect Vickers hardness values. These variables depend largely on the calcination and sintering conditions during fabrication. Mobnar et al [38] have also shown that strength anisotropy exists in cold pressed and sintered rings related to pore anisotropy.

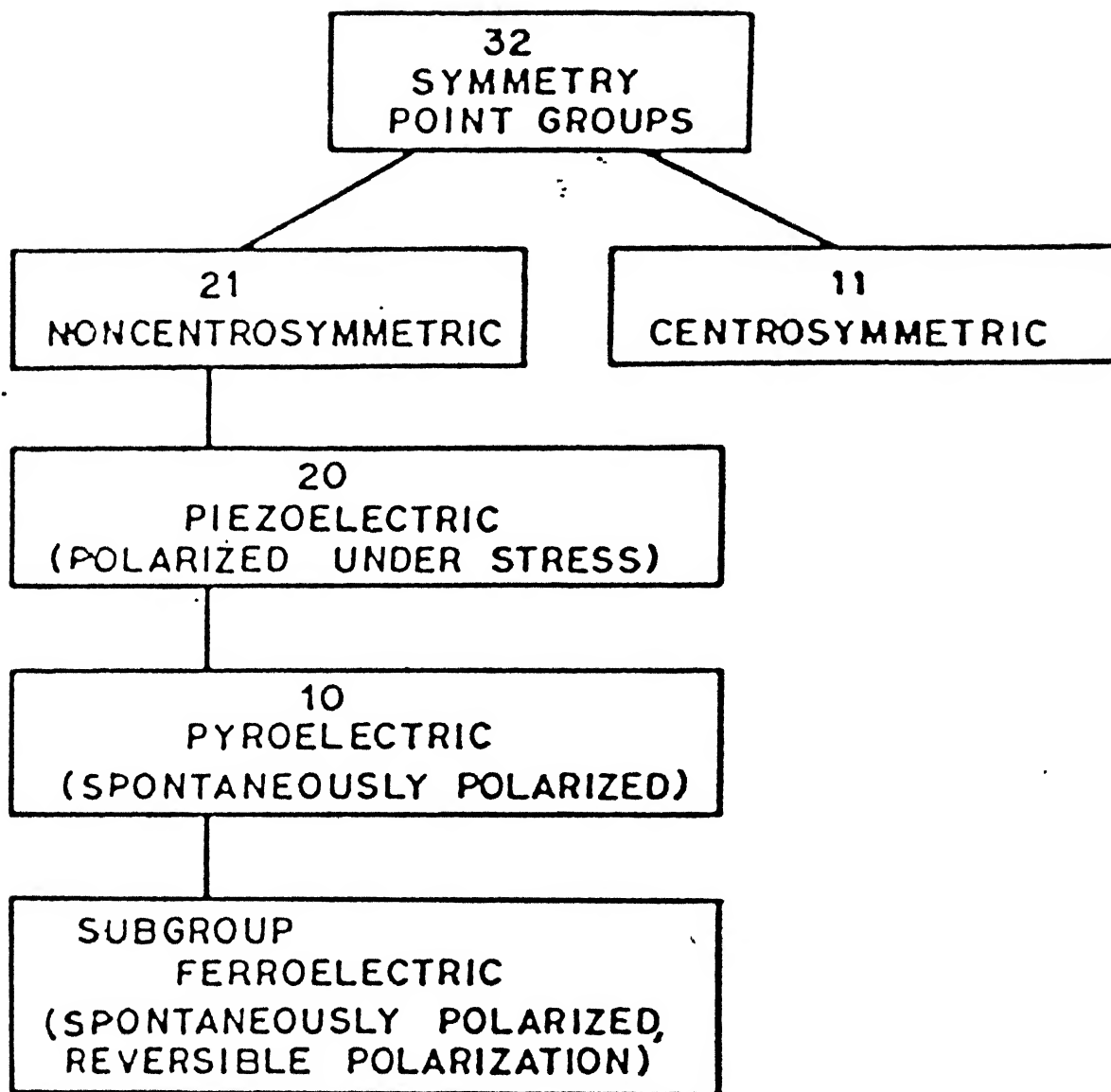


Fig. 1. 1 Interrelationships of piezoelectrics and subgroups on the basis of internal crystal symmetry.

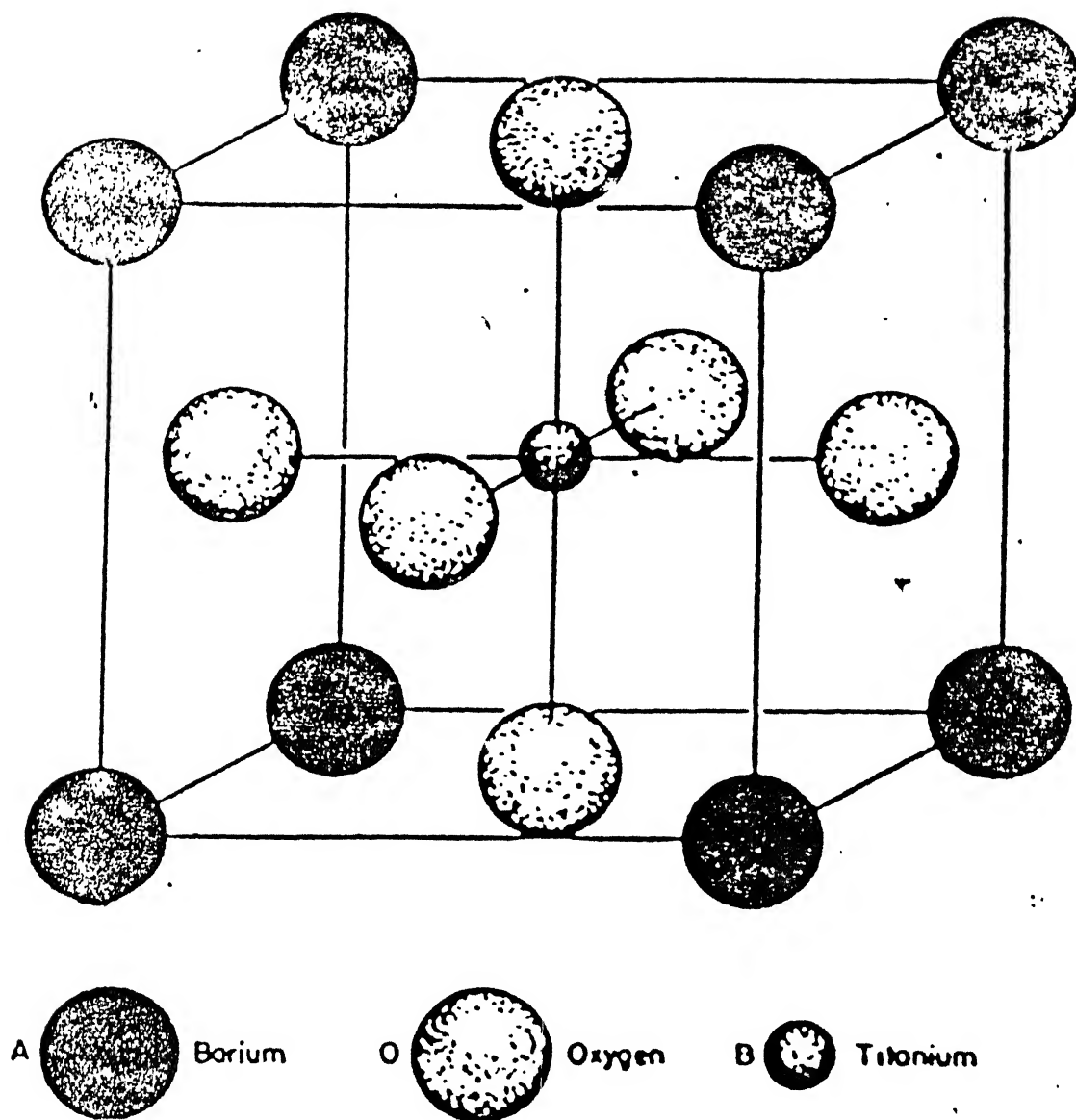


Fig. 1.2 The perovskite structure as typified by  $\text{BaTiO}_3$  above its Curie point.



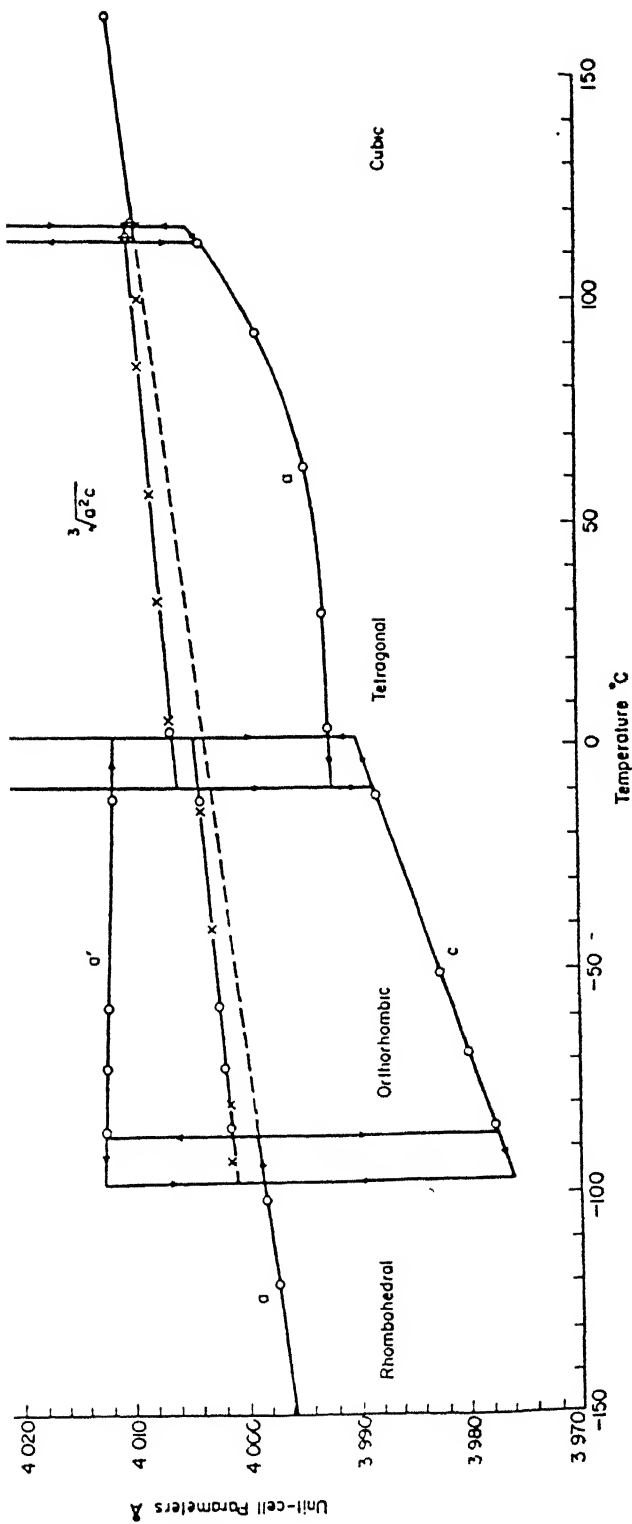
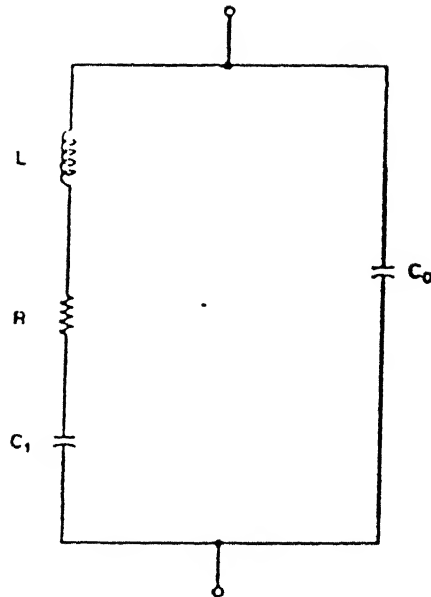
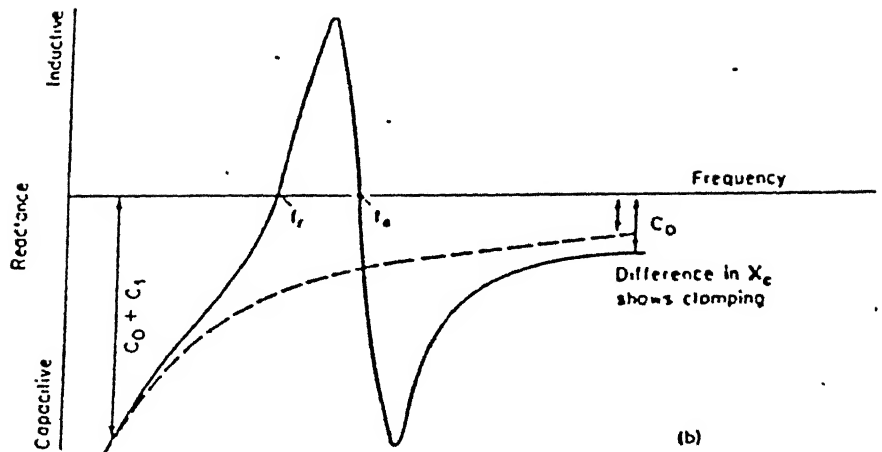


Fig. 1.3 Lattice parameters of BaTiO<sub>3</sub> as function of temperature.



(a)



(b)

Fig. 1.4(a) The equivalent circuit of a piezoelectric body near a fundamental resonance. The elements  $L, C_1, R$  are mass, elastic compliance and mechanical damping transformed into electrical magnitude by the piezoelectric effect.  $C_0$  is the capacitance in the absence of mechanical deformation at the frequency of the resonance under consideration.

(b) Reactance of a piezoelectric resonator compared with a capacitor of equal at low frequency. (dotted curve).

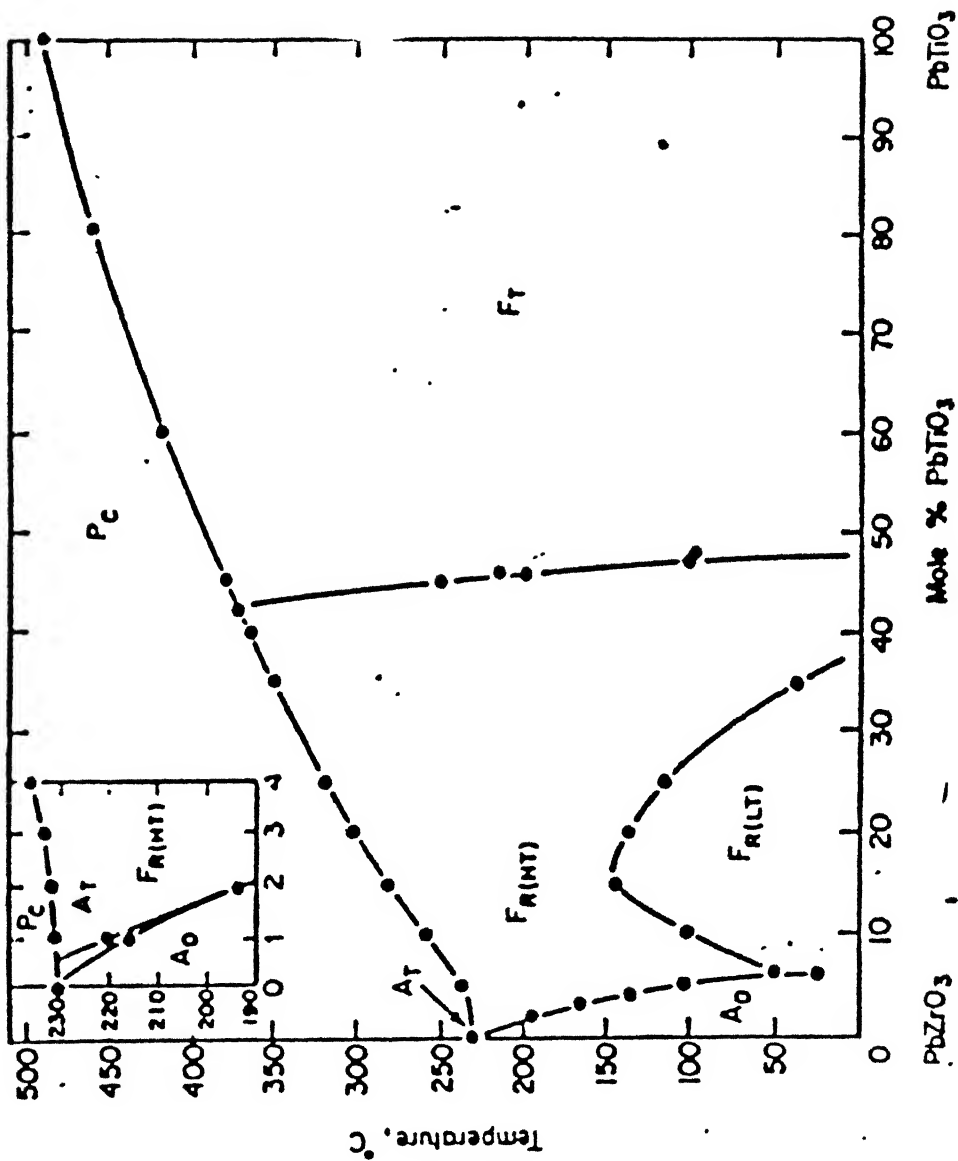


Fig. 1.5  $\text{PbTiO}_3$ - $\text{PbZrO}_3$  sub-solidus phase diagram.

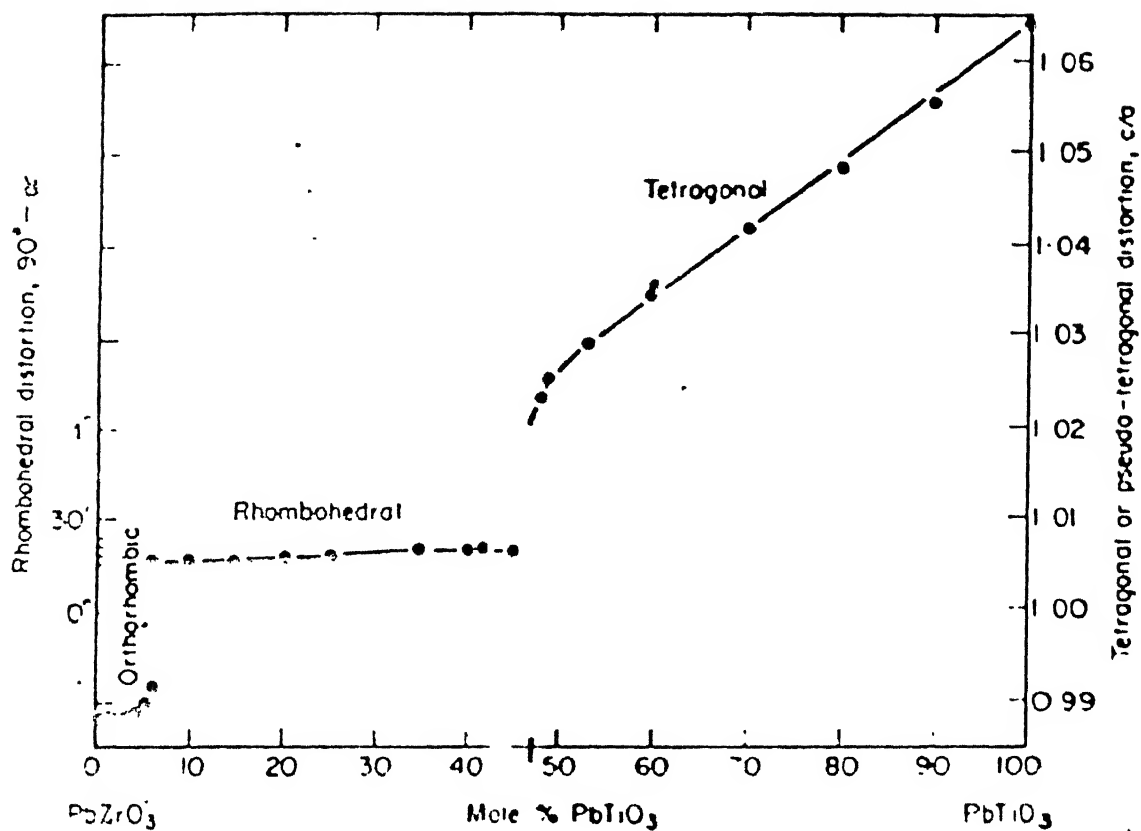


Fig. 1.6 Unit cell distortion at room temperature for the  $\text{PbTiO}_3$ - $\text{PbZrO}_3$  system.

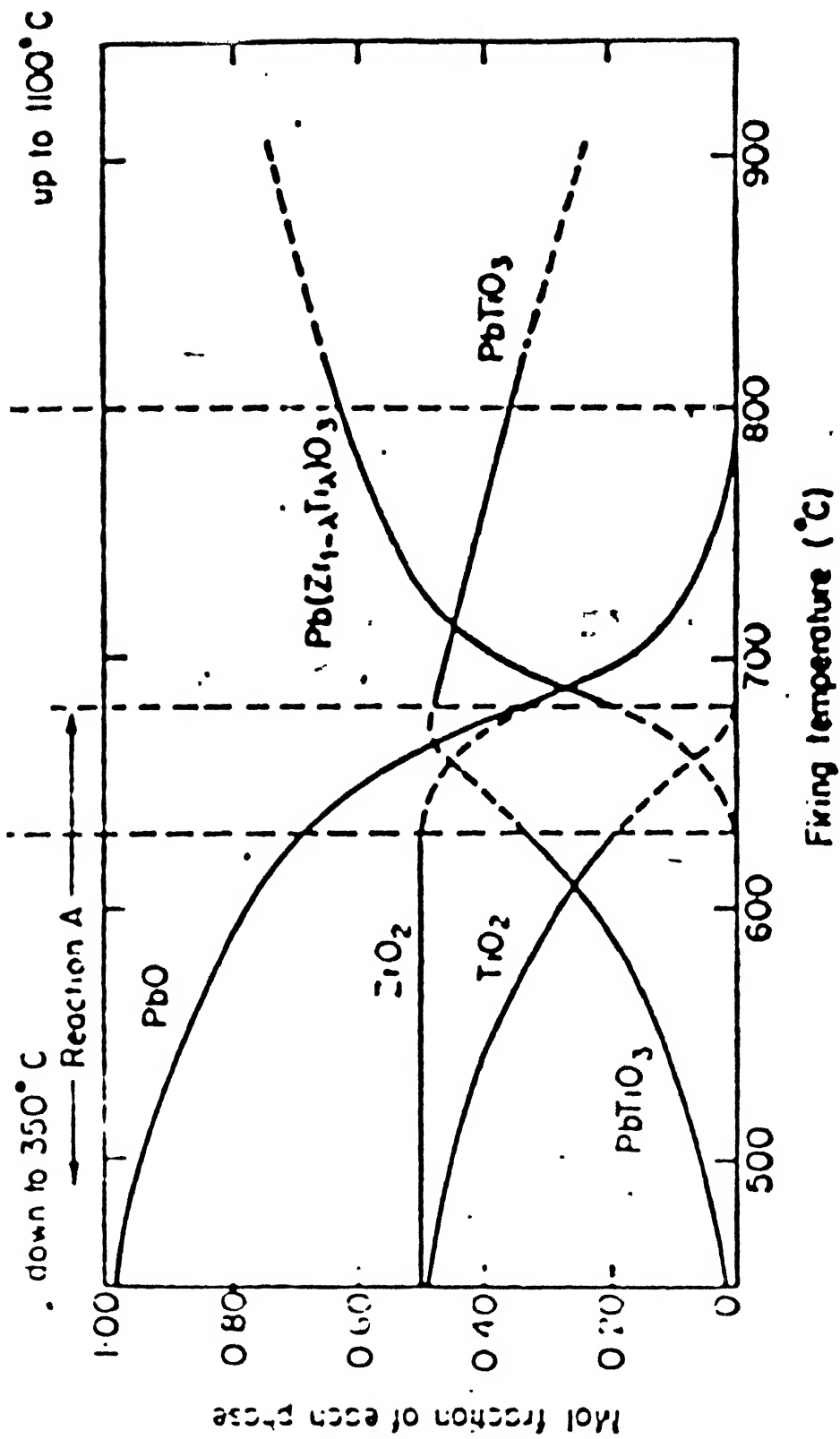
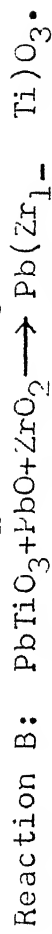
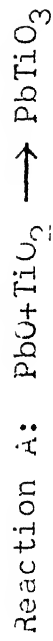


Fig. 1.7

Phases in the system  $\text{PbO}-\text{TiO}_2-\text{PbO}:\text{ZrC}_2$  as a function of firing temperature.



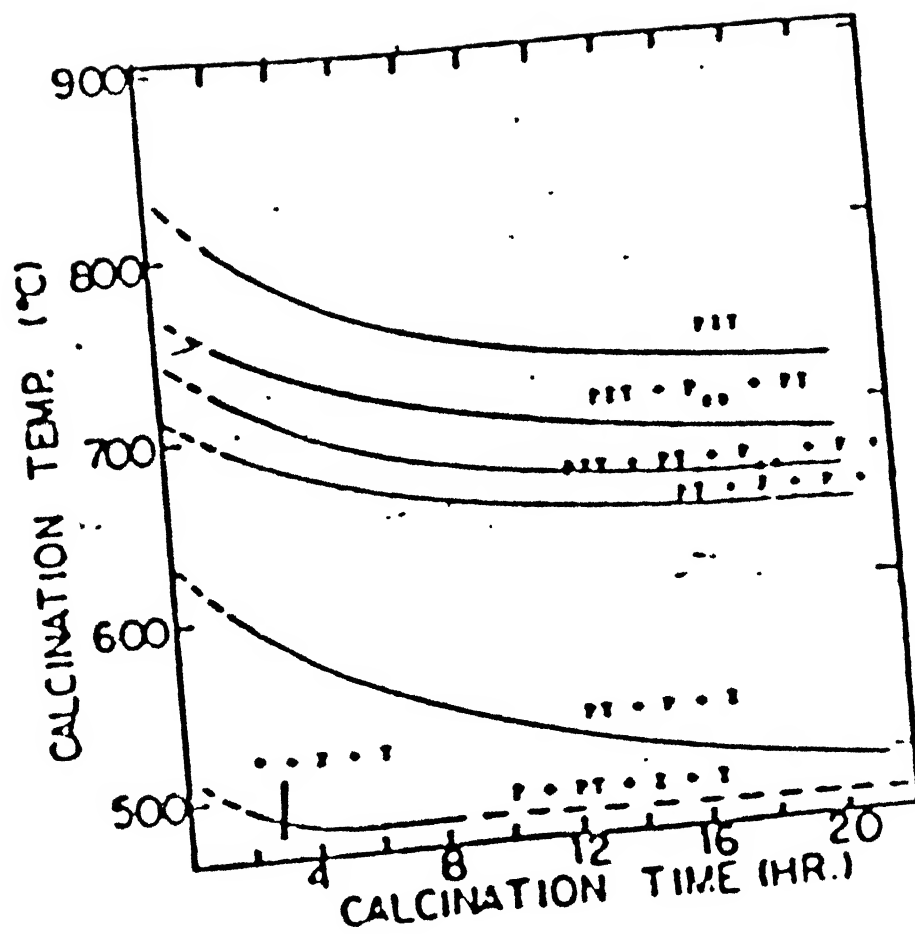


Fig. 1.8 Calcination reaction diagram for  $\text{PbZr}_{0.50}\text{Ti}_{0.50}\text{C}$

## CHAPTER 2

### EFFECT OF PROCESSING PARAMETERS ON THE MICROSTRUCTURE AND COMPOSITION FLUCTUATIONS OF $\text{Pb}(\text{Ti},\text{Zr})\text{O}_3$ COMPOSITIONS

Like any other electronic ceramic material lead-zirconate-titanate is also highly composition and microstructure sensitive in terms of its mechanical, elastic, dielectric and piezoelectric properties. The control of composition fluctuation and microstructure is achieved through selection of better grade starting materials and/or through processing. A detailed survey about how the processing parameters influence the microstructure and inhomogeneity is therefore of much importance.

A flowsheet of the fabrication of  $\text{Pb}(\text{Ti},\text{Zr})\text{O}_3$  compositions by the mixed oxide process is shown in Fig. 2.1 [30]. Chemical processes which are used to manufacture  $\text{Pb}(\text{Ti},\text{Zr})\text{O}_3$  for high quality performance are similar after the drying stage, the difference being initially in the production and mixing methods of the constituents. A variety of chemical methods have been investigated. The coprecipitation method provides a powder of very fine particle size and high reactivity. PZT compacts made with such powders have high sinterability and a very uniform microstructure with practically negligible porosity. However the method is not recommended for fabrication of doped  $\text{Pb}(\text{Ti},\text{Zr})\text{O}_3$  compositions

because of the difficulty of simultaneous precipitation of various cations. McNamara [40] demonstrated a way to obtain a precipitate of  $\text{Pb}^{+2}$ ,  $\text{Zr}^{+4}$  and  $\text{Ti}^{+4}$  using  $\text{NH}_3$  and  $\text{CO}_2$  gases bubbling into the reactor.

A thermal spray decomposition method [41] and a freeze-drying method [42] were also tried in obtaining a solid phase from a solution. Though the difficulty did not increase with the number of kind of cations, no data regarding the composition fluctuation of compacts made by this process are available.

Noticing that the composition fluctuation arose at the site of  $\text{Zr}^{+4}$  and  $\text{Ti}^{+4}$  in the PZT system [43] and that the stoichiometry could be easily attained between an A-site ion and a B-site ion in the perovskite type compound of  $\text{ABO}_3$ , Kakegawa et al obtained  $\text{Pb}(\text{Ti}, \text{Zr})\text{O}_3$  having no composition fluctuation by solid-solid reaction of oxides containing  $\text{Zr}^{+4}$  and  $\text{Ti}^{+4}$  prepared by the wet method with  $\text{PbO}$  powder [13]. A mixed oxide of titanium and zirconium formed by spray decomposition, mixed with equimolar  $\text{PbO}$  and heated to elevated temperatures was also tried [44]. Fluctuations in this case were about 3 at%.

Though some reference was made to PZT prepared by wet methods above, it may be useful to revert to the discussion on the processing parameters of the MO process



as it is currently still the most popular among the fabrication methods and is being employed by the author in his investigations. The quality of the starting constituents determine the microstructure and inhomogeneity of  $\text{Pb}(\text{Ti},\text{Zr})\text{O}_3$  compositions significantly. Use of a high purity, highly reactive, chemically prepared submicron sized  $\text{ZrO}_2$  leads to a calcination reaction sequence different from that when commercial  $\text{ZrO}_2$  is used. If the  $\text{ZrO}_2$  is not very reactive the diffusion of  $\text{Zr}^{+4}$  ions in the  $\text{PbTiO}_3$  structure get hindered leading to the formation of second phase free  $\text{ZrO}_2$  and a high composition fluctuation in the PZT. The crystal structure of  $\text{TiO}_2$  however has no significant effect on the mentioned variables.

The mixing process is normally achieved in ball, vibratory, drum or blunging mills with zirconia or alumina balls [12,14,45,46,47,48,49] or cylinders. Distilled or deionised water or organics like isopropanol, ethanol or acetone/stearic acid mixtures are used to make up the slurry. A higher milling time promotes a lower composition fluctuation and a more uniform microstructure in the ceramic. Use of organic media during the wet homogeniation process provides the advantage of cutting down on drying time thereafter and hence reducing  $\text{PbO}$  segregation. Where distilled or deionised water is used, normally another dry mixing step follows drying.

The importance of the calcination reaction is emphasised in [47]. Buckner et al demonstrated that the sintered density of  $\text{Pb}(\text{Ti},\text{Zr})\text{O}_3$  compositions is controlled largely by the calcination temperature. If the calcination temperature is high enough the calcination time is of relative unimportance. As the PZT formation process ends during calcination it is easy to understand that a higher calcination temperature and time leads to more homogenisation.

Hankey et al [50] showed that the rate constant at packing pressures  $> 100$  MPa for solid-state reactions during  $\text{PbTiO}_3$  formation in the  $\text{PbO}-\text{ZrO}_2-\text{TiO}_2$  system increased by a factor of three on increasing packing pressure. They determined that the formation of  $\text{PbTiO}_3$  followed the Jander model for diffusion controlled reactions with unidirectional bulk diffusion of  $\text{Pb}^{+2}$  and  $\text{O}^{-2}$  ions. The packing geometry which is dependent on the packing pressure can therefore be utilised to alter calcination kinetics and subsequent sintering mechanisms to obtain better microstructures in fired  $\text{Pb}(\text{Ti},\text{Zr})\text{O}_3$ .

The binder addition and removal steps are important for the microstructure of the fired PZT. An excess quantity of binder or a non uniform distribution of it result in large pores. The effects of nonuniform distribution of binder is seen in Figs 2.2 and 2.3 [28]. Lamination effects during cold pressing also contribute to pore anisotropy [38].

The sintering process has been the most explored among all the stages of PZT fabrication. Various investigators have researched on the effect of sintering temperature and time, packing atmosphere and the amount of PbO excess on the density, microstructure and inhomogeneity of  $\text{Pb}(\text{Ti}, \text{Zr})\text{O}_3$  piezoelectrics and have found interesting results.

The work of Lucuta et al [46] shows the variation of density and porosity with sintering temperature (Fig. 2.4) for both modified and unmodified lead-zirconate-titanate compositions. Increase in the sintering temperature led to a decrease in porosity due to a decrease in the number and size of the pores but after the porosity reached a minimum the increase was attributed to enlargement of the pore diameters. In the investigation  $\text{PbZrO}_3$  pellets with 3% excess PbO was used. in the packing arrangement. At that temperature at which the PbO vapour pressure equaled the equilibrium values for the following,- evaporation-recondensation equilibrium,



the porosity was the minimum. Processing variables like to rate of heating, time of thermal treatment, atmosphere and additives influenced the equilibrium. The increase of porosity at temperatures higher than the optimum was caused by a greater rate of evaporation of PbO than its recondensation. The grain size increased exponentially with increasing sintering temperature for both doped and undoped samples.

The width of the coexistence phase region decreases with sintering temperature [45,46] and sintering time [13]. Vasilau et al explained it on the basis of microregion composition fluctuations, resulting from the particular sintering technology used in preparing the samples; which cannot provide a truly atomic homogeneity in the solid solution. Very small regions rich in either lead titanate (tetragonal phase) or lead zirconate (rhombohedral phase) are formed as a function of microscopic concentration and temperature gradients. With increasing sintering temperature diffusion effects within these regions are enhanced leading to a higher and lower Zr/Ti ratio, in each microregion respectively, compared with the ratio at lower temperatures. The tetragonality of the unit cell in the tetragonal microzone therefore decreases as was observed experimentally, similar to that found by varying the macroscopic Zr/Ti ratio [51]. On the other hand the lowering of the local Zr/Ti ratio has a negligible influence on the rhombohedral unit cell. Also no effect is found by varying the composition in the LPB coexistence region [12,15].

The role of packing powder in determining the stoichiometry and microstructure of  $\text{Pb}(\text{Ti},\text{Zr})\text{O}_3$  is very significant. Chiang et al [49] found that  $\text{Pb}_{1-y}(\text{Zr}_{0.52}\text{Ti}_{0.48})\text{O}_{3-y}$  disks with 3 wt% excess  $\text{PbO}$ , sintered at  $1200^\circ\text{C}$  for 8 hours in PZ and PZ+Z packing powders had the same fired densities

although the grain size was smaller for the latter set. A specimen sintered in finer PZ+Z packing powder had a slightly higher density and an intermediate grain size. They discussed the volatility of PbO from the specimen in terms of the PbO activity ( $a_{\text{PbO}}$ ) which is the ratio of the PbO partial pressure above the PZT compound to that above pure PbO at a given temperature. Fig. 2.5 shows plots of  $a_{\text{PbO}}$  vs  $1/T$  for equilibrium combinations of some compound. In a close system the  $a_{\text{PbO}}$  tends to equilibrate between the specimen and the packing powder. If a PZ packing powder is used, its  $a_{\text{PbO}}$  will depend on the degree of its saturation with PbO. If  $a_{\text{PbO}}$  of the PZ packing powder  $> a_{\text{PbO}}$  of  $\text{Pb}_{1-y}(\text{Zr}_{0.5}\text{Ti}_{0.5})\text{O}_3$  when saturated with PbO, then some of the PbO will leave the specimen and be absorbed by the packing till it becomes saturated. On the other hand, if PZ+Z packing powder is used the system attempts to equilibrate to an  $a_{\text{PbO}}$  of  $\approx 0.08$  provided the powder has a sufficient amount of  $\text{ZrO}_2$  to absorb and react with all of the PbO volatilised from the specimens (PZT will have  $y > 0$ ). PZ+Z powder has a fixed  $a_{\text{PbO}}$  over a range of PbO contents. Thus it is useful as a packing material during sintering of PZT. The PZT can equilibrate to a fixed PbO content irrespective of its initial  $\text{PbO}/(\text{Zr},\text{Ti})\text{O}_2$  ratio [52]. Kingion et al also demonstrated that  $a_{\text{PbO}}$  for PZT compositions containing a PbO excess is a function of the PbO excess contradicting the postulates of Atkin et al [53] and Holman et al [54] who assumed that the pseudobinary system  $\text{PbZrO}_3\text{-PbTiO}_3$  behaves in the same

way as the binary systems  $\text{PbO-ZrO}_2$  and  $\text{PbO-TiO}_2$ . The need to isolate PZT compacts from PZ+Z atmosphere powder to prevent solid state diffusion of Ti ions from the former to the latter was also pointed out, contradicting the general belief that no significant transfer of  $\text{Zr}^{+4}$  or  $\text{Ti}^{+4}$  ion occurs because PbO transfer occurs in the vapour phase.

Chiang et al [49] determined the effect of PbO excess in sintered PZT compacts, and found that with an increase of excess PbO the density and grain size increased. The increase indicates the existence of a liquid-phase sintering mechanism which persists for longer times with an increase of excess PbO. The densification kinetics are discussed in [55].

Among the other factors that influence the microstructure, the geometry of the sintered compact has prime importance. Sintered rod shaped specimens have different characteristics compared to disc shaped ones [49]. The cross section of thin discs sliced from  $\text{Pb}(\text{Ti}_{0.48}, \text{Zr}_{0.52})\text{O}_3$  sintered rods which were isostatically pressed initially were not uniform. During pressing the regions adjacent to the surfaces acquired a higher unfired density which during sintering densified first providing a rigid cage and affecting the density of the inner region. The PbO content in the outer region was therefore greater than that in the inner part.

X-ray mapping and electron microprobe analysis showed that  $\text{ZrO}_2$  segregation occurred in the inner region of the compact where composition fluctuation was higher. Yet X-ray diffraction analysis showed that such compositions had only a tetragonal phase while  $\text{Pb}(\text{Ti}_{0.5}, \text{Zr}_{0.5})\text{O}_3$  compositions which were calcined in the powder form and then sintered at the same temperature had a coexistence of both phases inspite of the former being closer to the MPB. The dependence of the composition fluctuation on the  $\text{PbO-ZrO}_2\text{-TiO}_2$  mixture geometry during the calcination reaction can never be more adequately emphasised.

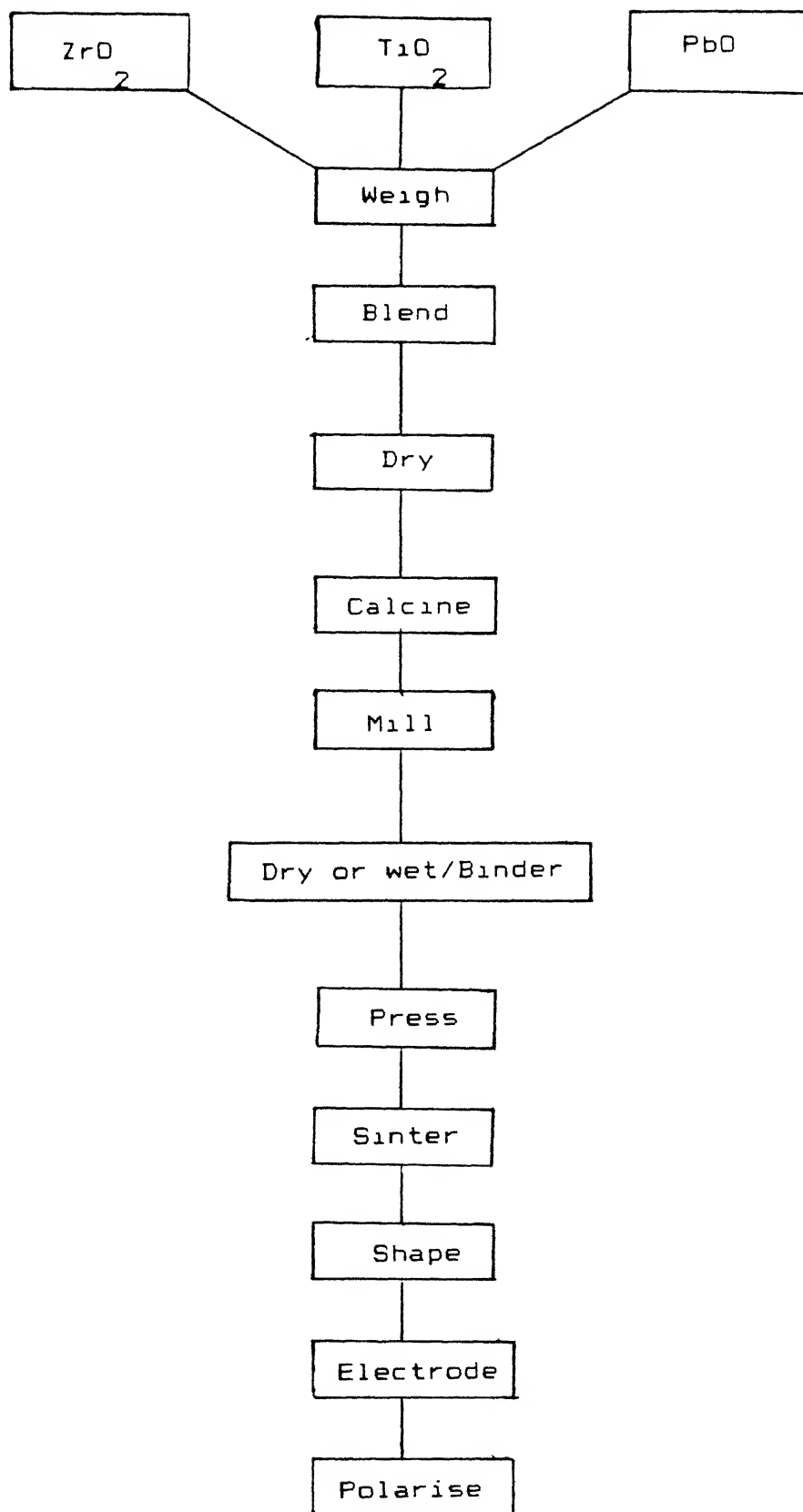


Fig. 2.1 Flowsheet of the mixed oxide (MO process) for fabrication of I.T ceramics.





Fig. 2.2 Laminar, unconnected pore in P2T microstructure. This effect is attributed to expansion of trapped gases from burn out of organic binder agglomerates.

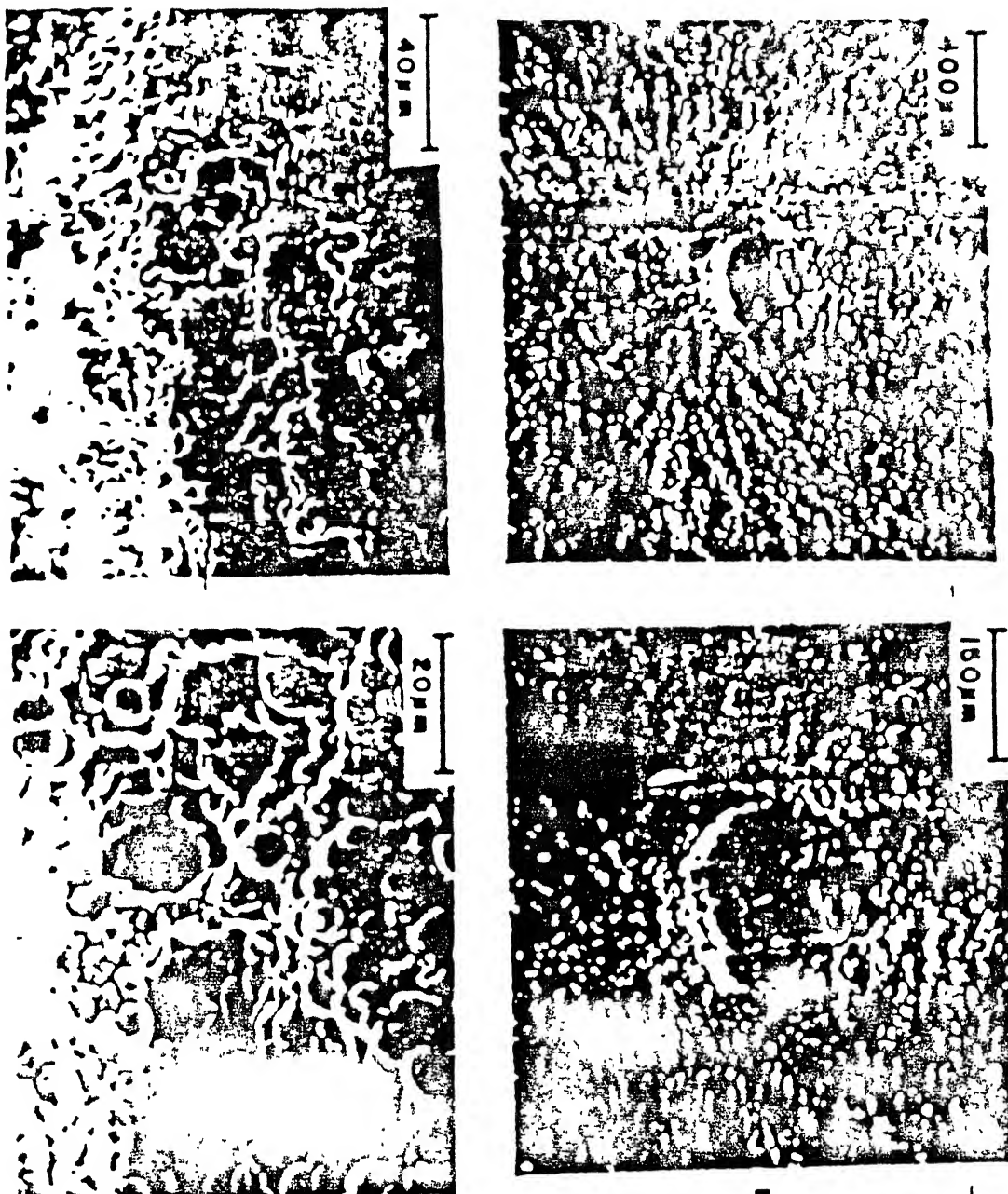


Fig. 2.3 Laminar, connected pore in PZT microstructure.

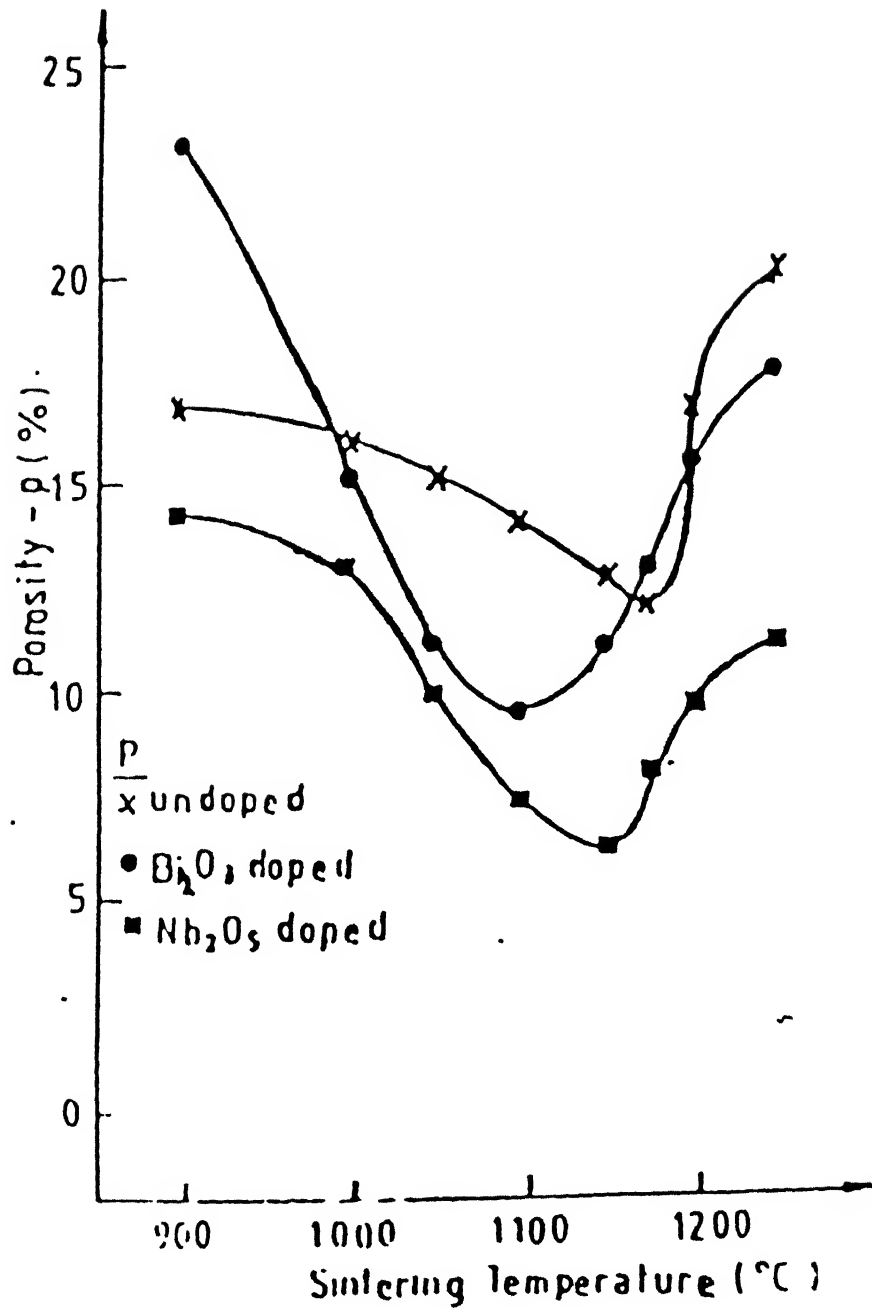


Fig. 2.4 Porosity as a function of sintering temperature for unmodified and modified  $\text{Pb}(\text{Zr}_{0.525}\text{Ti}_{0.475})$  solid solutions.

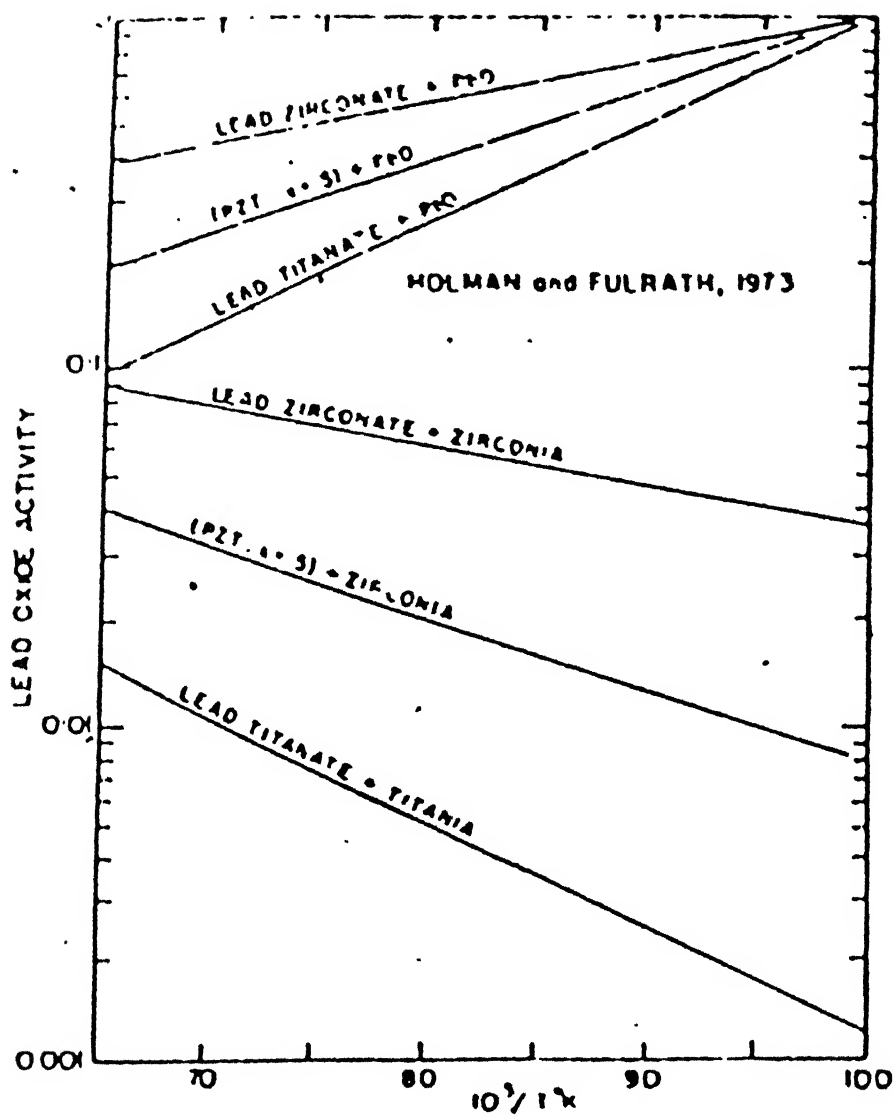


Fig. 2.5 Lead oxide activity as a function of reciprocal temperature.

DETERMINATION OF INHOMOGENEITY IN LEAD-ZIRCONATE-TITANATE  
CERAMICS BY X-RAY DIFFRACTION

## 3.1 Introduction:

The diffraction line profile analysis has long been used by metallurgists to get information about mean crystallite size and lattice strains in polycrystalline materials. Its employment in ceramic systems began rather late and still then was mostly limited to calculating crystallite size. Kakegawa et al [43] first reported that this once purely metallurgical tool could be used to calculate composition fluctuations in the lead-zirconate-titanate system. The principle of this analysis as applied to the evaluation of inhomogeneity is discussed in this chapter.

For a polycrystalline lead-zirconate - titanate specimen consisting of sufficiently large ( $>10^{-5}$  cm) and strain free crystallites, diffraction theory predicts that the lines of the powder pattern will be exceedingly sharp ( breadths measured in seconds of arc). In actual experiments lines of such sharpness are never observed because of the combined effects of the following.

- i) spectral width of the incident beam.
- ii) instrumental factors.
- iii) composition fluctuations in the specimen.

The pure diffraction line profile  $f(\theta)$  therefore broadens to give an experimental profile  $h(\theta)$  which is plotted by the diffractometer.

$\text{Pb}(\text{Zr}_x\text{Ti}_{1-x})\text{O}_3$  has a perovskite structure and tetragonal symmetry in the composition range  $0 \leq x \leq 0.535$ . Fig. 3.1 [43] shows a relation between lattice constant and composition in this range. The lattice constant ' $a_T$ ' increases with the composition ' $x$ '. ' $c_T$ ' however does not depend on ' $x$ '. Therefore for a sample having a compositional inhomogeneity, ' $a_T$ ' will fluctuate but ' $c_T$ ' will not. As the spacing for  $hk0$  planes are fixed only by ' $x$ ' in  $\text{Pb}(\text{Zr}_x\text{Ti}_{1-x})\text{O}_3$ , compositional fluctuations will cause a dilation or contraction in the lattice parameter  $\Delta a_T$ . The strain  $\frac{\Delta a_T}{a_T}$  can be estimated from the slope of the relation between  $\beta \cos \theta$  and  $\sin \theta$  for  $hk0$  diffractions as the slope equals  $\Delta a_T/a_T$  [43].  $\beta$  is the broadening due to the compositional fluctuation only. From Fig. 3.1 and the value of  $\Delta a_T$  the composition fluctuation  $\Delta x$  is easily calculated.

A precise determination of  $\beta$  is therefore necessary to evaluate the composition fluctuation in the sample. Effectively this means that the pure diffraction profile  $f(\theta)$  must be extracted from the experimental profile  $h(\theta)$ . This operation is feasible because of the convolution relationship among  $h(\theta)$ ,  $g(\theta)$  and  $f(\theta)$  where  $g(\theta)$  is the profile due to the instrumental factor.

$$h(E) = \int_{-\infty}^{+\infty} g(\eta) f(E-\eta) d\eta \quad \dots\dots (3.1)$$

within certain mathematical limitations imposed principally by a) the presence of random experimental errors ('noise') in the curves  $h(E)$  and  $g(E)$  and b) the practical necessity of evaluating the integral of eqn.(3.1) over a finite rather than infinite angular range this equation can be deconvoluted more or less rigorously. The two methods most commonly applied to X-ray data are Fourier transformation (method of Stokes) and the iterative method of successive foldings of  $h(E)$  with  $g(E)$ ; both methods are discussed in [56]. In the present work only relative numerical results are useful and these sophisticated procedures have been circumvented because of the extensive and tedious computations involved. The deconvolution can be done by analytical procedures, substituting simple equations or graphs based on line profiles of assumed analytical form also.

### 3.2 Measure of line width:

The line width has been defined in literature in three different ways

- i) the half maximum width  $W_{\frac{1}{2}}$
- ii) the integral breadth  $W_i$
- and iii) the variance  $W_{2\sigma}$ .

Of these the most convenient to use, although the least amenable to mathematical analysis is  $W_{1/2}$ . Thus  $W_{1/2}$  is most generally employed for routine measurements when relative values suffice. The integral breadth,

$$W_i = \frac{1}{I_p} \int I(2\theta) d(2\theta) \quad \dots\dots (3.2)$$

is the width of a rectangle having the same area and peak height as the actual line profile.  $I_p$  is the maximum peak height of the profile. The variance,

$$W_{2\theta} = \frac{\int (2\theta - \langle 2\theta \rangle)^2 I(2\theta) d(2\theta)}{\int I(2\theta) d(2\theta)} \quad \dots\dots (3.3)$$

has important mathematical advantages, but its evaluation involves lengthy calculations and depends sensitively on the choice of background level with an attendant truncation operation. Where the profile has a long tail it is more reliable to use  $W_{1/2}$  as it is the least sensitive to the choice of background level. Each of the measures of line width is shown in Fig. 3.2.

### 3.3 Shape of the X-ray line Profile:

In simplified analytical deconvolution treatments it is necessary to make specific assumptions concerning the shapes of the line profiles  $h, g$  and  $f$  with the consequence that the derived  $\beta_{1/2}$  or  $\beta_i$  values have restricted absolute



significance. In the following discussion the breadths of h, g and f line profiles are for the sake of simplicity of notation designated B, b and  $\beta$  respectively with subscripts 1/2 or i as required.

#### Gaussian or Cauchy Profiles:

The two most commonly assumed line shapes are the Gaussian

$$I(E) = I_p(E) \exp (-K^2 E^2) \quad \dots (3.4)$$

and the Cauchy

$$I(E) = I_p(E)/(1+K^2 E^2) \quad \dots (3.5)$$

profiles. If h, g and f are all Gaussian, on application of the convolution integral; from eqn.(3.1) and eqn.(3.4),

$$B^2 = b^2 + \beta^2 \quad \dots (3.6)$$

for all Cauchy profiles

$$B = b + \beta \quad \dots (3.7)$$

These solutions are given in [56]. The relationships hold for both half maximum and integral breadths.

Actual line profiles are never pure Gaussian or pure Cauchy. The Gaussian shape has some justification in its usage for Debye-Scherrer setups as eqn.(3.4) constitutes a more realistic approximation of the instrumental

profile than does eqn. (3.5) particularly for low-absorbing specimens and/ or back reflection angles. However, the geometrical features of diffraction in a high-resolution parafofocussing diffractometer cause the g profile to depart widely from the Gaussian and become highly unsymmetrical . Assuming a Cauchy function in this case becomes more reasonable. For the present case the diffraction curves are assumed as intermediate between Gaussian and Cauchy.

After defining the half width and the assumptions usually made regarding the shape of the line profile, we revert to the discussion of how to obtain the corrected line broadening (3.4).

#### 3.4 Correction due to Spectral Width of the Incident Beam:

The angular separation 'd' between  $K\alpha_1$  and  $K\alpha_2$  is small at low Bragg angles but becomes progressively more important as  $\theta$  increases (Fig. 3.3, Ref.56). At sufficiently large angles it is often possible to circumvent this problem by measuring the separate profile of either the  $\alpha_1$  or  $\alpha_2$  line but this recourse fails if the pure diffraction broadening is too great. Rachinger's method [57] of correction provides good reliability without excessive computational labour. Corrections of slightly less accuracy but still sufficiently good is more conveniently applied by reference to correction curves based on profiles of certain standard shapes, for e.g., those of Fig. (3.4). The curves in Fig.(3.4) are as follows.

- A  $\longrightarrow$  Jones' curve for the integral breadths of back reflection Debye-Scherrer f and g profiles of a particular arbitrary shape [58]. Here Jones postulated that the  $K\alpha_1$  and  $K\alpha_2$  profiles are usually similar figures having an intensity ratio of 2:1. He then showed that the sum of the two profiles divided by the height of the composite maximum is the observed integral breadth. A is the correction curve obtained in this way .
- C  $\longrightarrow$  Correction curve for f(E) and g(E) , both Gaussian.
- D  $\longrightarrow$  Correction curve for f(E) and g(E), both Cauchy.
- E  $\longrightarrow$  Correction curve for f(E) and g(E), both intermediate between the Cauchy and Gaussian shapes.

Unlike curve A, curves C,D and E refer to breadths at half-maximum intensity  $W_{1/2}$ . Of these curves A and E have greater general applications. In the present analysis the half-maximum intensity  $W_{1/2}$  has been used considering the tails of the profiles. As E is particularly suitable in diffractometry, the author has used this curve in his line profile analysis.

### 3.5 The Powder Diffractometer :

The broadening due to the instrument is due to the combined effect of several weight functions. For a better understanding of these functions it will be useful to take a closer look at the diffraction equipment used i.e. the powder diffractometer.

Nearly all modern day diffractometers have the parafofocussing arrangement i.e. the receiver G pivots about the sample S (Fig. 3.5), thus maintaining a constant sample-to-receiver distance SG. In order to accomplish this end, the sample surface is made flat rather than curved, and it is caused to rotate with one-half the angular velocity with which the receiver revolves, so that the sample surface remains tangent to the focussing circle at all points. As G pivots about S toward larger angles,  $2\theta$ , the radius of the focussing circle decreases. Thus as shown in Fig. 3.5, the focussing circle has the respective radii  $r_1, r_2$  and  $r_3$  for reflections at the deviation angles  $2\theta_1, 2\theta_2$  and  $2\theta_3$ . For  $2\theta = 0^\circ$ ,  $r = \infty$  whereas at  $2\theta = 180^\circ$ ,  $r$  reaches a minimum value of  $\frac{SF}{2} = \frac{SG}{2}$ .

The plane of Fig. 3.5 is called the equatorial or focussing plane, and the perpendicular direction which is parallel to the goniometer axis is the axial direction. The focus at G is not perfect for several reasons. In particular, parafofocussing errors result from the use of a flat rather than curved sample, from sample 'transparency' (low absorption coefficient), and from the axial direction properties of the system (finite dimensions of the sample, source, slits etc in the axial direction). Each of these error introducers are dealt with in a later section. However by limiting the

equatorial divergence of the primary beam, and by restricting the axial dimensions of the X-ray optical system in various respects, the aberrations are kept small.

Fig. 3.6 shows the optical arrangement of a typical present day diffractometer. The focal spot is viewed laterally, so that the apparent source width is only  $w \sin \alpha$ , where  $\alpha$  is normally 3 to 6°. An X-ray source of such narrow projected width is often referred to as a line source. The equatorial divergence is limited by the dimension  $x$  of the aperture  $X$ , whereas the axial divergence, instead of being prescribed by the heights  $h$  of the source and  $y$  of the divergence slit, is more drastically limited by employing two Soller slit collimators  $S_1$  and  $S_2$  for the incident and diffracted beams, respectively.

The background is improved by placing an anti-scatter slit at either position  $M$  or  $M'$  (Fig. 3.6) which excludes from the receiver all X-rays except those emanating from the specimen. The Soller plates are made of some metal of high atomic number to minimise the possibility of K fluorescence, which tend to increase the background level.

The step scanning method of recording a diffraction pattern with some form of digital resistration of the output counts enable the determination of interplanar spacings and broadening function with the highest

accuracy because this technique makes possible a statistical evaluation of the precision of the results. However as this recording mode facility was not available to the author he has made use of the continuous mode of measurement with very slow scanning speeds in his experiments which too provide a means of obtaining diffraction results of nearly comparable accuracy.

### 3.6 The Instrumental Weight Functions:

In the previous section it was mentioned that an instrumental factor introduces its own line profile  $g(E)$  which broadens the pure diffraction line profile  $f(E)$  to the experimental profile  $h(E)$ . The contributions that form  $g(E)$  by convolution synthesis are discussed below.

$$g(E) = \widehat{g_I} \widehat{g_{II}} \widehat{g_{III}} \widehat{g_{IV}} \widehat{g_V} \widehat{g_{VI}} \widehat{g_{VII}} \dots (3.8)$$

These factors which decrease the resolution (increase breadth of line profile) are not dependent on the scanning technique employed. Eqn. (3.8) may be evaluated by performing the five constituent folds in any order.

#### A. X-ray Source, $g_1$ :

This is the most important among the instrumental weight functions at lower resolution geometries. As the resolution increases this factor starts to get dominated by other instrumental weight functions. The projected focal spot

profile in this case may be approximated by a Gaussian intensity function,

$$g_1 = \exp(-K_1^2 E^2) \quad \dots (3.9)$$

#### B. Flat Specimen Surface, $g_{II}$ :

This function arises from the varying displacements of different portions of the flat specimen surface from the focussing circle to which it is tangent. The profile assumes the form

$$g_{II} = |E|^{-1/2} \quad \dots (3.10)$$

$g_{II}$  has the effect of displacing the line profile in the  $-E$  direction, i.e. to a smaller  $2\theta$  value. The flat specimen effect is minor except at small Bragg angle or when the horizontal beam divergence  $\gamma$  is large.

#### C. Axial Divergence, $g_{III}$ :

Though the profile of this function is in principle determinate, in actual practice the complexity of the calculations is so great that the profiles have been calculated only for simplified situations. Fig. 3.4 shows representative axial divergence profiles corresponding to  $2\theta = 24^\circ$  and a specimen linear absorption coefficient  $\mu = 34 \text{ \AA}^{-1}$ . For diffractometers without Soller slits

$$g_{III} = |2E \cot \theta|^{-1/2} \quad \dots \quad (3.11)$$

Although the form of  $g_{III}$  is different for diffractometers with and without Soller slits, in either situation the magnitude of the line distortion is greatest at very small values of  $2\theta$  and shrinks with increasing  $2\theta$  until it is near zero in the general range  $90^\circ < 2\theta < 120^\circ$ , and increases again at still larger angles. Below  $90^\circ$  the displacement of the line profile is in the  $-E$  direction, whereas in the back reflection region it is in the  $+E$  direction.

#### D. Specimen Transparency, $g_{IV}$ :

This weight function arises from the penetration of the specimen having finite absorption coefficient  $\mu$  by the beam. When the specimen is sufficiently long to intercept the entire direct beam at the particular incident angle concerned, and when the thickness  $t$  of the specimen satisfies the condition

$$t \geq \frac{3.2}{\mu} \frac{P}{\rho'} \sin \theta \quad \dots \quad (3.12)$$

( $\rho$  and  $\rho'$  are, respectively, the densities of the solid material composing the powder and that of the powder including interstices); a diffraction beam of maximum intensity is generated.

$$g_{IV} = \exp (K_{IV} E) \quad \dots \quad (3.13)$$



$$\text{where } K_{IV} = \frac{4\mu R}{114.6} \sin 2\theta \quad \dots (3.14)$$

for  $\theta$  expressed in degrees of arc,

$R$  = sample to source distance = sample to receiver distance.

In eqn. 3.13  $\theta$  varies between the limits 0 and  $-\infty$ .

The influence of the specimen transparency function is greatest for thick specimens with small absorption coefficients for X-rays.

#### E. Receiving Slit, $g_V$ :

As shown in Fig. 3.7, this function is evidently a rectangle in profile with a width  $w_s$  equal to the angle subtended by the receiving slit at the center of the goniometer arc. For any given angular position  $\theta$ , it covers the range from  $\theta - \left(\frac{w_s}{2}\right)$  to  $\theta + \left(\frac{w_s}{2}\right)$ . This function assumes a less important role in diffractometers with narrow sources and narrow slits though the resolution is not much affected by employing a slit width somewhat greater than the source width, for instance, as wide as 0.05.

#### F. Misalignment $g_{VI}$ :

This function arises because of the probability of a certain residual degree of misalignment in any well adjusted diffractometer. The residual deficiency in focus arises from either the limiting mechanical imperfections

of the instrument or the extreme difficulty in synchronising the numerous variables of the alignment process. It was empirically found in most cases that

$$g_{VI} = 1/(1+K_{VI}^2 E^2) \quad \dots (3.15)$$

where  $K_{VI} = 2/W_{VI}$ ,  $W_{VI}$  = angular width of misalignment profile at half-maximum intensity

#### G. Spectral Dispersion, $g_{VII}$ :

This function arises because of the natural spectral dispersion of the characteristic X-radiation employed. For a pure spectral line such as  $K\alpha_1$  or  $K\alpha_2$  or for the unresolved  $K\alpha$  doublet at low Bragg angles, this function may be assigned the Cauchy form,

$$g_{VII} = 1/(1+K_{VII}^2 E^2) \quad \dots (3.16)$$

as a first approximation. In eqn. (3.10)  $K_{VII} = \frac{2}{w_{VII}}$ ,  $w_{VII}$  being the angular width of the spectral profile at half-maximum intensity. The width is proportional to  $\tan \theta$  and is therefore small at low Bragg angles. For  $CuK\alpha$  radiation, Ekstein et al [59] give  $w_{VII} = 0.0424 \tan \theta$ .

### 3.7

The convolution calculations in X-ray diffractometry lead to two limiting curves for low and high Bragg angles (Fig. 3.8) [56,60].

1. At low angles, spectral breadth is insignificant.
2. At high angles, spectral breadth is important.

Details of the convolution synthesis of line profiles under these conditions are given in [61]. At low or moderate Bragg angles, the instrumental profile  $g(E)$  is produced by the joint action of several factors of approximately equal weight. Since some of the factors are asymmetric, the resulting low-angle profile is also more or less asymmetric, this effect being greatest at the smaller angles where the asymmetric factors have the most weight. The convolutions of such profiles with pure diffraction profiles  $f(E)$  of various breadths lead to the correction curve designated 'low angle reflections' in Fig. 3.8. These curves are valid to the extent that the  $f(E)$  profiles approximate the Cauchy form, though not fully and when there is a small difference between the curves for half-maximum and integral breadths. As both factors are sufficiently true for profiles  $f(E)$  in PZT samples and because the hKO peaks selected in these specimens are all between  $21^{\circ}$ - $70^{\circ}$  (in the low angle region), the low angle curve is used in the present calculations.

At high Bragg angles broadening due to the various instrumental factors becomes small in relation to broadening resulting from the natural spectral distribution

in the radiation. To a fair approximation a pure spectral line such as  $K\alpha_1$  or  $K\alpha_2$  may be assigned a Cauchy profile. This means that to a first approximation at large Bragg angles the observed profile is simply the convolution of two Cauchy profiles ( $1/(1+K^2\theta^2)$  profiles), one due to the composition fluctuations in lead-zirconate-titanate as mentioned before and the other to the spectral distribution of the incident radiation. Computation of a series of such convolutions yields the result labeled 'back-reflections' in Fig. 3.8. This correction applies to both widths at half-maximum intensity and integral breadths. It is equivalent to

$$\frac{c}{B} + \frac{b}{B} = 1$$

which reduces to the simple additivity rule of equation 3.7. However, for reasons mentioned before this curve does not find usage in the present analysis.

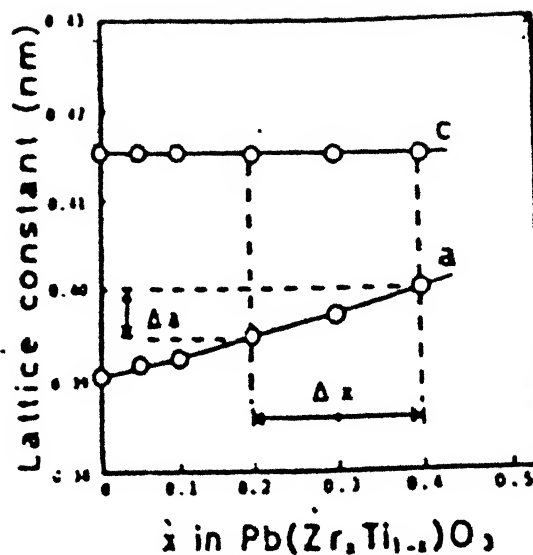


Fig. 3.1 Relation between lattice constants and composition of  $\text{Pb}(\text{Zr}_x\text{Ti}_{1-x})\text{O}_3$ .

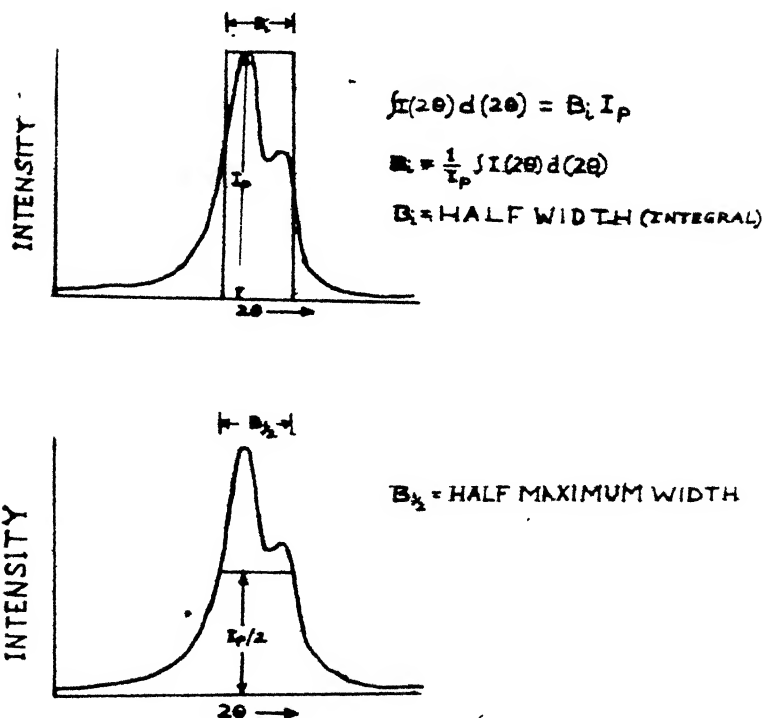


Fig. 3.2 Line breadth measures of diffraction profiles.

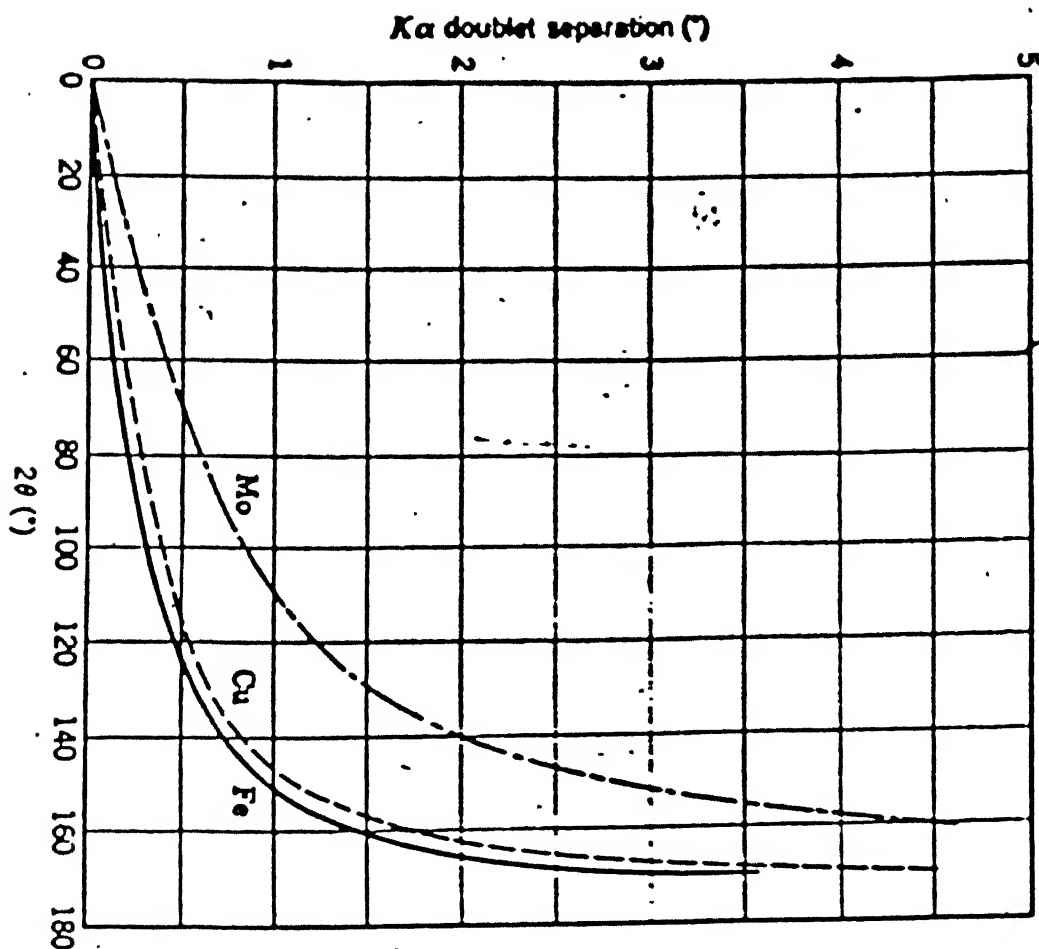


Fig. 3.3 Angular separation of the  $K\alpha$  doublet as a function of  $2\theta$  for three common radiations.

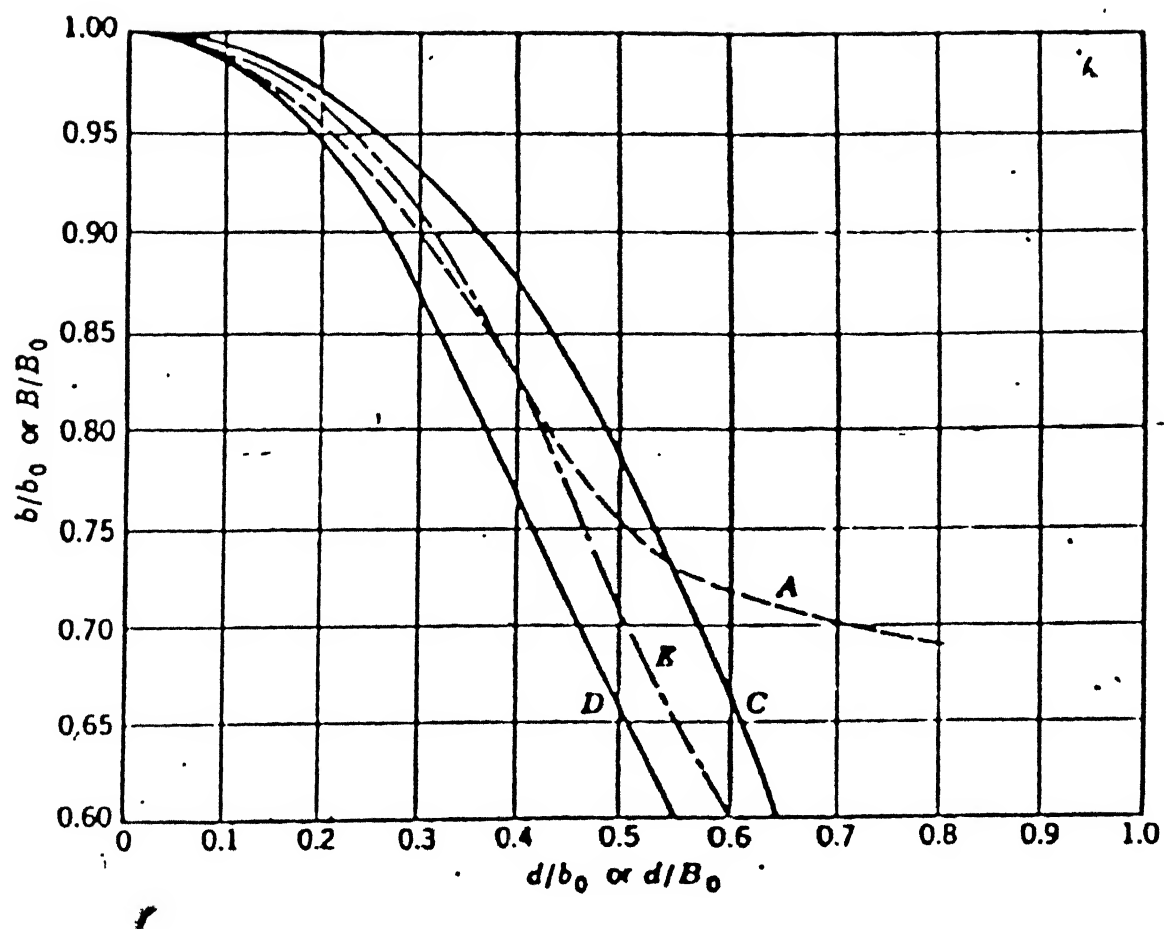


Fig. 3.4 Curves for correcting line breadths for  $K\alpha$ -doublet broadening.

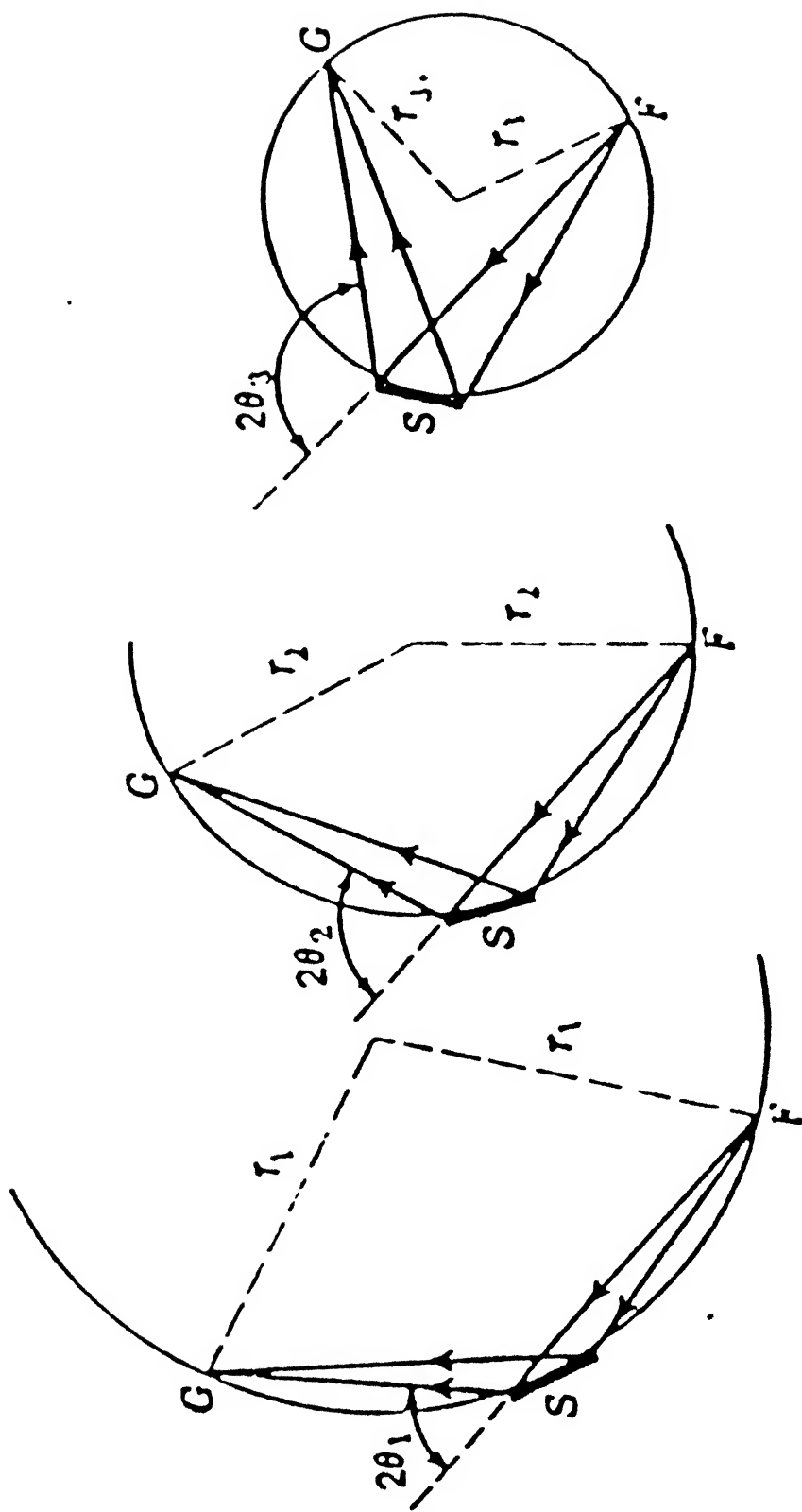


Fig. 3.5 Parafocussing arrangement used in the powder diffractometer •



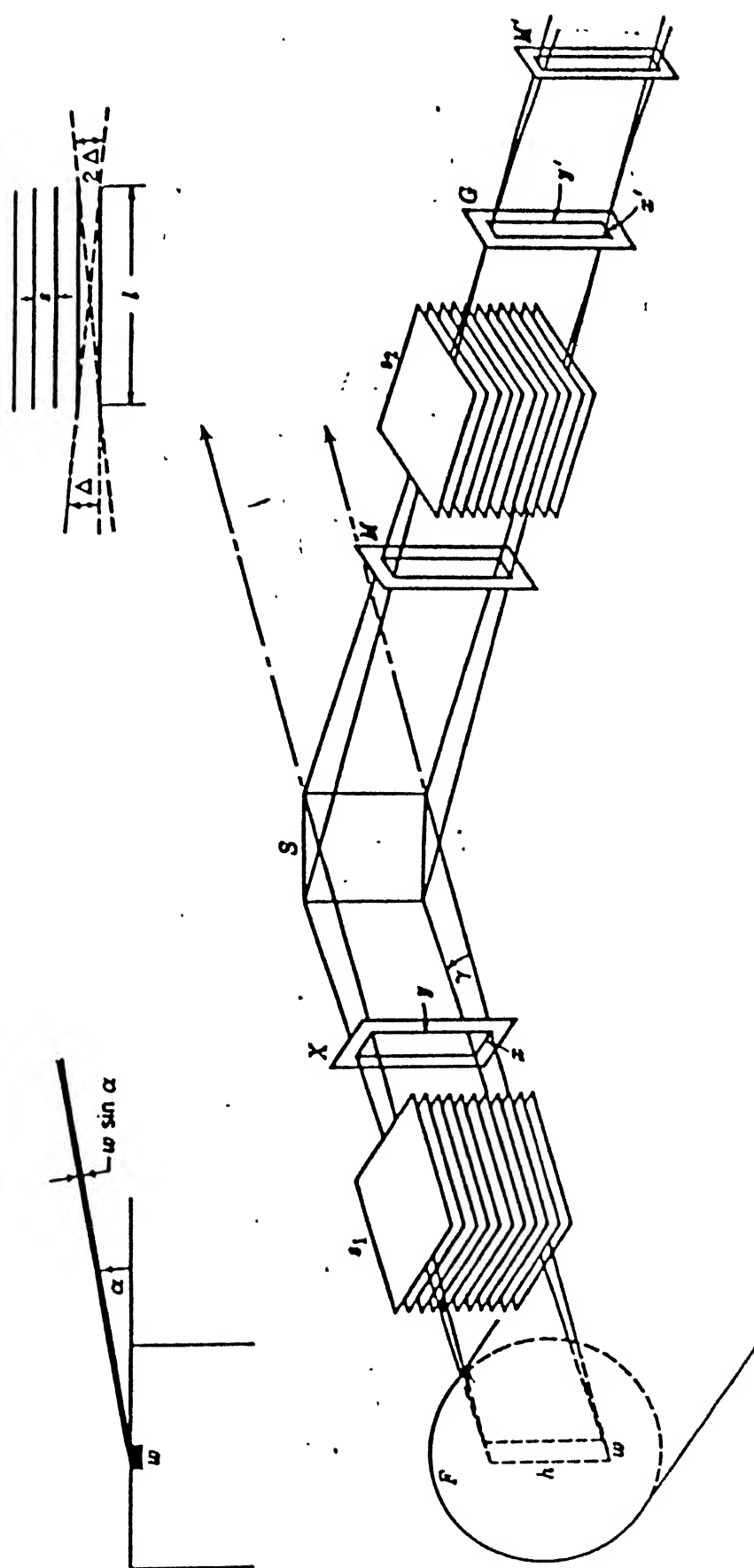


Fig. 3.6 Optical arrangement in a diffractometer with a 'line' X-ray source and slits to limit axial divergence.

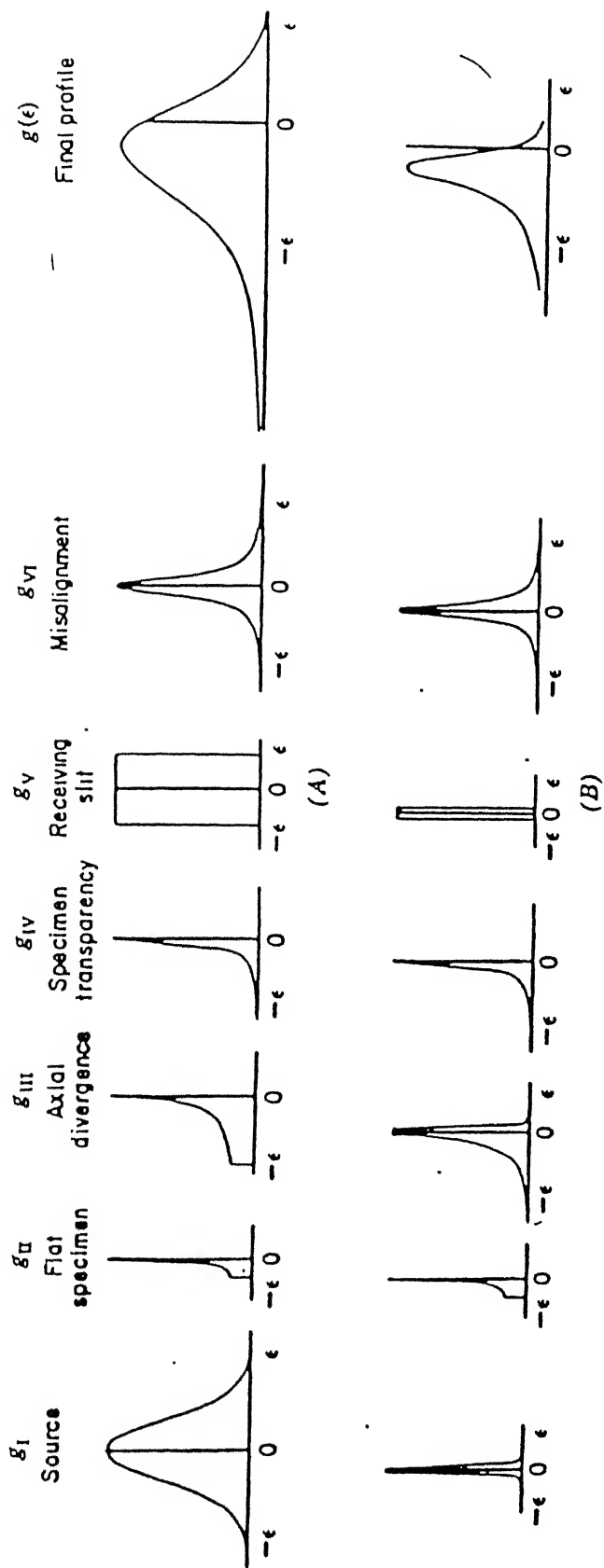


Fig. 3.7 Instrumental weight functions for diffractometers employing (A) low resolution and (B) high resolution geometry computed for  $2\theta = 24^\circ$ ,  $\mu = 34\text{cm}^{-1}$ .

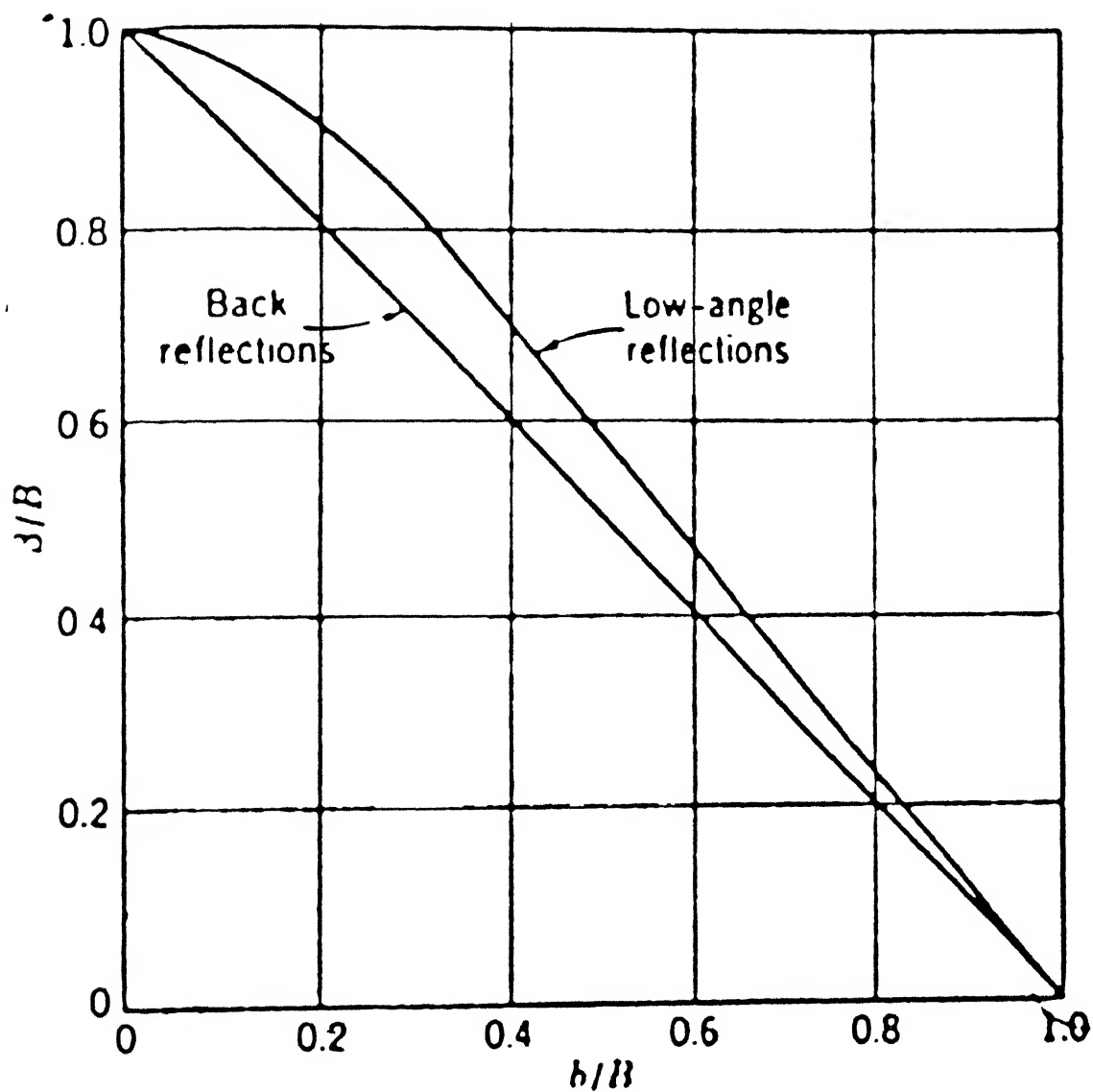


Fig. 3.8 Curves for correcting X-ray diffractometer line breadths due to instrumental broadening.

## CHAPTER 4

### THE PRESENT WORK

Though a lot of research has been done to ascertain the reaction sequence occurring during the calcination process; strangely, none of the investigations have viewed this step as contributing to the inhomogeneity in lead zirconate-titanate.

Knowing the dependence of the mechanical and piezoelectric properties on the Zr/Ti ratio and realising the importance of the calcination process towards homogenisation, the author felt the need for determining composition fluctuations of  $\text{Pb}(\text{Zr}_x\text{Ti}_{1-x})\text{O}_3$  prepared under various calcination conditions. The inhomogeneity is measured by a simplified treatment of the line profile method in the present work. The measured composition fluctuation is then compared with variations in the values of the measurable piezoelectric constant ' $d_{33}$ ' for samples of each specimen set using a statistical correlation analysis. A PZ+Z packing powder composition is used during the sintering process so that each sample equilibrates to a PbO content. Composition variations in samples prepared under different sintering conditions are also measured.

Investigations regarding the grain size and shape and the presence of second phase particles are achieved through scanning electron microscopy.

## CHAPTER 5

### EXPERIMENTAL PROCEDURE

#### 5.1 SAMPLE PREPARATION

##### 5.1A Raw Materials :

The raw materials used for the preparation of PZT samples and the atmosphere powder were as follows

Table 5.1 A

Details of Chemicals used in Experiments

Chemical	Purity	Manufacturer
Lead Oxide (yellow) (PbO)	99.0%	Fluka Gerantie Switzerland
Zirconia ( $ZrO_2$ )		
Average particle size 1.5 $\mu$ m	99.5%	Indian Rare Earth Ltd (IRE) Kerala
Titania ( $TiO_2$ )	>99%	Fluka Gerantie Switzerland

### 5.1 B. Preparation of Packing Powder:

A PZ+Z powder was chosen as the atmosphere powder during calcination and sintering of the lead zirconate titanate samples.

Table 5.1 B

Chemical Composition of Packing Powder

PbO			ZrO <sub>2</sub>		
Molar ratio	Molecular weight	Weight %	Molar ratio	Molecular weight	Weight %
C.27	223.19	40.12	0.73	123.22	59.82

A 250 gm batch was wet ball milled in a plastic jar with alumina balls as milling media for 5 hours. Isopropanol was used in preparing the slurry. The balls filled 45% of the plastic jar in a random packing arrangement. The slurry and the milling media filled approximately 70% of the mill. The mill was run at 55% of its critical speed (85 rpm).

$$\text{The critical speed} = \frac{42.2}{\sqrt{D-d}} \text{ rpm (155 rpm) ... (5.1)}$$

where  $(D - d)$  is in metres.

The slurry obtained after ball milling was dried over a magnetic stirrer thoroughly at about 60°C. The dried, cake like mass was broken up and passed through a 20 mesh sieve. The sieved powder was calcined in recrystallised alumina crucibles at 860°C for 5 hours. The calcined powder was again sieved through a 60 mesh sieve. A fast XRD scan of this powder confirmed the presence of lead zirconate and zirconia phases only. The prepared powder was thus ready to be used as the atmosphere powder during the calcination and sintering of the PZT samples. It was stored in a plastic jar and kept inside a dessicator to prevent granulation.

#### 5.1C Preparation of Lead Zirconate Titanate Samples:

PZT samples of the composition given in Table 5.1C were prepared by the standard ceramic processing route.

Table 5.1C

Chemical Composition of Fabricated PZT specimens

PbO			ZrO <sub>2</sub>			TiO <sub>2</sub>		
Molar ratio	Mol. wt.	Wt%	Molar ratio	Mol. wt.	Wt%	Molar ratio	Mol. wt.	Wt%
1.00	223.21	68.73	0.50	123.22	18.97	0.50	79.90	12.30



750 gms of the sample powder, in three, batches were ball milled and dried in exactly the same way as described in 5.1B. Each batch mixture was then passed through a 20 mesh sieve. The sieved powder of each batch mixture was then mixed together.

Nine sets of  $\text{Pb}(\text{Zr}_{0.5}\text{Ti}_{0.5})\text{O}_3$  samples were prepared. The calcination and sintering conditions of each set is given in Table 5.1D. Each set consisted of 4 pellets and 2 discs. The schedule in Table 5.1D was designed to study the effects of calcination and sintering times and temperatures.

Table 5.1D

Calcination and Sintering Conditions for the  
Specimen sets

Sample	Calcination		Sintering	
	Temperature (°C)	Time (hr)	Temperature (°C)	Time (hr)
A	760	1.0	1260	1.0
B	860	1.0	1260	1.0
C	960	1.0	1260	1.0
D	860	2.5	1260	1.0
E	860	5.0	1260	1.0
F	860	1.0	1260	4.0
G	860	1.0	1260	7.0
H	860	1.0	1100	1.0
I	860	1.0	1350	1.0

The calcination assembly in shown in Fig. 5.1a calcined powders of each set which formed an agglomerated mass after calcination were crushed in polythene bags and ground in an agate mortar. They were then sieved through a 60 mesh sieve and then made into a slurry with isopropanol. A PVA binder solution (1.5% by wt) was then added to the slurry. For each gram of PZT in the slurry, 0.005 gms of PVA was added. The slurry for each specimen set was magnetically stirred at 60°C till it was completely dry. The resulting cake masses were broken up and crushed in agate mortars. The crushed powder was passed through a 100 mesh screen in each case. These powders were then stored in separate plastic jars and then kept inside a dessicator.

The -100 mesh powders in each samples were pressed at 8.5 tons for 1 minute in a die of diameter 0.5 inch. Pellets of 2 cm thickness were formed. For Vickers hardness measurements, disc shaped samples were pressed. The discs were 1 inch in diameter and 0.7 cm in thickness. Pressing in this case was done at a pressure of 9.5 tons.

The prepared pellets were dried in an oven at 60°C for a day before loading them into the furnace for sintering. The entire sintering assembly is shown

in Fig. 5.1b. The diagram is self explanatory. The furnace was heated to the sintering temperature at about  $200^{\circ}\text{C}/\text{hour}$ . However the temperature was kept constant at  $120^{\circ}\text{C}$  for 2 hours and  $560^{\circ}\text{C}$  for 4 hours to drive out adsorbed water and binder respectively before soaking the sample at the sintering temperature. The cooling down to room temperature consisted of cooling in the furnace from the sintering temperature to  $1000^{\circ}\text{C}$  in about one hour, cooling to  $500^{\circ}\text{C}$  in about one and a half hours and then switching off the furnace for further cooling.

## 5.2 XRD Analysis:

The specimen for XRD analysis was made by grinding the sintered sample in an agate mortar to a fine powder and sieving. Powder of -60 mesh and +100 mesh were packed into a square perspex sample holder. The powder surface was smoothed by passing a glass slide back and forth over it. A REICH SEIFERT ISO DEBYEFLEY 2002 DIFFRACTOMETER was used in the analysis.  $\text{CuK}_{\alpha}$  ( $\lambda = 1.5405\text{\AA}$ ) radiation was used.

The X-ray diffraction plots of the sample were taken in the  $2\theta$  range of  $20^{\circ}$  to  $70^{\circ}$  with the following operating conditions

Table 5.2

Operating Conditions of Diffractometer during X-ray  
diffraction

Current,voltage	- 30 mA, 40KV
Time constant	- 10 seconds
Beam slit width	- 1.5 mm.
Detector Slit width	- 0.3 mm.
Scanning speed (2 $\theta$ )	- 0.6°/minute
Chart speed	- 15 mm/ minute
Full scale intensity	- 10K counts/ minute

#### 5.2A Measurement of Lattice Parameters:

From the peak position, phases of PZT were identified and lattice parameters were calculated as follows (62,63).

$$\text{Tetragonal: } \sin^2\theta = \frac{\lambda^2}{4} \left[ \frac{h^2+k^2}{a_T^2} + \frac{l^2}{c_T^2} \right] \dots (5.2)$$

Rhombohedral: For this system, the interplanar spacing is given as

$$\frac{1}{d^2} = \frac{(h^2+k^2+l^2)\sin^2\alpha + 2(hk+kl+hl)(\cos^2\alpha - \cos\alpha)}{a_R^2(1-3\cos^2\alpha + 2\cos^3\alpha)} \dots (5.3)$$

The lattice parameter determination using the above equation is tedious. Therefore, calculation was performed, indirectly from the lattice parameter values of the hexagonal system.

If H,K and L and h,k,l are Miller indices in the hexagonal and rhombohedral systems, respectively, then these are related as

$$H=h-k, K=k-l \text{ and } L=h+k+l.$$

The lattice parameters  $a_H$  and  $C_H$  for the hexagonal system are related by the equation,

$$\sin^2 \theta = \frac{\lambda^2}{4} \left[ \frac{4}{3} \left( \frac{H^2+HK+K^2}{a_H^2} \right) + \frac{L^2}{C_H^2} \right] \quad \dots (5.4)$$

This equation can be solved for  $a_H$  and  $C_H$  by using data for any two rhombohedral peak position. From the values of  $a_H$  and  $C_H$ ;  $a_R$  and angle  $\alpha$ , the angular distortion is calculated as

$$a_R = \frac{1}{3} (3 a_H^2 + C_H^2)^{1/2} \quad \dots (5.5)$$

$$\text{and } \sin \left( \frac{\alpha}{2} \right) = \frac{3}{2[3+(C_H/a_H)^2]^{1/2}} \quad \dots (5.6)$$

In equations (5.4), (5.5) and (5.6) ,

= wavelength of radiation employed

$\theta$  = diffraction angle.

h,k,l = Miller indices of the corresponding reflecti  
planes.

$2\theta$  values was made using the method of least squares to obtain the resolution width of the instrument at any angle.

The line breadths for the  $(100)_T$ ,  $(200)_T$  and  $(220)_T$  reflections for  $\text{Pb}(\text{Zr}_{0.5}\text{Ti}_{0.5})\text{O}_3$  samples were then measured.  $(B_0)$  and the ratio  $\frac{d}{B_0}$  calculated in each case. From curve E in Fig. 3.4 the value of  $\frac{B}{B_0}$  and hence  $B$  was then determined. From the  $b$  vs  $2\theta$  plot of the Silicon standard, the value of ' $b$ ' for the particular diffraction angle was then found. Knowing the ratio  $\frac{b}{B}$  the value of the corrected line breadth ( $\beta$ ) was obtained from Fig. 3.9 from the low angle reflection curve. A  $\beta \cos \theta$  vs  $\sin \theta$  plot was fitted into a linear equation by the method of least squares. The slope of the line gave the strain  $\frac{\Delta a_T}{a_T}$  in the lattice due to compositional fluctuation. As  $a_T$  is known (5.1) the value of  $\Delta a_T$  was calculated easily. From the value of  $\Delta a_T$  and Fig. 3.1 the composition fluctuation  $\Delta x$  was calculated. An illustration of the composition fluctuation calculation is given in Appendix 4.

### 5.3 Scanning Electron Microscopy:

Samples for SEM characterisation were prepared by cutting discs; 1 mm in thickness, using a diamond rimmed circular blade. The discs were then polished in 3/0 emery paper and cleaned with acetone in an ultrasonic bath. The discs were then mounted on an aluminium stub using a silver paint. For each sample the exposed disc face which was

to be viewed was gold coated using a PS-2 coating unit ( International Scientific Instrument). The coating conditions were as follows:

Current	-	10 mA.
Voltage	-	14 KV
Pressure	-	$10^{-1}$ Torr.
Time	-	1.5 minutes.

The sample microstructure were viewed through a JEOL 840A SEM. Sample micrographs in both secondary and back scattered electron modes were taken. The mean diameter of PTT grains was determined by the line intercept method. X-ray mapping was used to determine the presence of a second phase, if any.

#### 5.4 Piezoelectric Measurements:

##### A. $d_{33}$ measurement:

Disc shaped samples of 1 mm thickness were cut, polished and cleaned as mentioned in 5.3 Nailpolish was then put on the edges of the discs. The discs were then gold coated on both surfaces in the PS-2 coating unit under conditions identical to 5.3 except that the coating time for each face was 18 minutes.

After the surfaces were gold coated, nailpolish from the disc edges was removed by rubbing with acetone. Using a multimeter the continuity of each surface and the discontinuity between the two surfaces was checked.

The resistances measured between the multimeter probes were 40 to 150  $\Omega$  and 1 M respectively. A strong electric field was then applied to the discs placed tightly between a brass cathode and an aluminium anode using a fixture schematically shown in Fig. 5.2.

To avoid dielectric breakdown, the whole fixture was put in a beaker containing silicone oil. The beaker was heated and a constant temperature of the liquid was maintained using a 2MLH MAGNETIC STIRRER (REMI INSTRUMENTS). The poling field was along the thickness. The following poling conditions were adhered to.

Applied field	-	3.5 KV/ mm.
Temperature	-	110°C
Time	-	30 minutes.

When the temperature reached about 100°C, the electric field was switched on and after holding at a temperature of 110°C for 30 minutes, the sample was cooled by switching off the heater with the field on. When the temperature reached the room value, the field was switched off. To ensure rapid cooling to room temperature, the beaker containing the poling fixture was transferred to an ice bath with the field on. Cooling to room temperature



took about 7-8 minutes.

The discs were then taken out of the poling fixture and silicone oil was removed by gently rubbing with cotton, care being taken not to remove the gold coating. The poled samples were then kept for 24 hours after which  $d_{33}$  measurements were made. A Channel Products, Belincourt  $d_{33}$  meter was used for  $d_{33}$  measurements, at 100 Hz.

#### B. Measurement of Resonance and Antiresonance Frequencies:

It was attempted to measure these frequencies using the dynamic method principle; a 4194A impedance/gain phase analyser (Hewlett-Packard) was employed.

#### 5.5 Vickers hardness Measurement:

Discs of 1'' diameter and 0.7 mm thickness were taken and polished successively in 2/0, 3/0 and 4/0 grade emery paper and finally lapped on a polishing wheel using 0.3 micrometer alumina powder. Care was taken to ensure that the opposite faces of the discs were exactly parallel, and the surface on which indentations were to be made had a high reflectance. Each polished disc had a thickness of 0.4 mm.

Indentations were carried out on a Vicker's testing machine having a load range of 1 to 30 kg and using a load of 2.5 kg. The length of the diagonals of each indentation were measured by an image analyser used in conjunction with a Bausch and Lomb microscope fitted to the hardness machine at a magnification of 100X. The Vicker's hardness number ( $H_V$ ) was calculated using the formula (63)

$$H_V = \frac{1.8544P}{(2a)^2} \quad \dots (5.7)$$

where  $P$  is the load in kg and  $(2a)$  is the diagonal length in mm.

#### 5.6 Density and Porosity Measurements:

The sintered density and the percentage open porosity of the prepared  $\text{Pb}(\text{Zr}_x\text{Ti}_{1-x})\text{O}_3$  samples were measured by the water displacement method.

The moisture present in the samples was eliminated by heating in an oven at  $150^\circ\text{C}$  for half an hour. The initial dry weight ( $W_1$ ) of the sample was taken using a ACFORSET ER-120A ELECTRONIC BALANCE.

The sample was then immersed in a boiling water bath for two hours in order to allow water to enter into the pores of the sample. The bath was then allowed

to cool and the weight of the sample suspended in water ( $W_2$ ) was taken. The sample was then taken out and dabbed with tissue paper and cotton. The weight of the sample, saturated with water was finally taken. The sintered density and open porosity were calculated from the following relation.

$$\text{SINTERED DENSITY} = \frac{W_1}{W_1 - W_2} \quad \dots (5.8)$$

$$\% \text{ OPEN POROSITY} = \frac{W_3 - W_1}{W_3 - W_2} \times 100. \quad \dots (5.9)$$

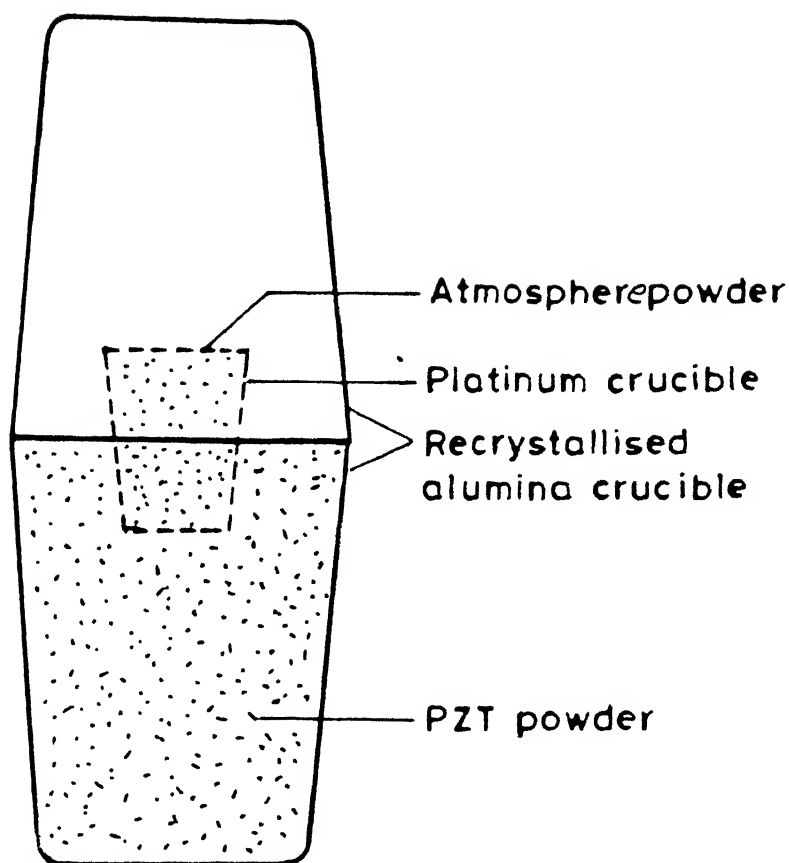


Fig. 5.1(a) Schematic diagram of crucible arrangement during calcination.

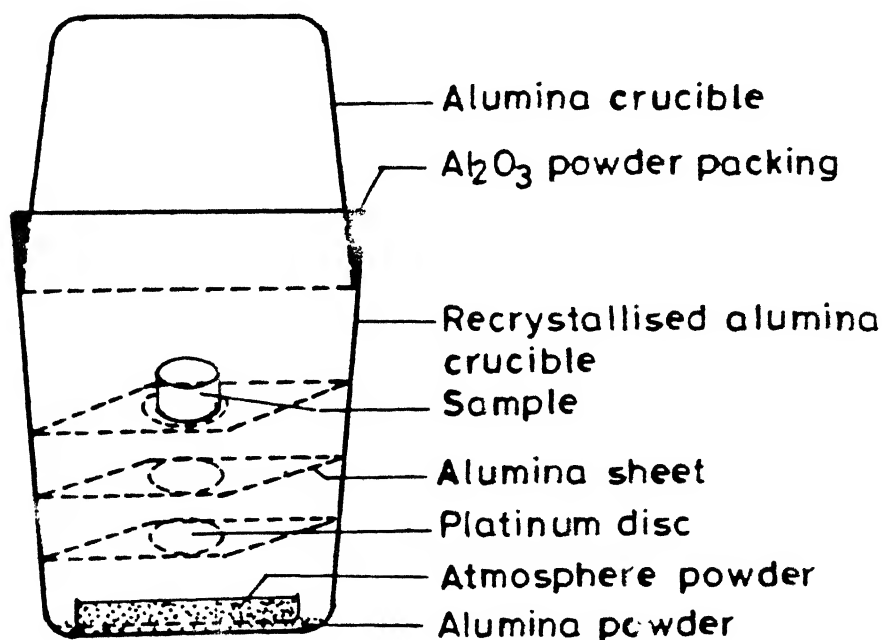


Fig. 5.1(b) Schematic diagram of crucible arrangement during sintering.

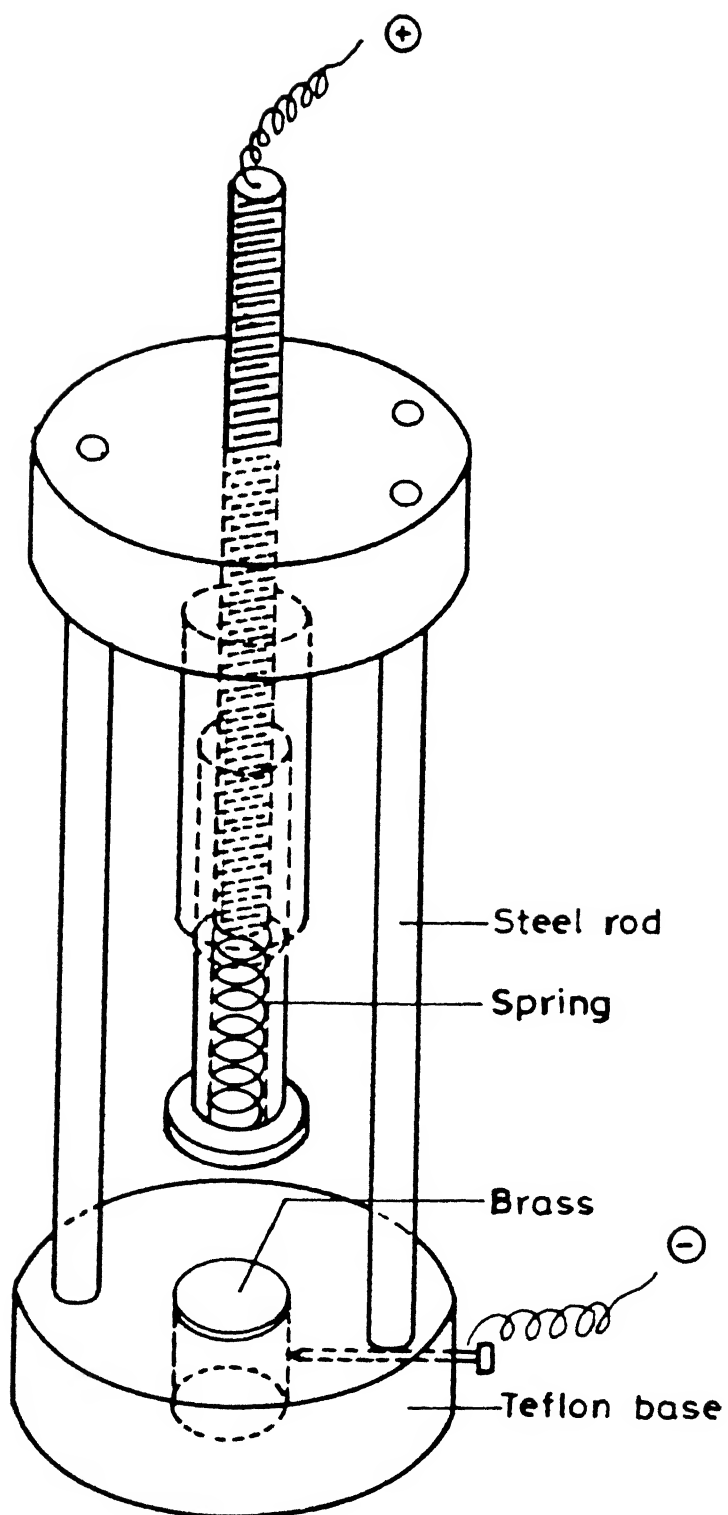


Fig. 5.2 Fixture used for poling PZT specimens.

## CHAPTER 6

### RESULTS AND DISCUSSION

Table 6.1A

1) LATTICE PARAMETERS OF  $\text{Pb}(\text{Zr}_{0.5}\text{Ti}_{0.5})\text{O}_3$  SPECIMENS CALCINED

## AT VARIOUS TEMPERATURES.

(Calcination time 1 hour, sintered at  $1260^\circ\text{C}$ , 1 hour)

Sample	Calcina- tion tempera- ture ( $^\circ\text{C}$ )	Phases		Tetragonal			Rhombohedral		
		hkl	2 $\theta$	$c_T$ ( $\text{\AA}$ )	$a_T$ ( $\text{\AA}$ )	$c_T/a_T$	hkl	2 $\theta$	$a_R$ ( $\text{\AA}$ )
A	760	Tetra- gonal + Rhomb- ohedral	(002) T	43.57	4.151	4.025	(200) R	44.31	4.087
			(200) T	45.01			(102) R	49.91	
B	860	Tetra- gonal + Rhomb- ohedral	(002) T	43.68	4.141	4.026	(200) R	44.30	4.083
			(200) T	45.00			(102) R	49.84	
C	960	Tetra- gonal + Rhomb- ohedral	(002) T	43.68	4.141	4.027	(200) R	44.36	4.089
			(200) T	44.98			(102) R	49.82	
									90.04
									89.98
									89.82

Table 6.1A

(ii) LATTICE PARAMETERS OF  $\text{Pb}(\text{Zr}_{0.5}\text{Ti}_{0.5})\text{C}_3$  SPECIMENS CALCINATED AT VARIOUS TIME  
(Calcination temperature =  $860^\circ\text{C}$ , Sintered at  $1260^\circ\text{C}$ , 1 hour)

Sample	Calcination time	Phases	Tetragonal			Rhombohedral			$a_R$ (Å)	$\alpha$
			hkl	2 $\theta$	$c_T$ (Å)	$a_T$ (Å)	$c_T/a_T$	hkl	2 $\theta$	
B	1 hr.	Tetragonal + Rhombohedral	(002) <sub>T</sub>	43.68	4.141	4.026	1.029	(200) <sub>R</sub>	44.51	89.98
			(200) <sub>T</sub>	45.00 <del>44.93</del>				(102) <sub>R</sub>	49.91	
D	2.5 hr.	Tetragonal + Rhombohedral	(002) <sub>T</sub>	43.68	4.141	4.032	1.027	(200) <sub>R</sub>	44.29	89.98
			(200) <sub>T</sub>	44.93				(102) <sub>R</sub>	49.90	
E	5 hr.	Tetragonal + Rhombohedral	(002) <sub>T</sub>	43.64	4.145	4.039	1.026	(200) <sub>R</sub>	44.18	89.98
			(200) <sub>T</sub>	44.84				(102) <sub>R</sub>	49.82	



Table 6.1A

iii) LATTICE PARAMETERS OF  $\text{Pb}(\text{Zr}_{0.5}\text{Ti}_{0.5})\text{O}_3$  SPECIMENS SINTERED AT VARIOUS TEMPERATURE.

(Calcination at  $860^\circ\text{C}$ / 1 hr, Sintering time = 1 hr).

Sample	Sintering temperature	Phases	Tetragonal			Rhombohedral					
			hkl	2θ	$C_T$ (Å)	$a_T$ (Å)	$C_T/a_T$	hkl	2θ	$a_R$ (Å)	α
A	1100°C	Tetragonal + Rhombohedral	(002) T	43.72	4.137	4.019	1.030	(200) R	44.22	4.083	90.20
			(200) T	45.08				(102) R	49.92		
B	1260°C	Tetragonal + Rhombohedral	(002) T	43.68	4.141	4.026	1.029	(200) R	44.30	4.083	89.98
			(200) T	45.00				(102) R	49.84		
I	1350°C	Tetragonal + Rhombohedral	(002) T	43.72	4.137	4.023	1.028	(200) R	44.29	4.083	89.98
			(200) T	45.03				(102) R	49.90		

Table 6.1A

iv) LATTICE PARAMETERS OF  $\text{Pb}(\text{Zr}_{0.5}\text{Ti}_{0.5})\text{O}_3$  SPECIMENS SINTERED AT  
VARIOUS TIMES.

(Calcination at  $860^\circ\text{C}$ / 1 hr. Sintering temperature  $1260^\circ\text{C}$ ).

Sample	Sinter- ing time	Phases	hkl	$2\theta$	$C_T$ ( $\text{\AA}$ )	$a_T$ ( $\text{\AA}$ )	$C_T/a_T$	hkl	$2\theta$	$a_R$ ( $\text{\AA}$ )	$\alpha$
B	1 hr.	Tetra- gonal + Rhombo- hedral	(002) T (200) T	43.68 45.00	4.141	4.036	1.029	(200) R (102) R	44.30 49.84	4.083	89.98
F	4 hr.	Tetra- gonal + Rhombo- hedral	(002) T (200) T	43.68 45.12	4.141	4.015	1.031	(200) R (102) R	44.16 50.00	4.097	90.75
G	7 hr.	Tetra- gonal + Rhombo- hedral	(002) T (200) T	43.72 45.22	4.137	4.007	1.033	(200) R (102) R	44.38 49.92	4.083	89.98

Table 6.1B

- i) COMPOSITION FLUCTUATION OF  $\text{Pb}(\text{Zr}_{0.5}\text{Ti}_{0.5})\text{O}_3$  SPECIMENS  
CALCINED AT VARIOUS TEMPERATURES.

(Calcination for 1 hr, sintering at  $1260^\circ\text{C}/1 \text{ hr}$ )

Sample	A	B	C
Calcination Temperature	$760^\circ\text{C}$	$860^\circ\text{C}$	$960^\circ\text{C}$
Composition Fluctuation ( $\Delta x$ )	0.0836	0.0211	0.0192
Percentage Composition fluctuation	16.71	4.22	3.84

Table 6.1B

- ii) COMPOSITION FLUCTUATION OF  $\text{Pb}(\text{Zr}_{0.5}\text{Ti}_{0.5})\text{O}_3$  SPECIMENS  
CALCINED AT VARIOUS TIME.

(Calcination temperature at  $860^\circ\text{C}$ , Sintering at  $1260^\circ\text{C}/1 \text{ hr}$ )

Sample	B	B	E
Calcination Time	1 hr.	2.5 hr.	5 hr.
Composition Fluctuation ( $\Delta x$ )	0.0211	0.0180	0.0070
Percentage Composition Fluctuation	4.22	3.60	1.40

Table 6.1B

iii) COMPOSITION FLUCTUATION OF  $\text{Pb}(\text{Zr}_{0.5}\text{Ti}_{0.5})\text{O}_3$  SPECIMENS  
SINTERED AT VARIOUS TEMPERATURE.

(Calcined at  $860^\circ\text{C}$ / 1 hr and sintered for 1 hr.)

Sample	H	B	I
Sintering Temperature	$1100^\circ\text{C}$	$1260^\circ\text{C}$	$1350^\circ\text{C}$
Composition Fluctuation ( $\Delta x$ )	0.133	0.0211	0.106
Percentage Composition Fluctuation	26.6	4.22	21.2

Table 6.1B

iv) COMPOSITION FLUCTUATION OF  $\text{Pb}(\text{Zr}_{0.5}\text{Ti}_{0.5})\text{O}_3$   
SPECIMENS SINTERED AT VARIOUS TIME.

(Calcined at  $860^\circ\text{C}$ /1 hr, sintered at  $1260^\circ\text{C}$ )

Sample	B	F	G
Sintering Time	1 hr.	4 hr.	7 hr.
Composition Fluctuation ( $\Delta x$ )	0.0211	0.066	0.165
Percentage Composition Fluctuation	4.22	13.2	33

Table 6.2

GRAIN SIZE OF  $\text{Pb}(\text{Zr}_{0.5}\text{Ti}_{0.5})\text{O}_3$  SAMPLES PREPARED UNDER VARIOUS CALCINATION AND SINTERING CONDITIONS.

- i) Grain diameters of  $\text{Pb}(\text{Zr}_{0.5}\text{Ti}_{0.5})\text{O}_3$  Samples calcined at various temperatures. ( Calcination for 1 hr, sintering at  $1260^\circ\text{C}/1$  hr).

Sample	Calcination Temperature	Grain diameter ( $\mu\text{m}$ )
A	$760^\circ\text{C}$	2.81
B	$860^\circ\text{C}$	3.46
C	$960^\circ\text{C}$	3.58

- ii) Grain size of  $\text{Pb}(\text{Zr}_{0.5}\text{Ti}_{0.5})\text{O}_3$  samples calcined at various times (Calcination at  $860^\circ\text{C}$ , Sintering at  $1260^\circ\text{C}/1$  hr).

Sample	Calcination time	Grain diameter ( $\mu\text{m}$ )
B	1 hr.	3.46
D	2.5 hr.	3.67
E	5 hr.	3.77

iii) Grain size of  $\text{Pb}(\text{Zr}_{0.5}\text{Ti}_{0.5})\text{O}_3$  Samples sintered at various temperatures ( calcination at  $860^\circ\text{C}$ / 1 hr, sintering for 1 hr).

Sample	Sintering temperature	Grain diameter ( $\mu\text{m}$ )
A	$1100^\circ\text{C}$	3.36
B	$1260^\circ\text{C}$	3.46
I	$1350^\circ\text{C}$	3.82

iv) Grain size of  $\text{Pb}(\text{Zr}_{0.5}\text{Ti}_{0.5})\text{O}_3$  samples sintered at various times ( Calcination at  $860^\circ\text{C}$ / 1 hr, sintering at  $1260^\circ\text{C}$ ).

Sample	Sintering time	Grain diameter ( $\mu\text{m}$ )
B	1 hr.	3.46
F	4 hr.	3.88
G	7 hr.	6.22

Table 6.3

i) STRAIN COEFFICIENT OF  $\text{Pb}(\text{Zr}_{0.5}\text{Ti}_{0.5})\text{O}_3$  SPECIMENS CALCINED AT VARIOUS TEMPERATURE.

(Calcination time 1 hr, sintering temperature  $1260^\circ\text{C}$  sintering time 1 hr).

Sample	Calcination Temperature	Mean $d_{33}$	Standard deviation
A	$760^\circ\text{C}$	$114.70 \text{ CN}^{-1}$	$7.91 \text{ CN}^{-1}$
B	$860^\circ\text{C}$	$122.8 \text{ CN}^{-1}$	$4.61 \text{ CN}^{-1}$
C	$960^\circ\text{C}$	$145.8 \text{ CN}^{-1}$	$3.12 \text{ CN}^{-1}$

Table 6.3

ii) STRAIN COEFFICIENT OF  $\text{Pb}(\text{Zr}_{0.5}\text{Ti}_{0.5})\text{O}_3$  SPECIMENS CALCINED AT VARIOUS TIME.

(Calcination temperature  $860^\circ\text{C}$ , sintering temperature  $1260^\circ\text{C}$ , sintering time 1 hr.)

Sample	Calcination Time	Mean $d_{33}$	Standard deviation
B	1 hr.	$122.8 \text{ CN}^{-1}$	$4.61 \text{ CN}^{-1}$
D	$2\frac{1}{2}$ hr.	$143.9 \text{ CN}^{-1}$	$2.19 \text{ CN}^{-1}$
E	5 hr.	$144.0 \text{ CN}^{-1}$	$1.20 \text{ CN}^{-1}$

Table 6.3

iii) STRAIN COEFFICIENT OF  $\text{Pb}(\text{Zr}_{0.5}\text{Ti}_{0.5})\text{O}_3$  SPECIMENS  
SINTERED AT VARIOUS TEMPERATURES.

(Calcination temperature  $860^\circ\text{C}$ , sintering time 1 hr,  
calcination time 1 hr.)

Sample	Sintering Temperature	Mean $d_{33}$	Standard deviation
H	$1100^\circ\text{C}$	$115.2 \text{ CN}^{-1}$	$4.67 \text{ CN}^{-1}$
C	$1260^\circ\text{C}$	$122.8 \text{ CN}^{-1}$	$4.61 \text{ CN}^{-1}$
I	$1350^\circ\text{C}$	$131.9 \text{ CN}^{-1}$	$1.02 \text{ CN}^{-1}$

Table 6.3

iv) STRAIN COEFFICIENT OF  $\text{Pb}(\text{Zr}_{0.5}\text{Ti}_{0.5})\text{O}_3$  SPECIMENS SINTERED  
AT VARIOUS TIME.

(Calcination temperature  $860^\circ\text{C}$ ; calcination time 1 hr.,  
sintering temperature  $1260^\circ\text{C}$ )

Sample	Sintering Time	Mean $d_{33}$	Standard deviation
B	1 hr	$122.8 \text{ CN}^{-1}$	$4.61 \text{ CN}^{-1}$
F	4 hr	$143.7 \text{ CN}^{-1}$	$4.65 \text{ CN}^{-1}$
G	7 hr	$177.3 \text{ CN}^{-1}$	$8.48 \text{ CN}^{-1}$



Table 6.4

i) DENSITY AND POROSITY OF  $\text{Pb}(\text{Zr}_{0.5}\text{Ti}_{0.5})\text{O}_3$  SPECIMENS  
CALCINED AT VARIOUS TEMPERATURES.

(Calcination time 1 hr. sintering temperature  $1260^\circ\text{C}$   
sintering time 1 hr.).

Sample	Calcination Temperature	Density (gm/cc)	Porosity (%)
A	$760^\circ\text{C}$	7.90	1.86
B	$860^\circ\text{C}$	8.10	1.45
C	$960^\circ\text{C}$	8.13	1.38

Table 6.4

ii) DENSITY AND POROSITY OF  $\text{Pb}(\text{Zr}_{0.5}\text{Ti}_{0.5})\text{O}_3$  SPECIMENS  
CALCINED AT VARIOUS TIMES.

(Calcination temperature  $860^\circ\text{C}$  sintering time 1 hr  
sintering temperature  $1260^\circ\text{C}$ ).

Sample	Calcination Time	Density (gm/cc)	Porosity (%)
B	1 hr.	8.10	1.45
D	$2\frac{1}{2}$ hr	8.11	1.43
E	5 hr.	8.12	1.38

Table 6.4

iii) DENSITY AND POROSITY OF  $\text{Pb}(\text{Zr}_{0.5}\text{Ti}_{0.5})\text{O}_3$  SPECIMENS  
SINTERED AT VARIOUS TEMPERATURES.

(Calcination temperature  $860^\circ\text{C}$  , Calcination time 1 hr,  
sintering time 1 hr).

Sample	Sintering Temperature	Density (gm/cc)	Porosity (%)
H	$1100^\circ\text{C}$	8.10	1.48
B	$1260^\circ\text{C}$	8.10	1.45
I	$1350^\circ\text{C}$	8.03	1.48

Table 6.4

iv) DENSITY AND POROSITY OF  $\text{Pb}(\text{Zr}_{0.5}\text{Ti}_{0.5})\text{O}_3$  SPECIMENS  
SINTERED AT VARIOUS TIMES.

( Calcination temperature  $860^\circ\text{C}$ , calcination time 1 hr.  
sintering temperature  $1260^\circ\text{C}$ ).

Sample	Sintering Time	Density (gm/cc)	Porosity (%)
B	1 hr .	8.10	1.45
F	4 hr.	8.11	1.41
G	7 hr.	7.91	1.56

Table 6.5

i) VICKERS HARDNESS DATA OF  $\text{Pb}(\text{Zr}_{0.5}\text{Ti}_{0.5})\text{O}_3$  SPECIMENS CALCINED AT VARIOUS TEMPERATURES.

(Calcination time 1 hr., sintering temperature  $1260^\circ\text{C}$ ,  
Sintering time 1 hr.).

Sample	Calcination Temperature	$\bar{H}_V$ ( $\text{kg}/\text{mm}^2$ ) (mean Vickers hardness)
A	$760^\circ\text{C}$	5.7
B	$860^\circ\text{C}$	15.13
C	$960^\circ\text{C}$	114.29

Table 6.5

ii) VICKERS HARDNESS DATA OF  $\text{Pb}(\text{Zr}_{0.5}\text{Ti}_{0.5})\text{O}_3$  SPECIMENS CALCINED FOR VARIOUS TIMES.

(Calcination temperature  $860^\circ\text{C}$ , sintering time 1 hr,  
sintering temperature  $1260^\circ\text{C}$ )

Sample	Calcination Temperature	$\bar{H}_V$ ( $\text{kg}/\text{mm}^2$ ) (mean Vickers hardness)
B	1 hr	15.13
D	$2\frac{1}{2}$ hr	17.57
E	5 hr	27.53

Table 6.5

iii) VICKERS HARDNESS DATA OF  $\text{Pb}(\text{Zr}_{0.5}\text{Ti}_{0.5})\text{O}_3$  SPECIMENS  
SINTERED AT VARIOUS TEMPERATURES.

(Calcination temperature  $860^\circ\text{C}$ , calcination time 1 hr,  
sintering time 1 hr).

Sample	Sintering Temperature	$\bar{H}_V$ ( $\text{kg}/\text{mm}^2$ ) (mean Vickers hardness)
H	$1100^\circ\text{C}$	7.40
B	$1260^\circ\text{C}$	15.13
I	$1350^\circ\text{C}$	45.05

Table 6.5

iv) VICKERS HARDNESS DATA OF  $\text{Pb}(\text{Zr}_{0.5}\text{Ti}_{0.5})\text{O}_3$  SPECIMENS  
SINTERED AT VARIOUS TIMES.

(Calcination temperature  $860^\circ\text{C}$ , calcination time 1 hr.  
sintering temperature  $1260^\circ\text{C}$ ).

Sample	Sintering Time	$\bar{H}_V$ ( $\text{kg}/\text{mm}^2$ ) (mean Vickers hardness)
B	1 hr.	15.13
F	4 hr.	23.78
G	7 hr.	31.03

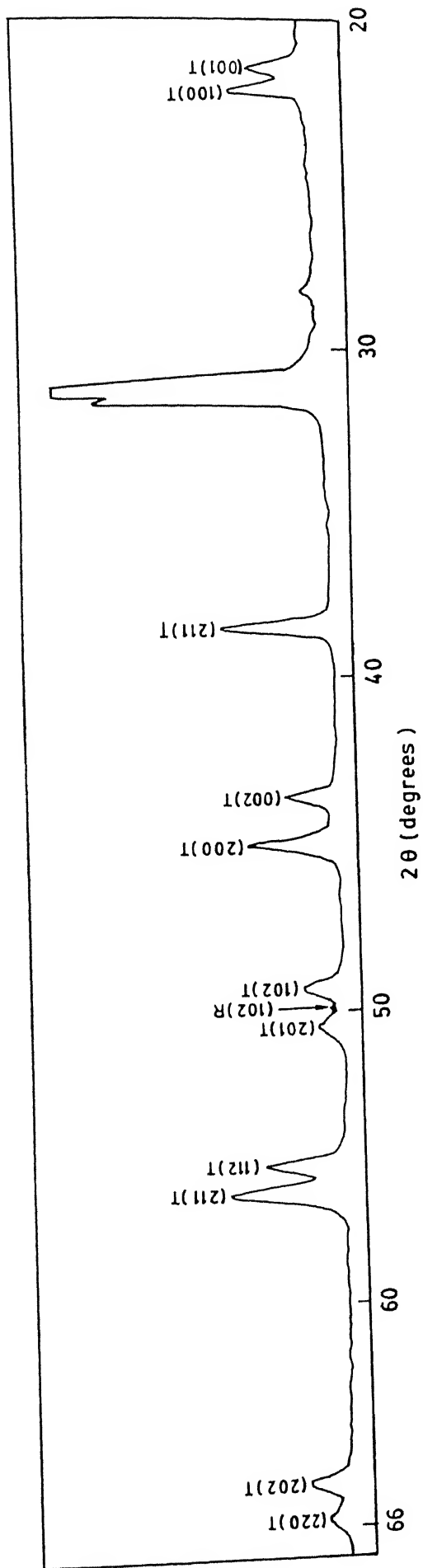


Fig. 6.1 XRD plot of  $\text{Pb}(\text{Zr}_{0.5}\text{Ti}_{0.5})\text{O}_3$  from  $2\theta = 20^\circ$  to  $2\theta = 70^\circ$ .

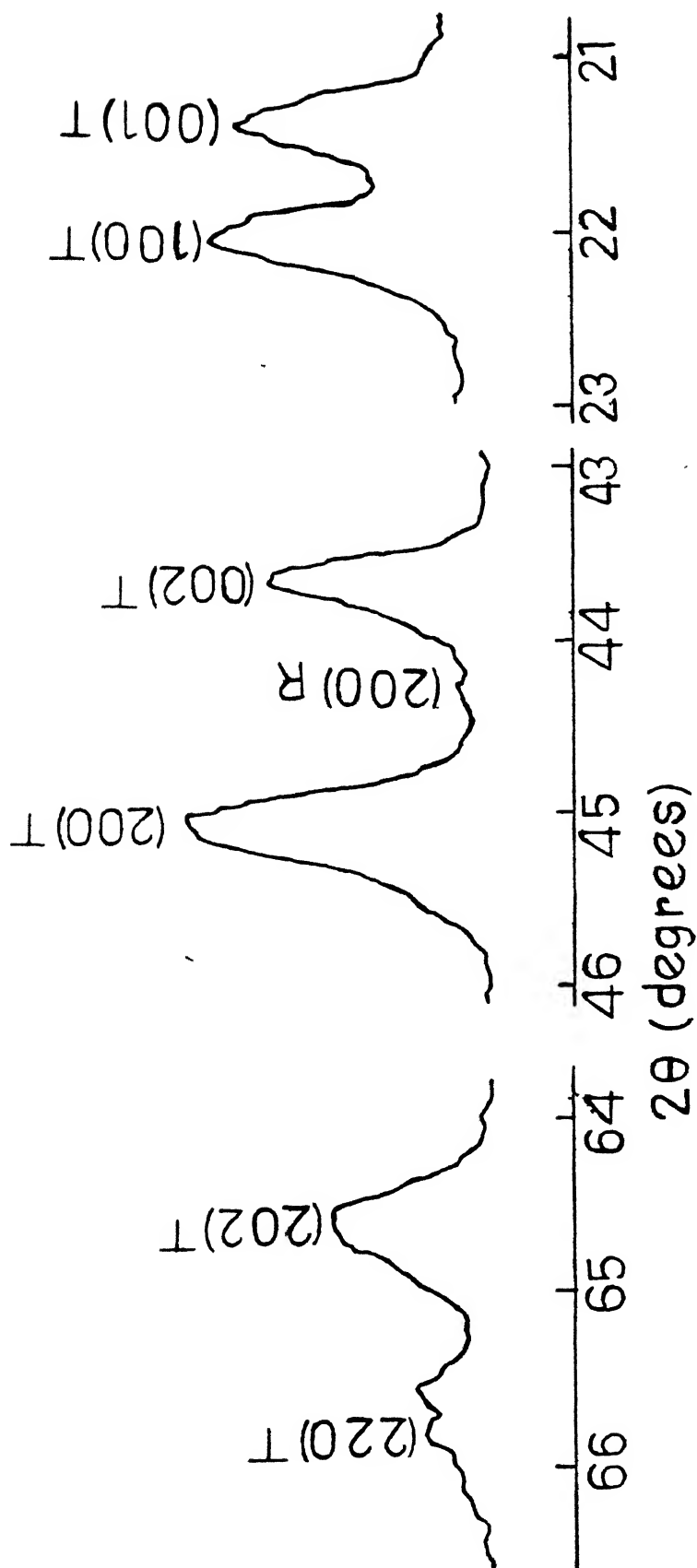


Fig. 6.2 : XRD Plot of  $\text{Pb}(\text{Zr}_{0.5}\text{Ti}_{0.5})\text{O}_3$  at  $0.6^\circ/\text{min. scan}$



Fig. 6.3 Scanning electron micrographs of PZT sample calcined at  $760^{\circ}\text{C}/1$  hr. and sintered at  $1260^{\circ}\text{C}/$



Fig. 6.4 Scanning electron micrograph of PZT sample calcined at  $860^{\circ}\text{C}/1$  hr. and sintered at  $1260^{\circ}\text{C}/1\text{hr.}$

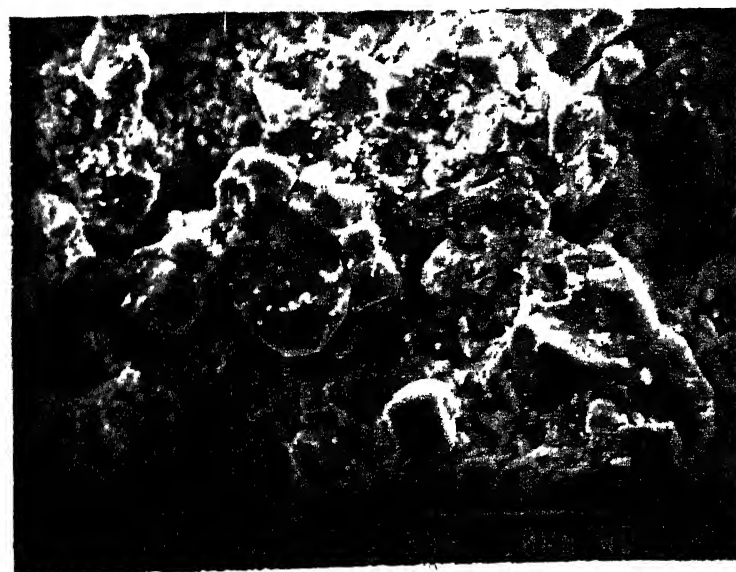
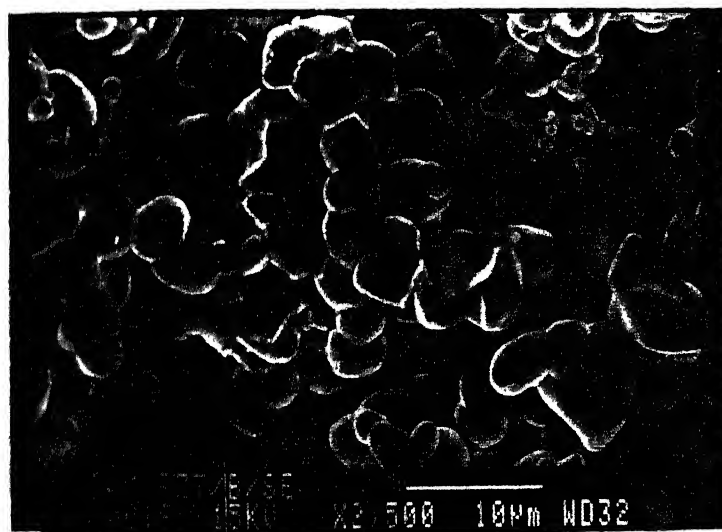
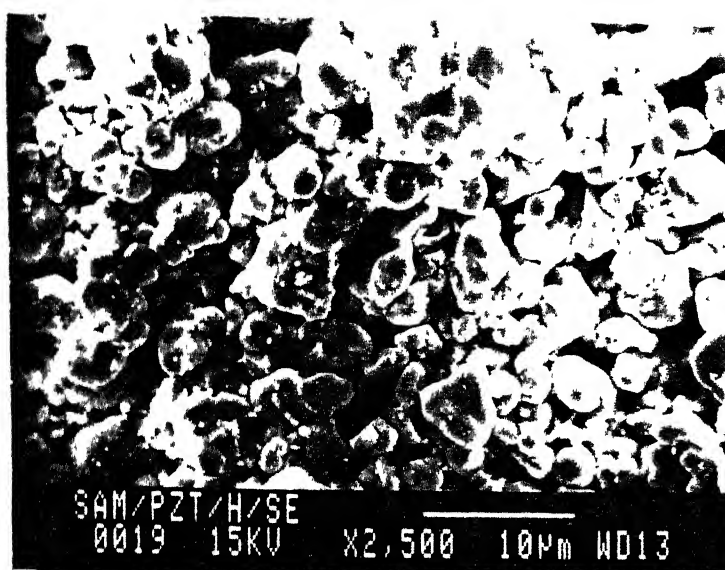


Fig. 6.5

Scanning electron micrograph of PZT sample calcined at  $260^{\circ}/1\text{hr}$  and sintered for 1 hr. Sintering temperature a)  $1100^{\circ}\text{C}$  b)  $1260^{\circ}\text{C}$  c)  $1350^{\circ}$ .



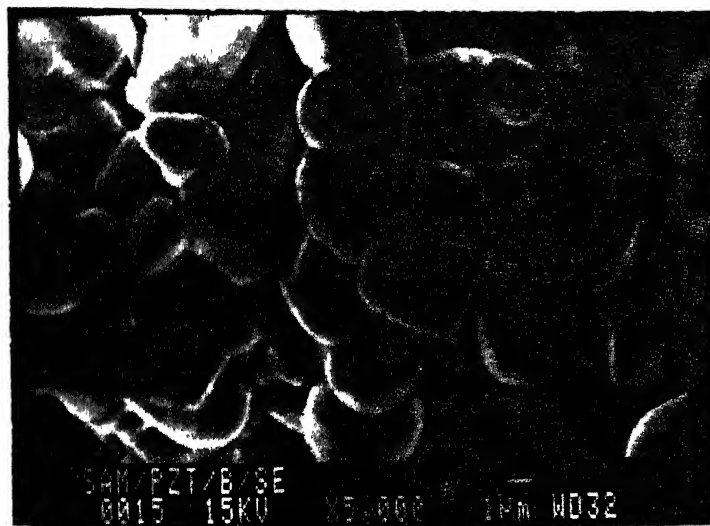


Fig. 6.6

Scanning electron micrographs of PZT samples calcined at  $860^{\circ}\text{C}$ / 1 hr and sintered at  $1260^{\circ}\text{C}$  for a) 1 hr b) 4 hr

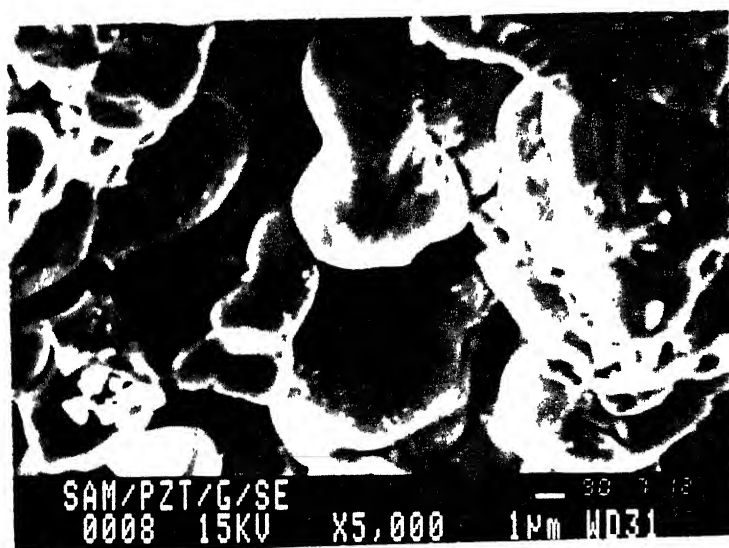
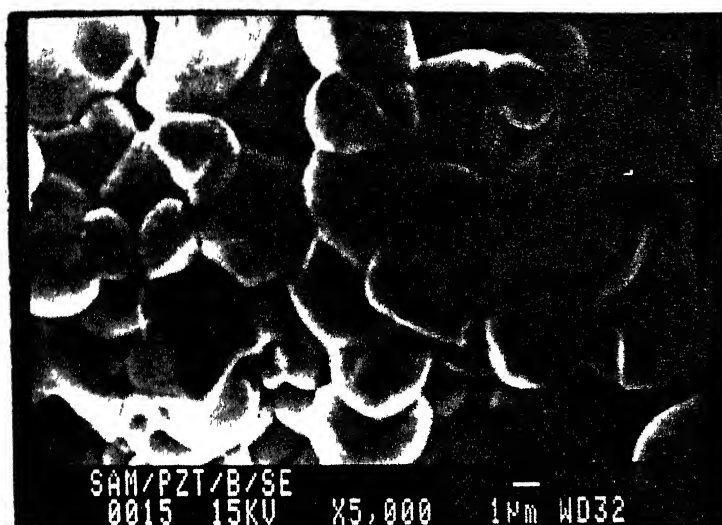


Fig. 6.7 Scanning electron micrograph of PZT samples calcined at  $860^{\circ}\text{C}/1$  hr and sintered at  $1260^{\circ}\text{C}$  for a) 1 hr b) 7 hr.

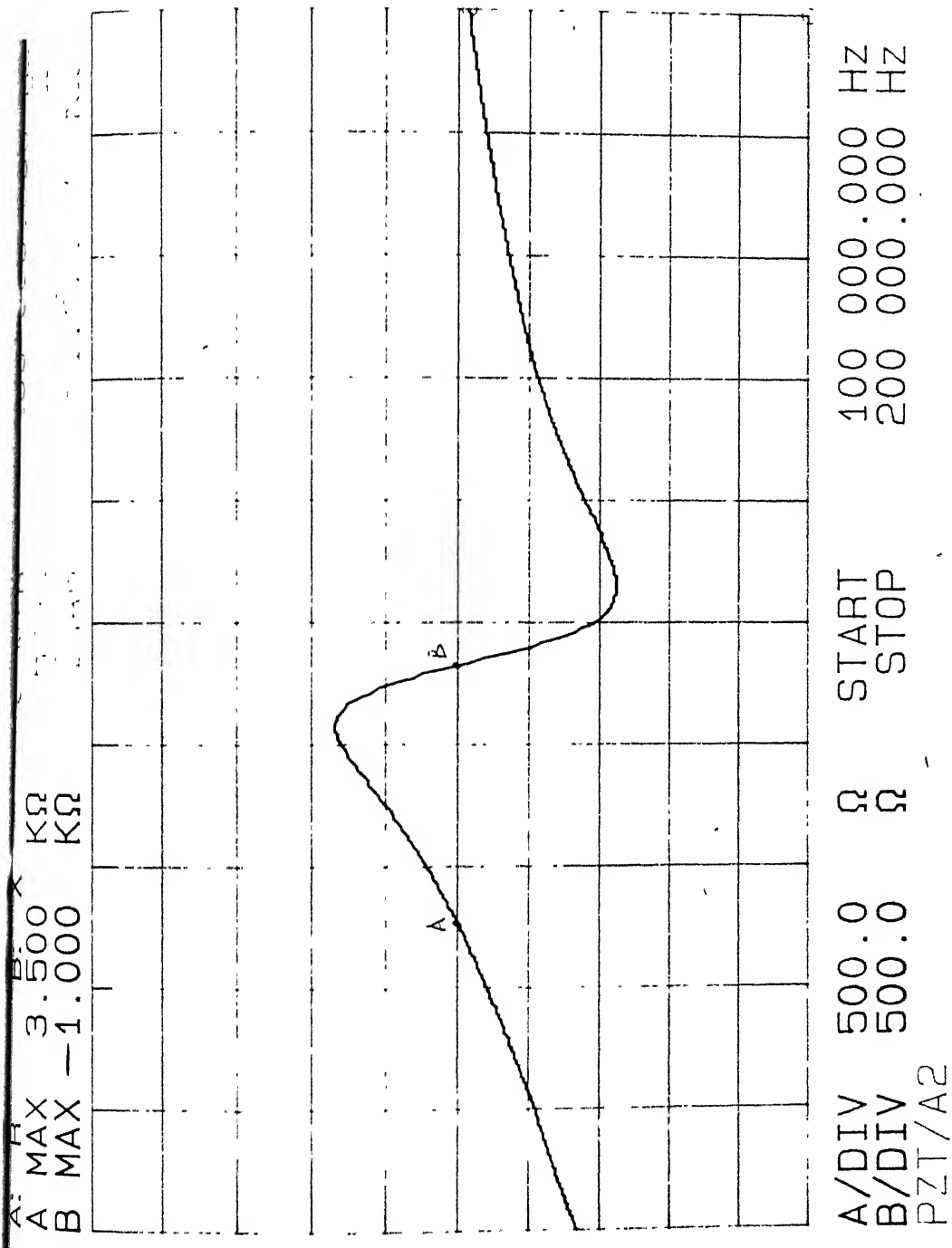


Fig. 6.8 Plot from Impedance analyser showing reactance as a function of frequency.

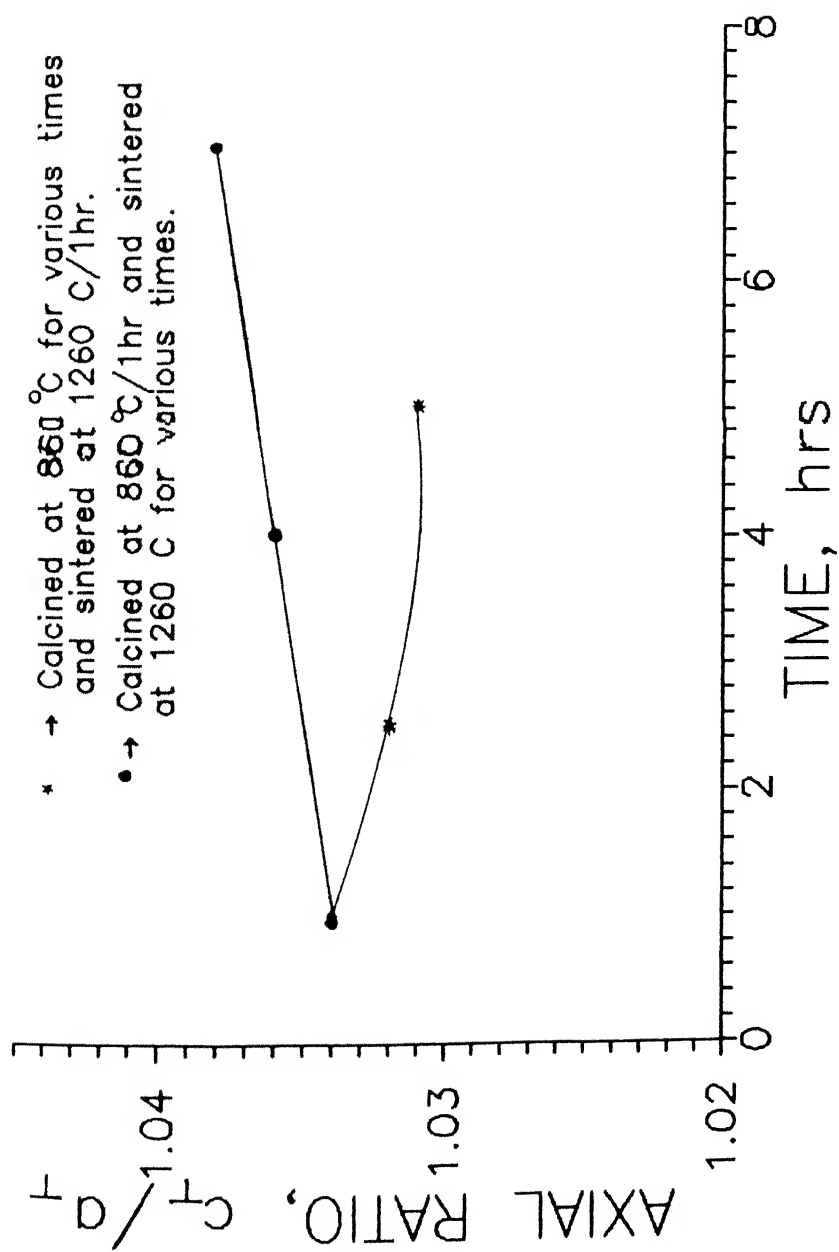


Fig. 6.9 Effect of calcination and sintering times on the  $C_T/a_T$  axial ratio.

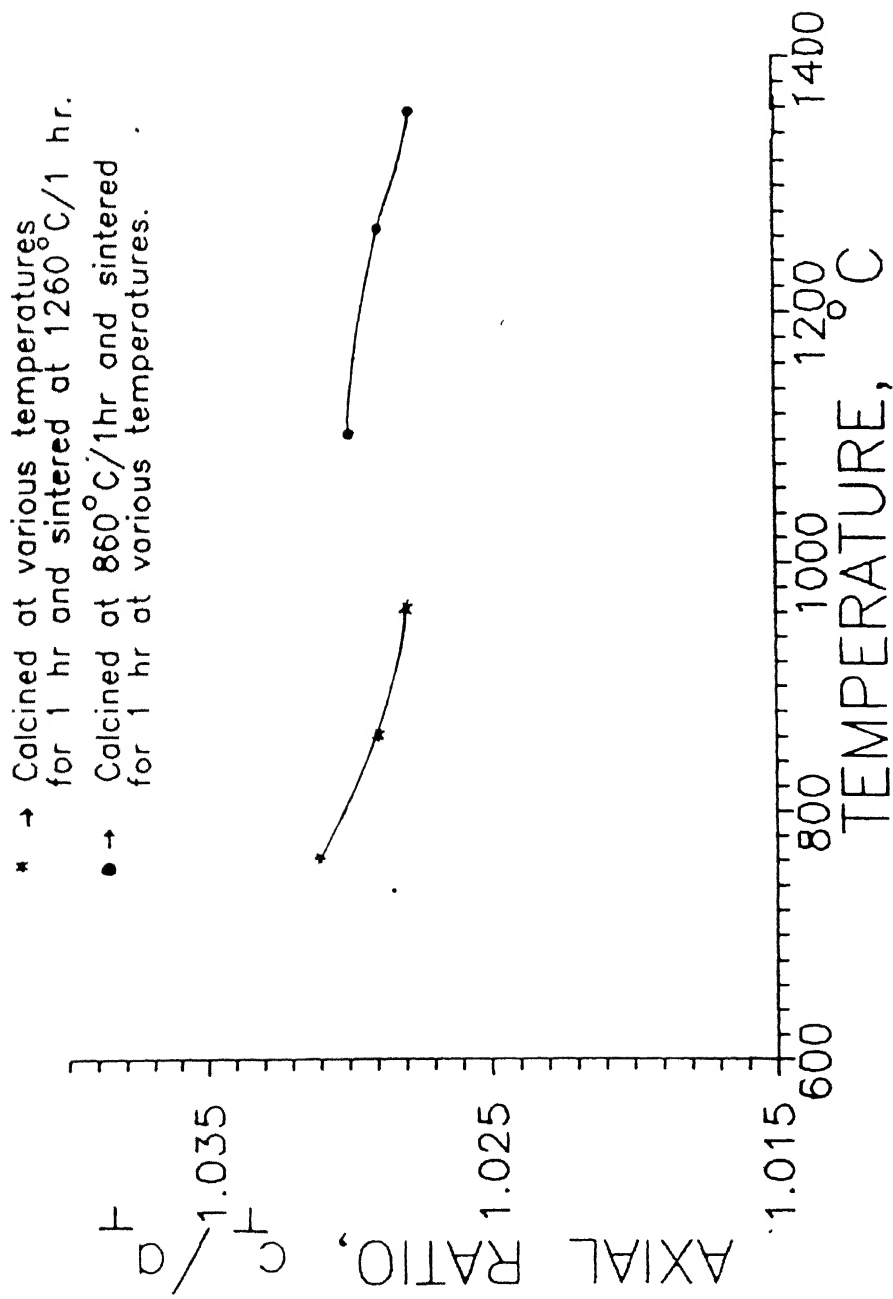


Fig. 6.10 Effect of calcination and sintering temperatures on the  $C_T/a_T$  axial ratio.

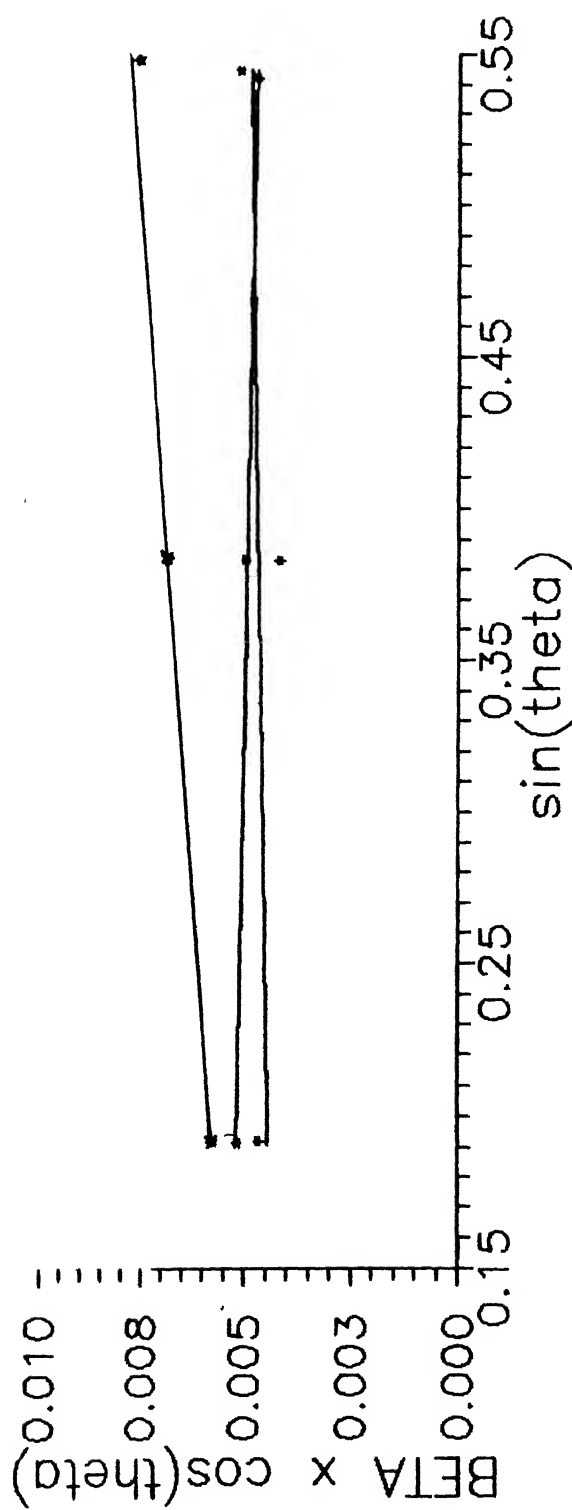


Fig. 6.11 Plot of  $\beta \cos \theta$  vs  $\sin \theta$  for PZT samples calcined at various temperatures for 1 hr. and sintered at 1260 C/ 1 hr.

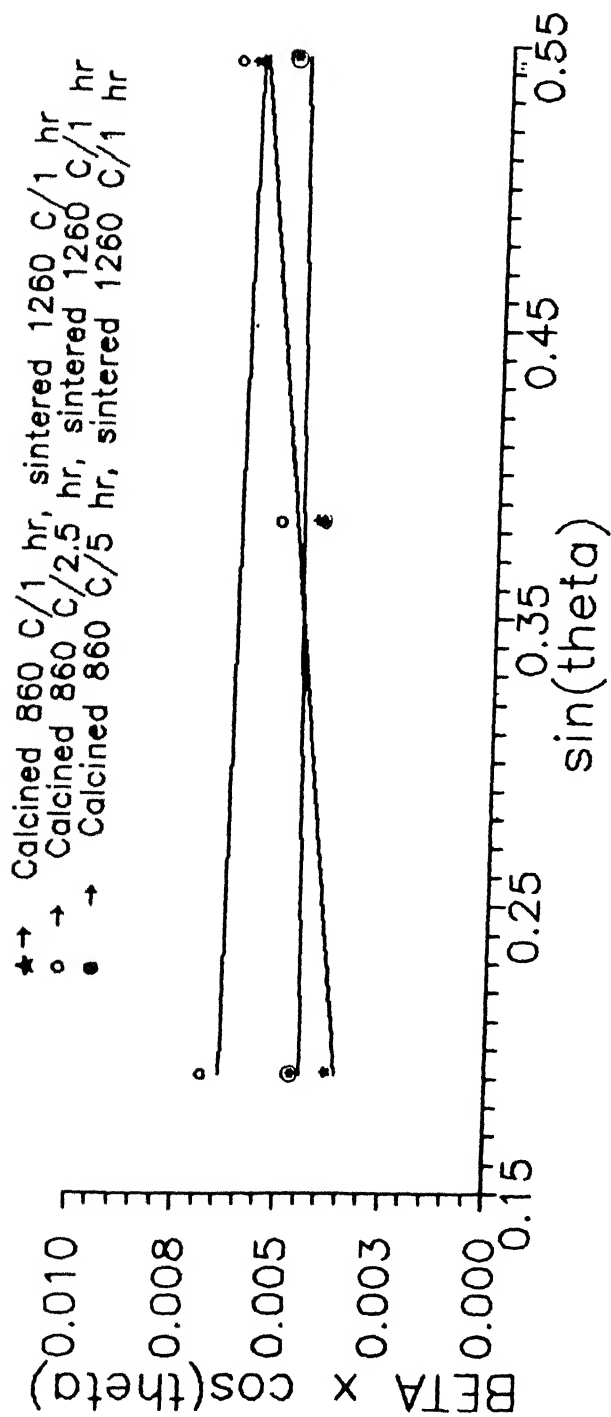


Fig. 6.12 Plot of  $\beta \cos \theta$  vs  $\sin \theta$  for PZT samples calcined for various times at 860°C and sintered at 1260°C/ 1 hr.

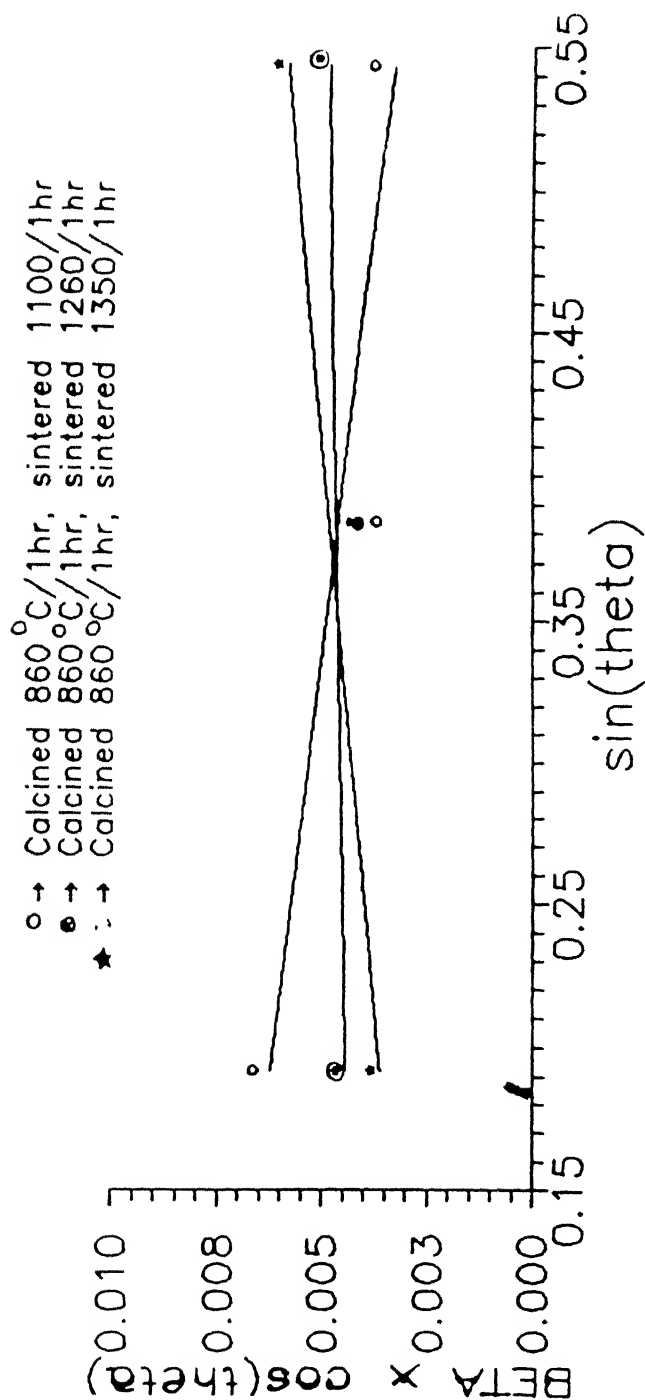


Fig. 6.13 Plot of  $\beta \cos \theta$  vs  $\sin \theta$  for Ti-1 samples calcined at 860°C/1 hr and sintered at various temperatures for 1 hr.



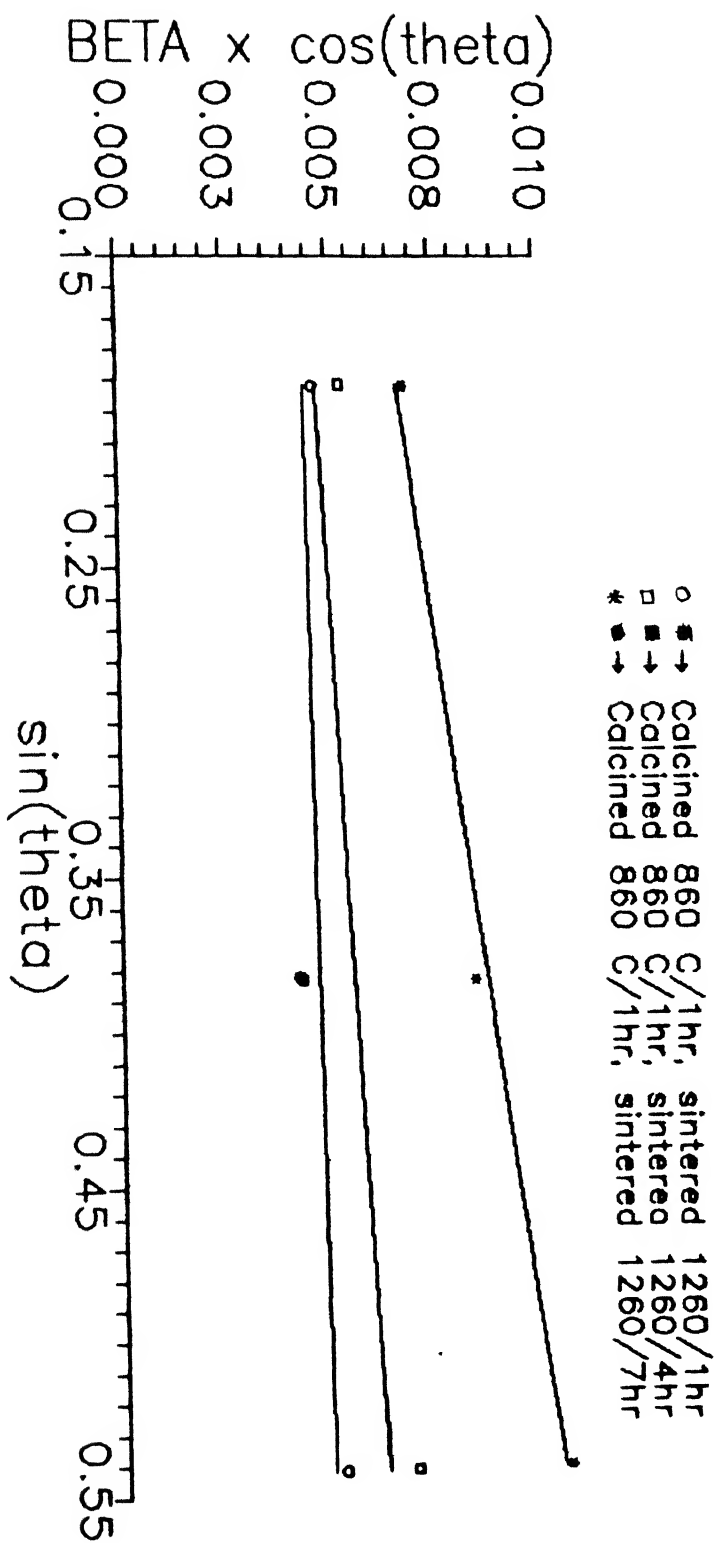


Fig. 6.14 Plot of  $\beta \cos \theta$  vs  $\sin \theta$  for LNT samples calcined at  $860^\circ\text{C}/1\text{ hr}$  and sintered at

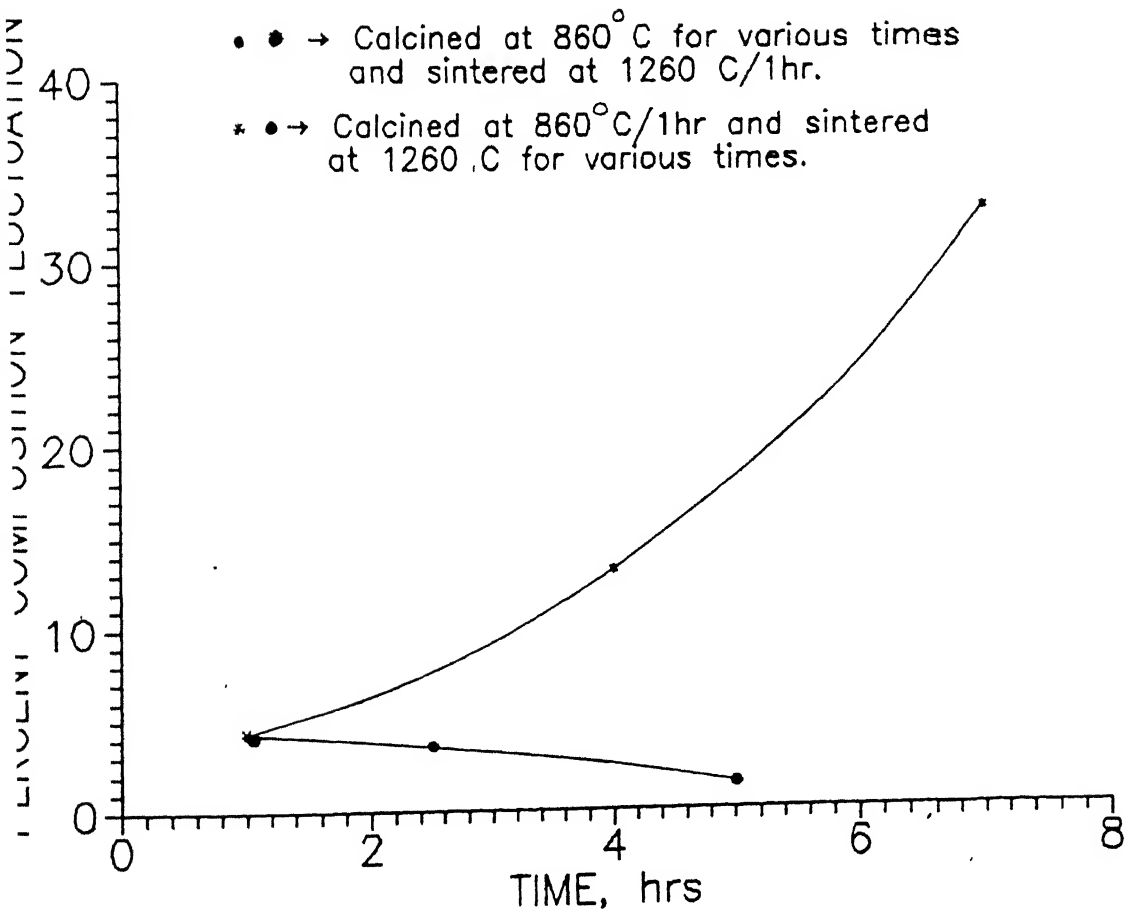


Fig. 6.15 Effect of calcination and sintering times on the composition fluctuation of  $\text{Pb}(\text{Zr}_{0.5}\text{Ti}_{0.5})\text{O}_3$ .

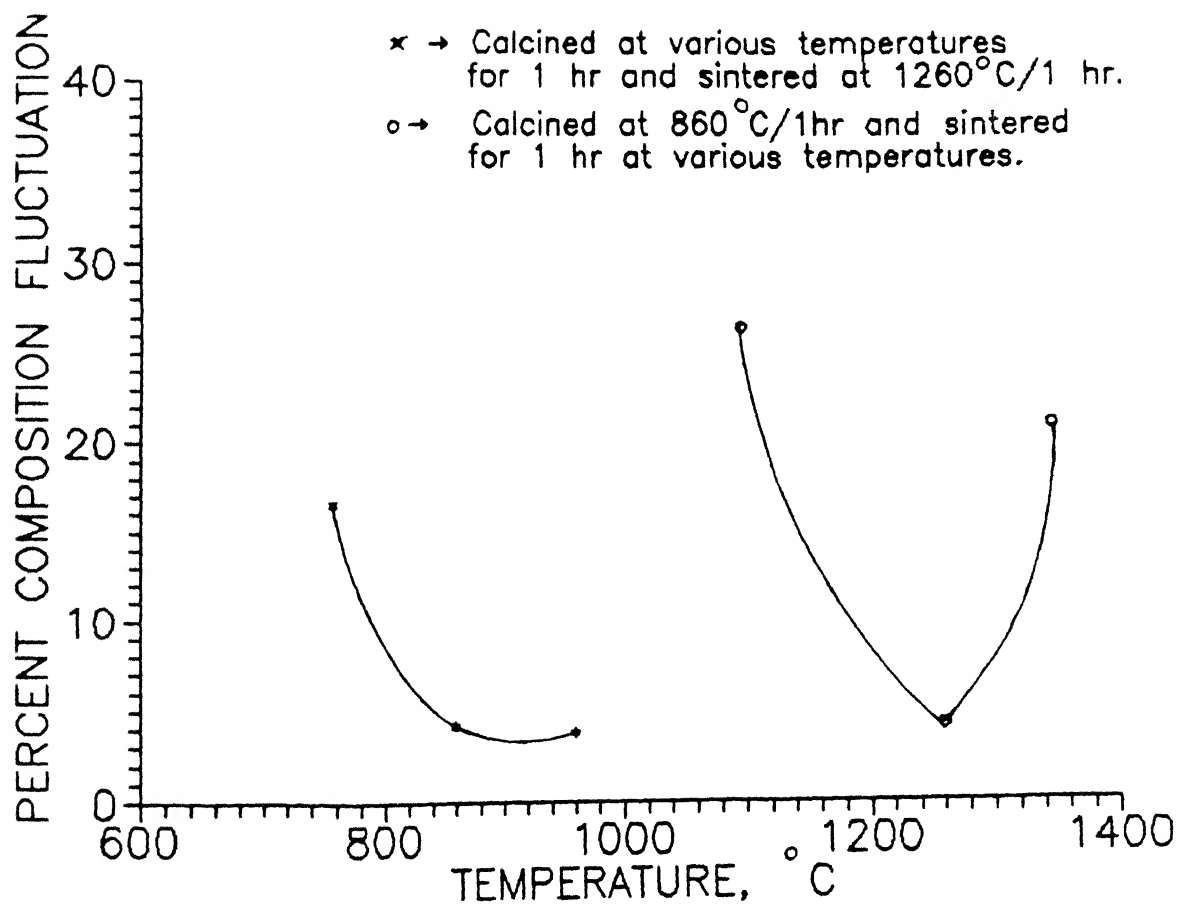


Fig. 6.16 Effect of calcination and sintering temperatures on the composition fluctuation of  $\text{Pb}(\text{Zr}_{0.5}\text{Ti}_{0.5})\text{O}$

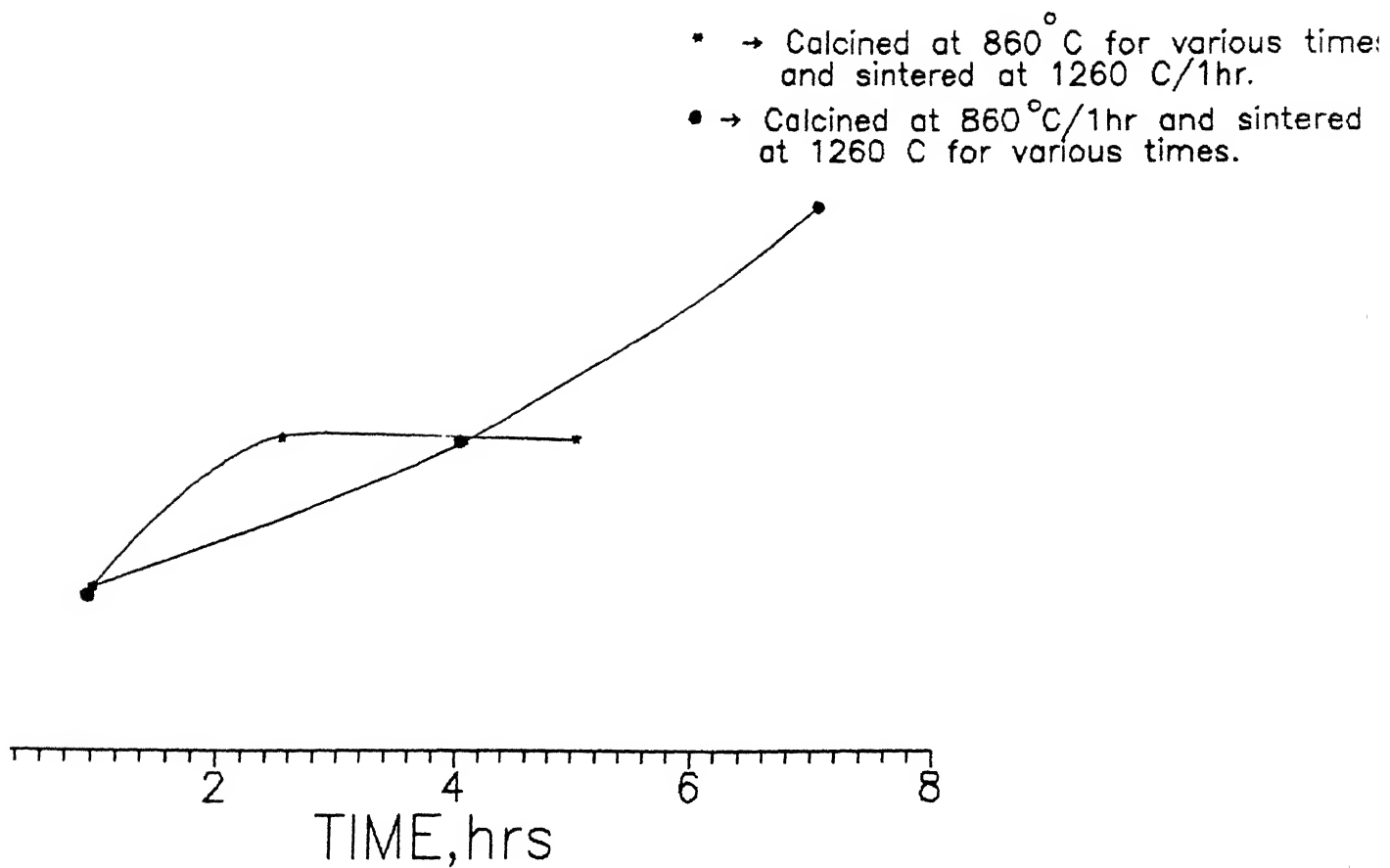


Fig. 6.17 Effect of calcination and sintering times  
 on the piezoelectric strain coefficient  
 of  $\text{Pb}(\text{Zr}_{0.5}\text{Ti}_{0.5})\text{O}_3$ .

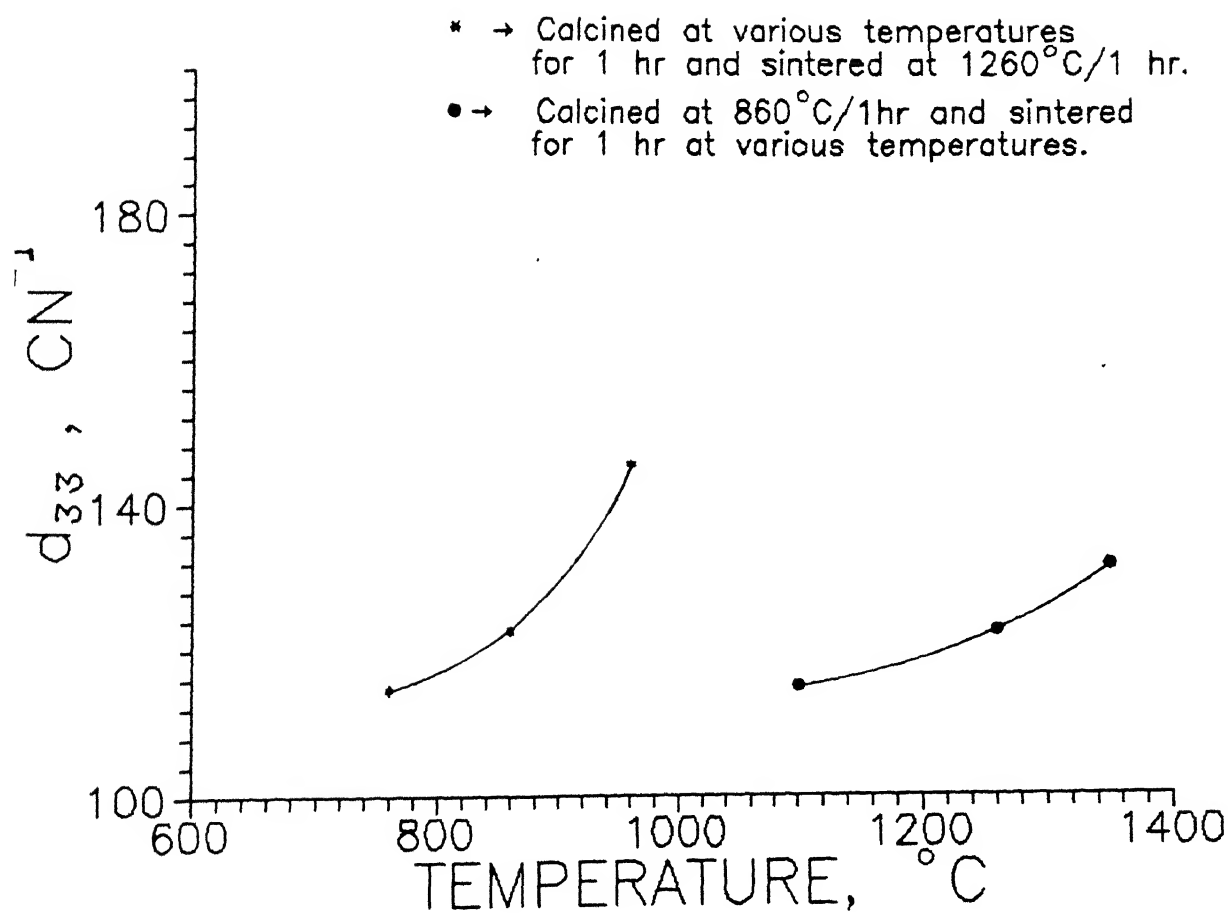


Fig. 6.18 Effect of calcination and sintering temperatures on the piezoelectric strain coefficient of  $\text{Pb}(\text{Zr}_{0.5}\text{Ti}_{0.5})\text{O}_3$ .

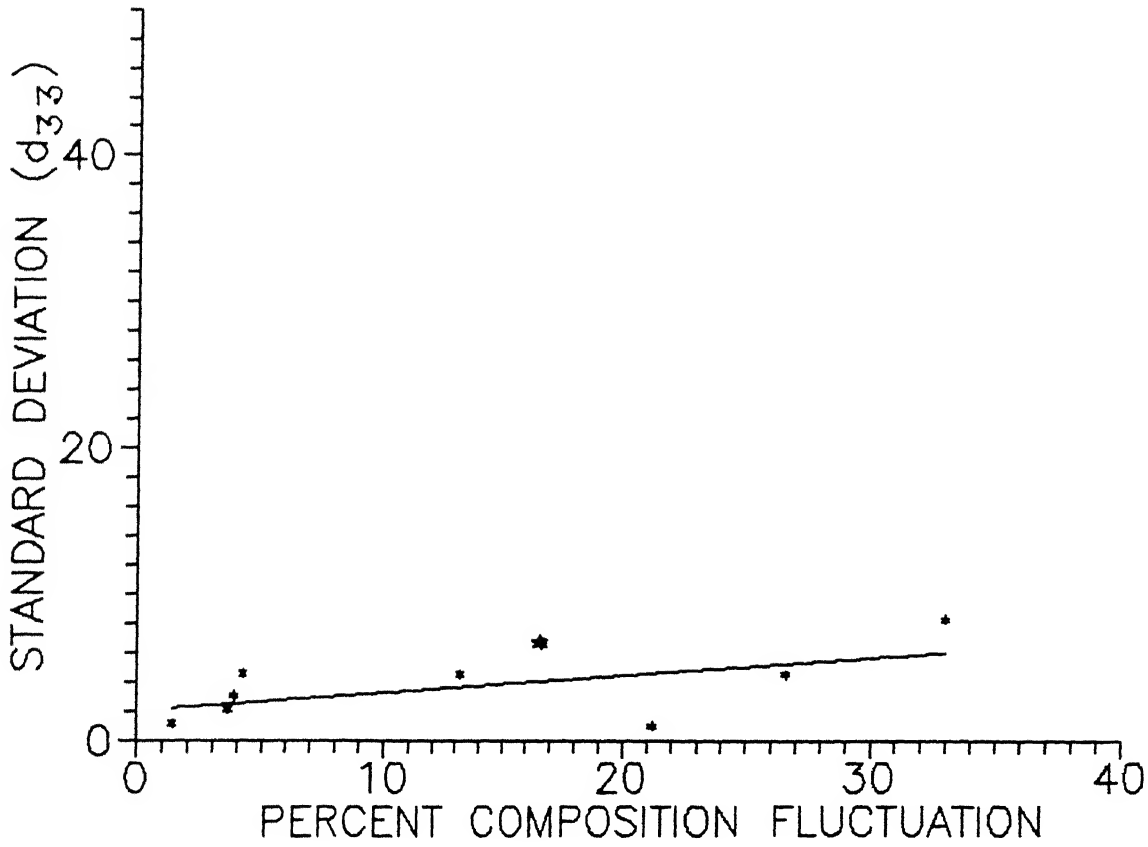


Fig. 6.19 Variation of standard deviation of piezo - electric strain coefficient,  $d_{33}$  as a function of composition fluctuation.

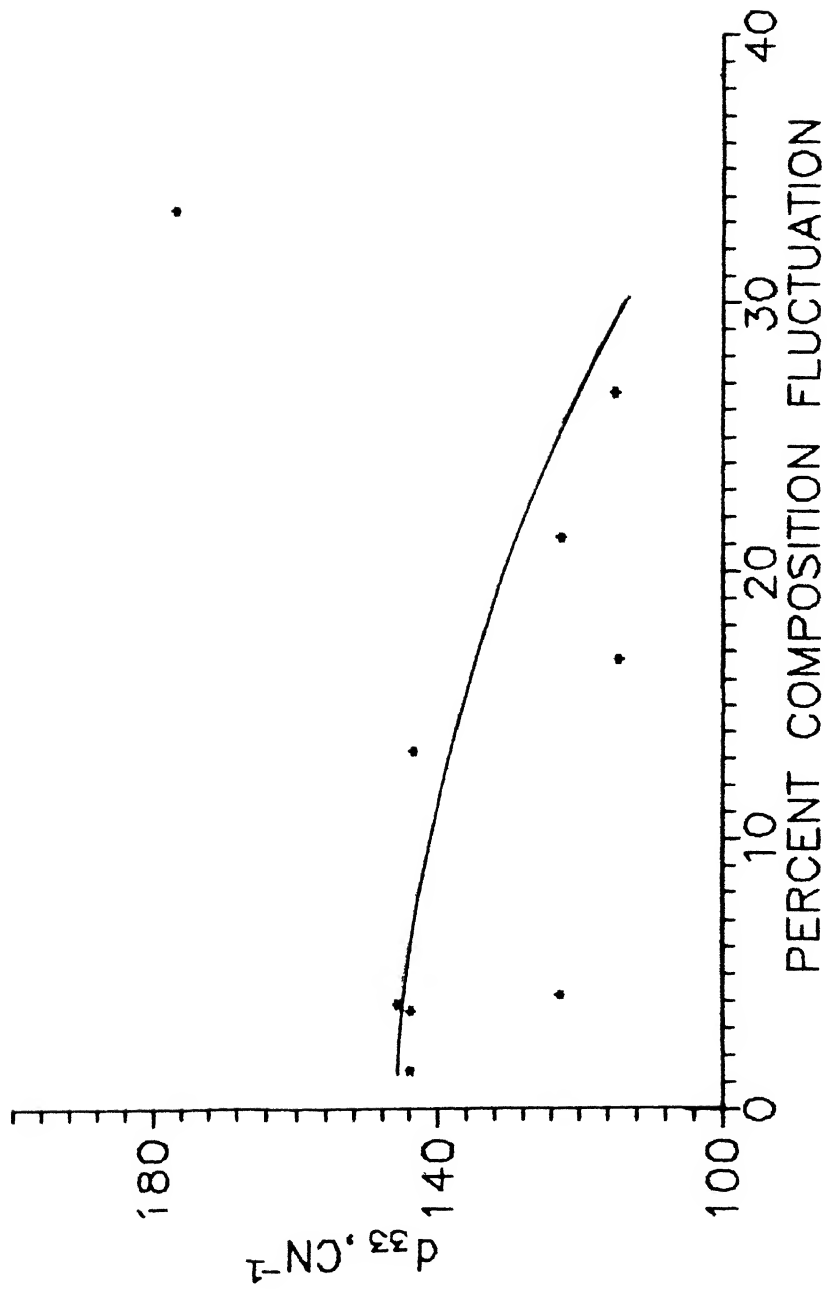


Fig. 6.20 Variation of piezoelectric strain coefficient,  $d_{33}$  as a function of composition fluctuation.

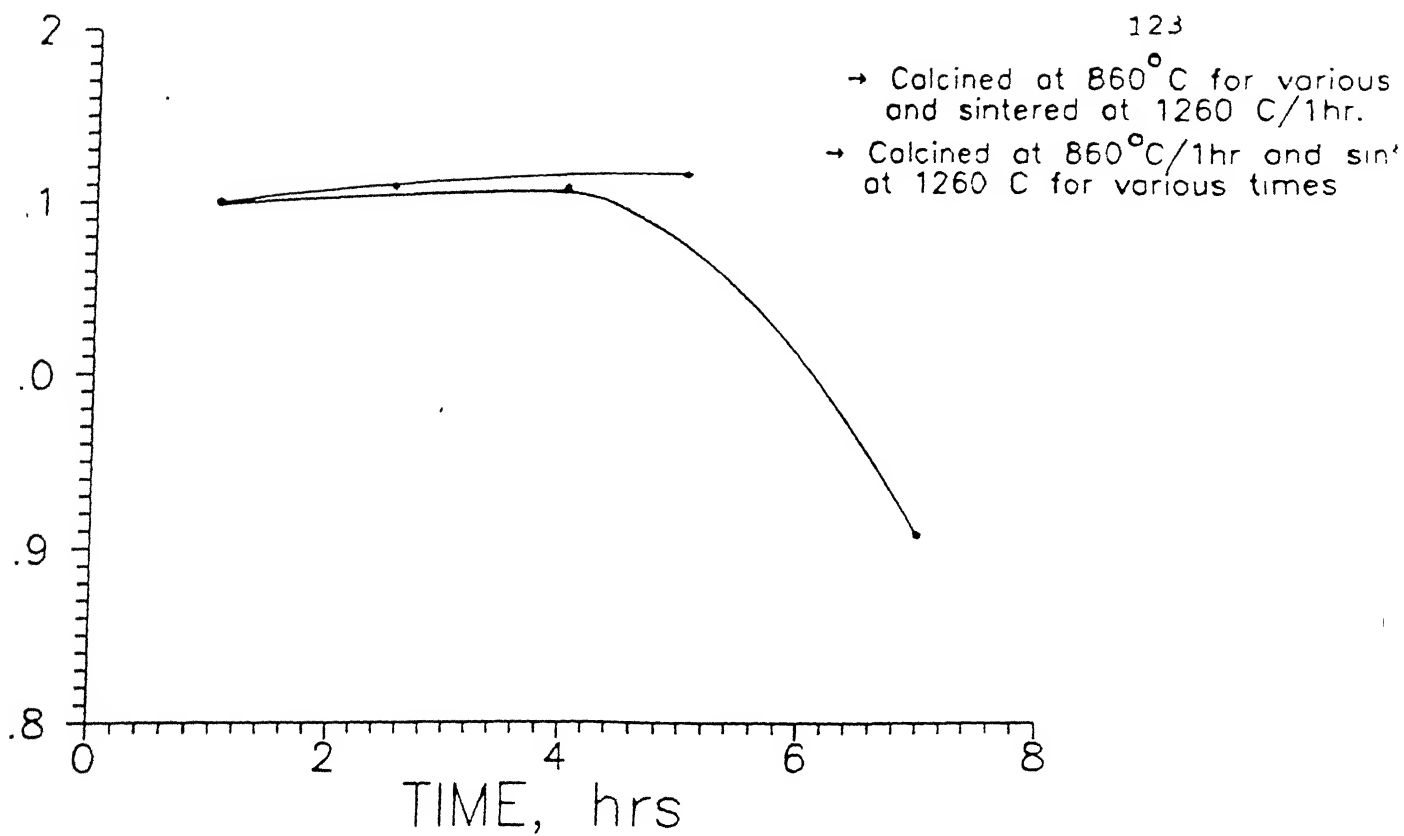


Fig. 6.21 Effect of calcination and sintering times on the density of  $\text{Pb}(\text{Zr}_{0.5}\text{Ti}_{0.5})\text{C}_3$ .



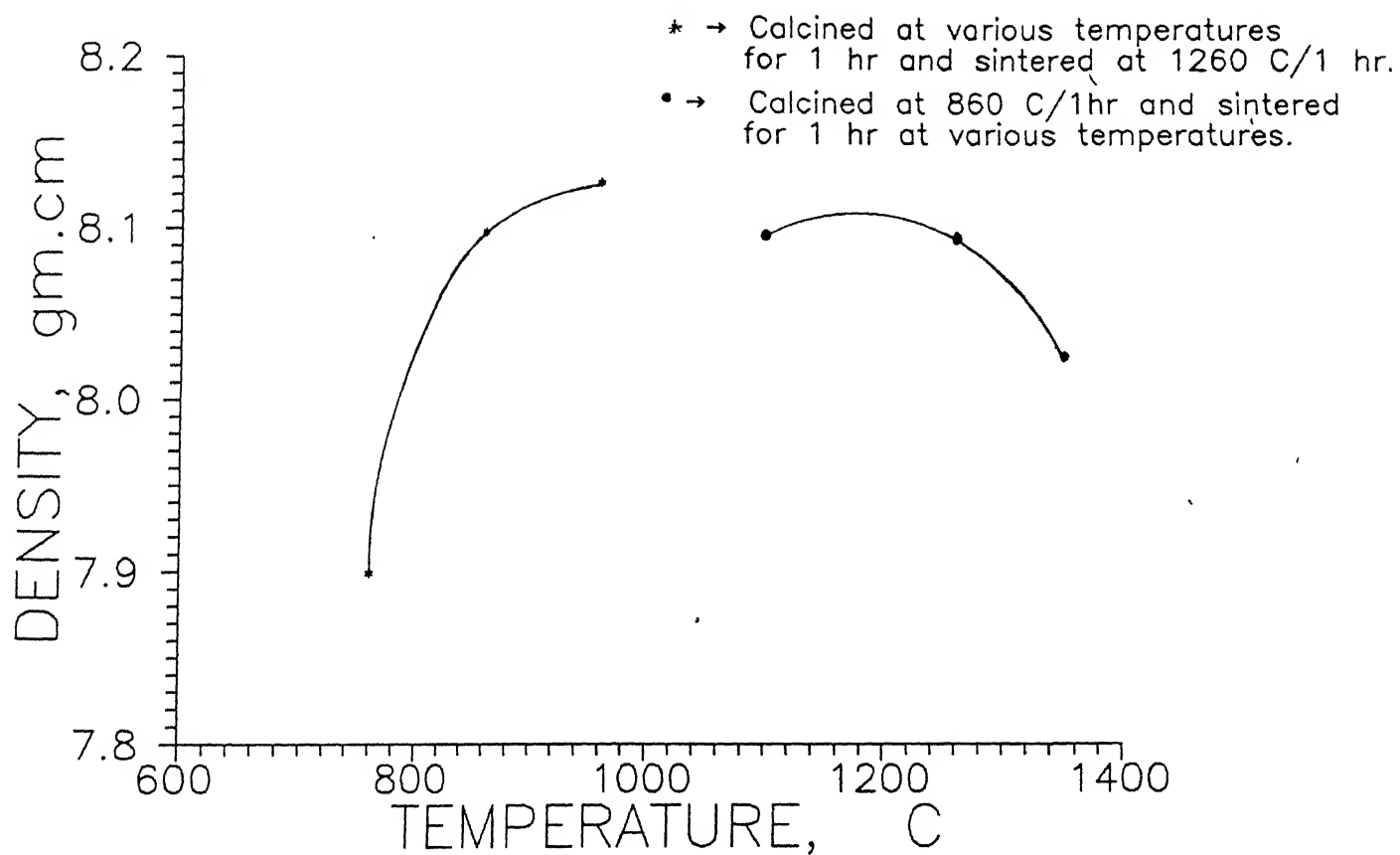


Fig. 6.22 Effect of calcination and sintering temperature on the density of  $\text{Pb}(\text{Zr}_{0.5}\text{Ti}_{0.5})\text{O}_3$ .

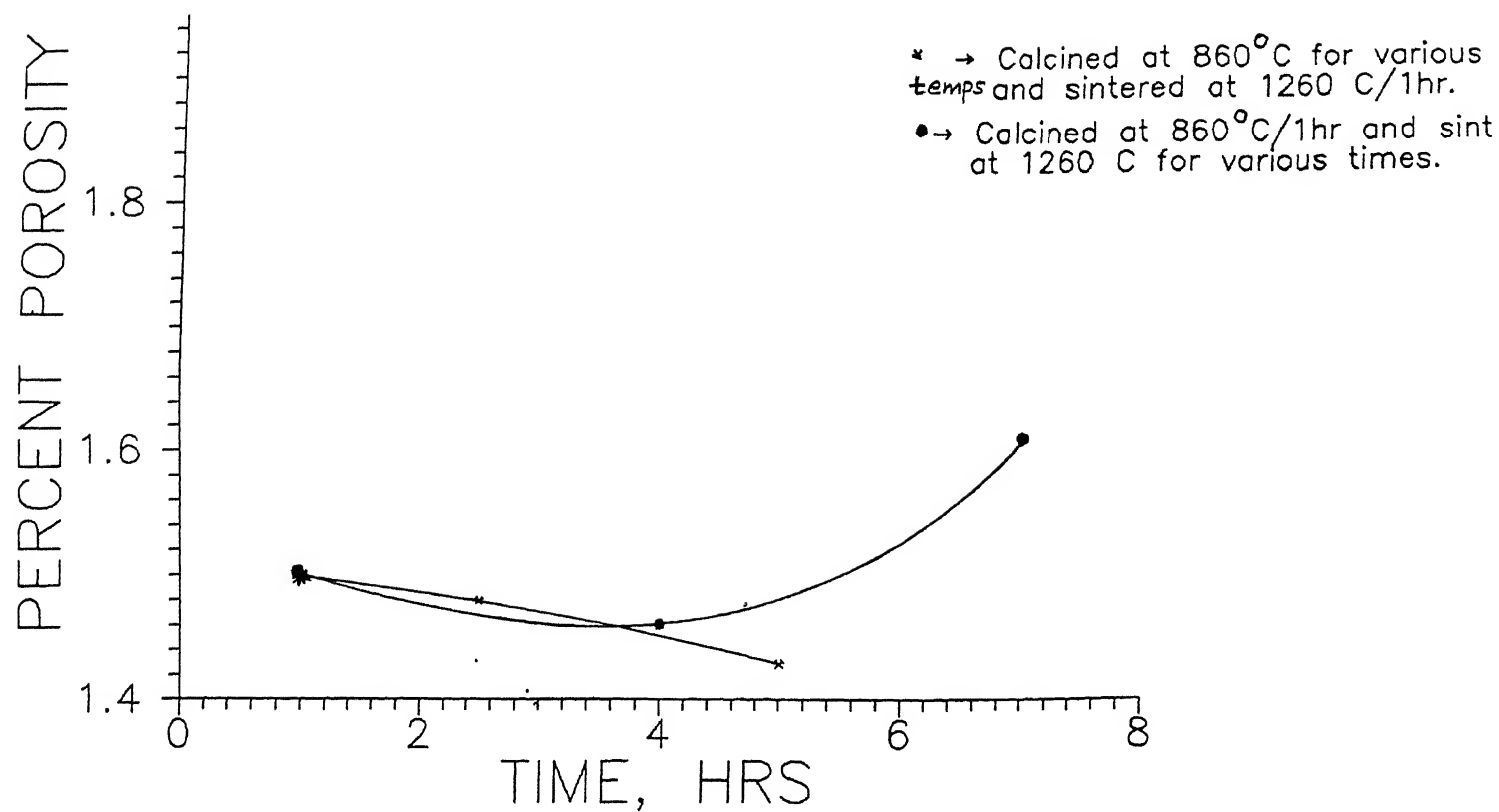


Fig. 6.23 Effect of calcination and sintering times on the porosity of  $\text{Pb}(\text{Zr}_{0.5}\text{Ti}_{0.5})\text{O}_3$ .

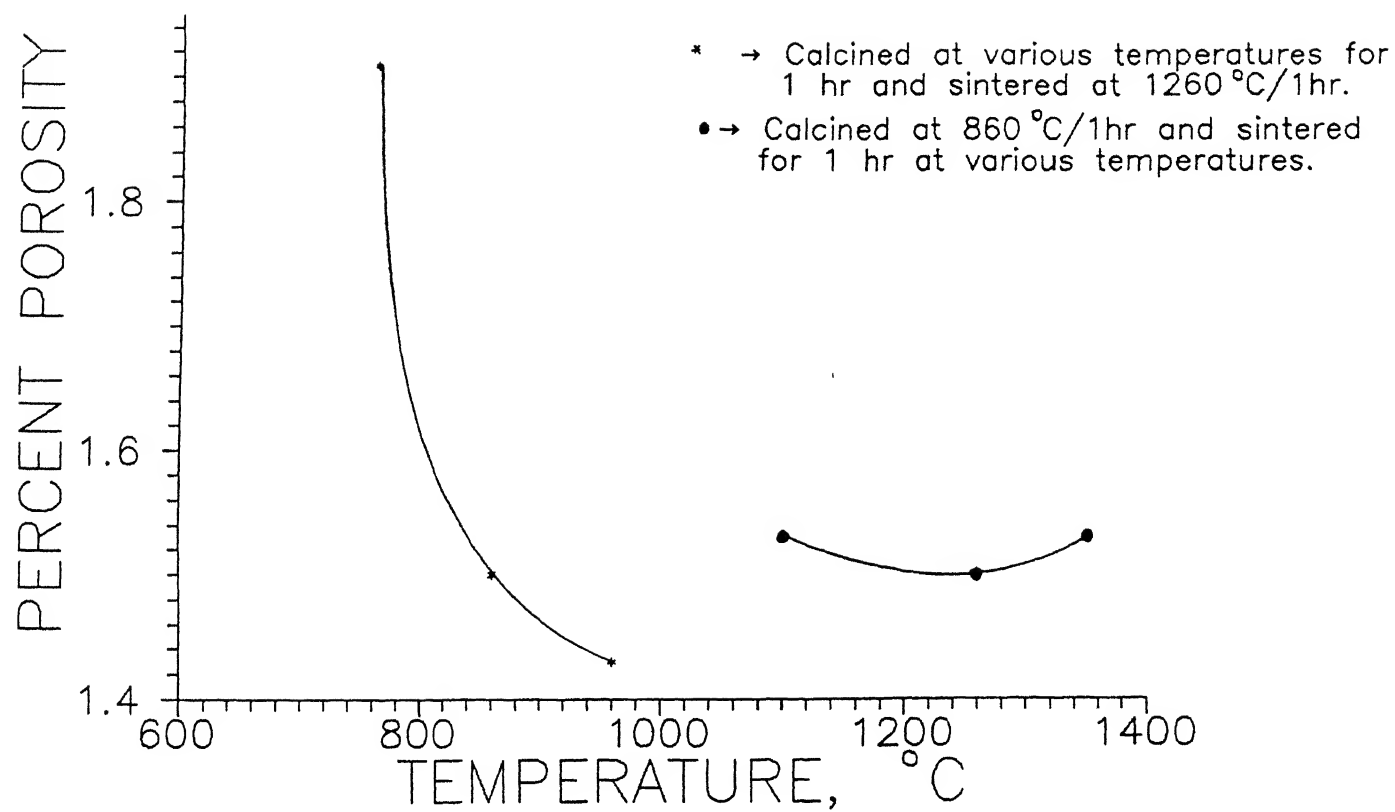


Fig. 6.24 Effect of calcination and sintering temperatures on the porosity of  $\text{Pb}(\text{Zr}_{0.5}\text{Ti}_{0.5})\text{O}_3$ .

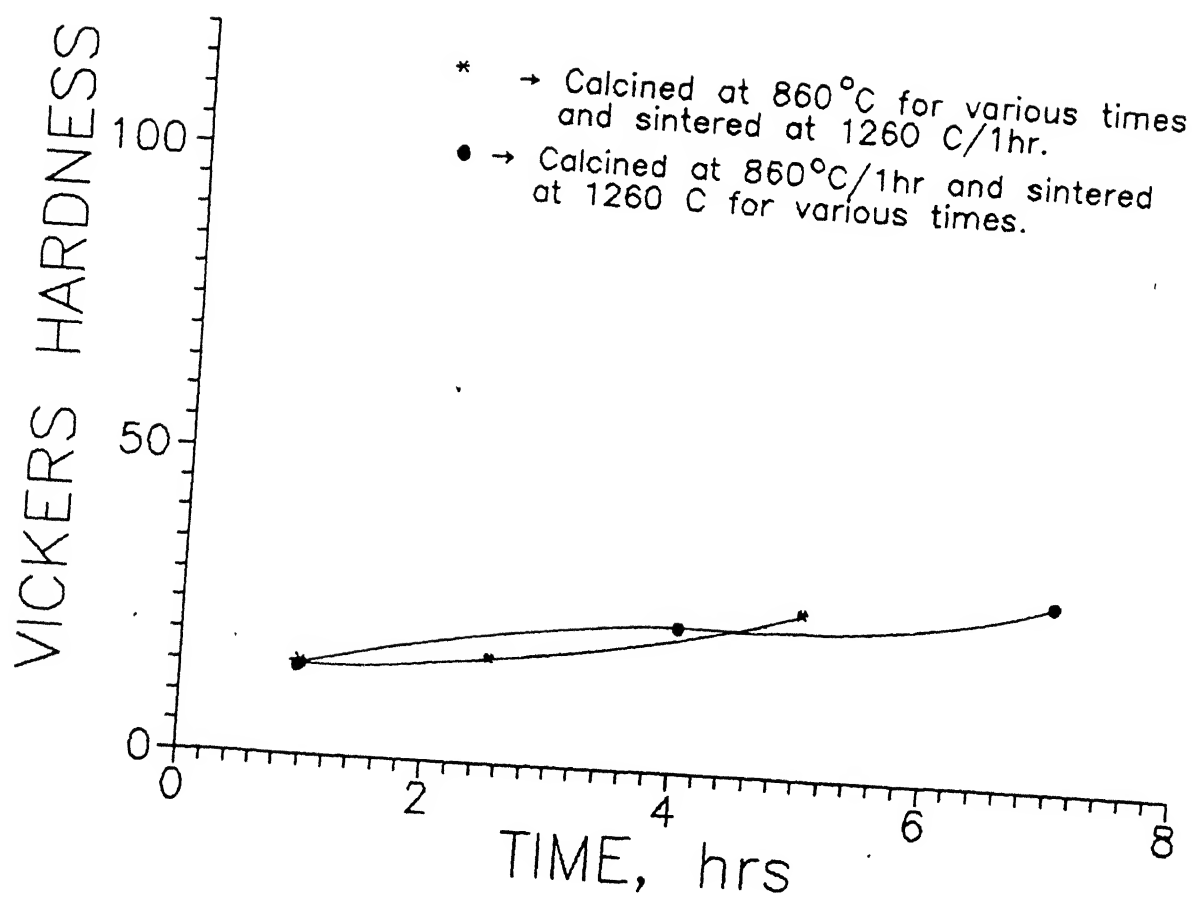


Fig. 6.25 Effect of calcination and sintering times on the Vickers hardness of  $\text{Pb}(\text{Zr}_{0.5}\text{Ti}_{0.5})\text{O}_3$ .

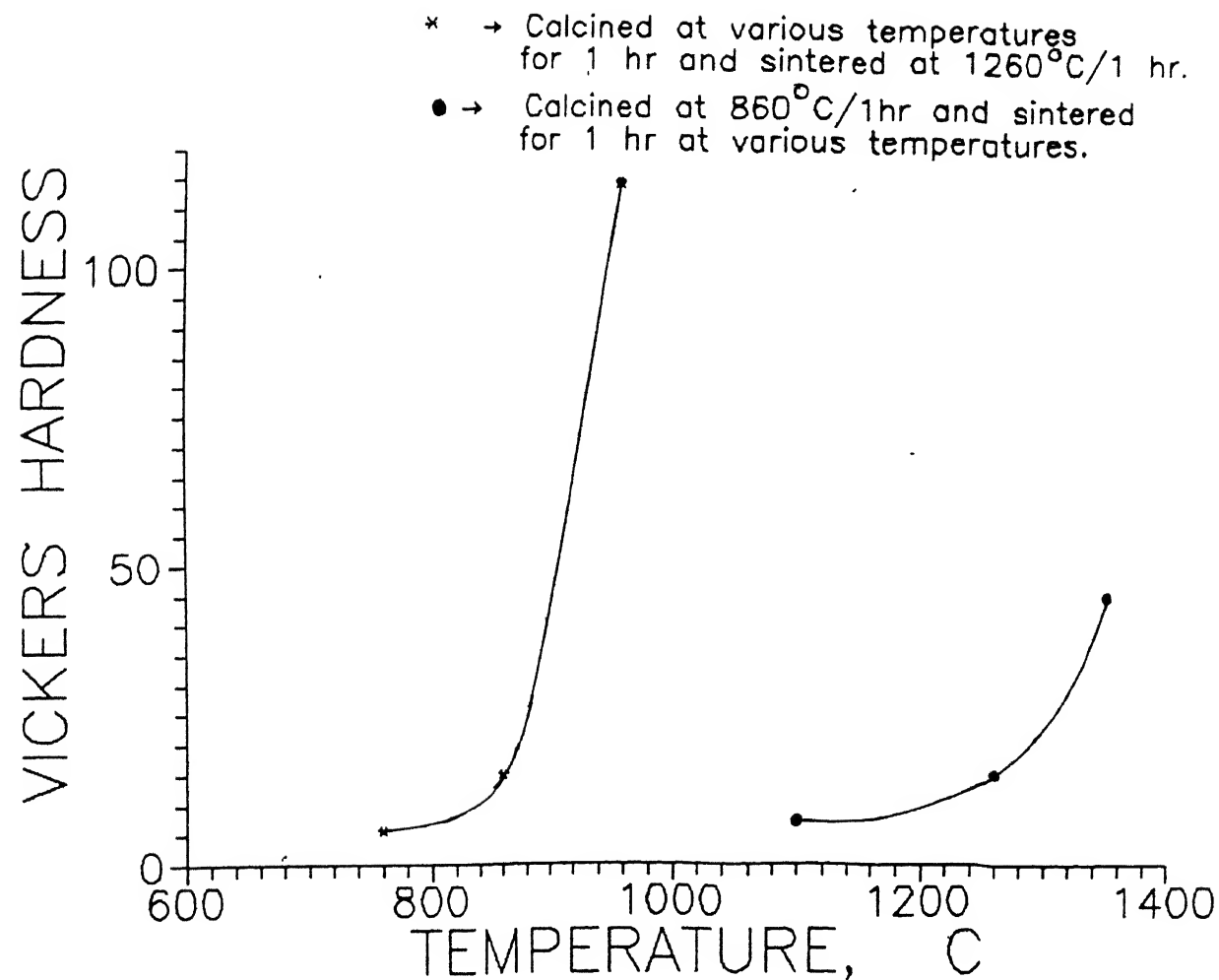


Fig. 6.26. Effect of calcination and sintering temperatures on the Vickers hardness of  $\text{Pb}(\text{Zr}_{0.5}\text{Ti}_{0.5})\text{O}_3$ .

The obtained results indicate that the tetragonal lattice parameter ' $a_T$ ' increases on increasing calcination temperature and time while ' $C_T$ ' remains more or less constant. The axial ratio  $C_T/a_T$  indicating the degree of tetragonality decreases with increasing calcination temperature and time together with the inhomogeneity. All these point out that homogenisation of the microcomposition indeed occurs in the lead-zirconate-titanate composition with  $x=0.5$ . The composition, fluctuation initially in the PZT solid solution lead to the formation of very small regions rich in either the tetragonal lead titanate phase or the rhombohedral lead zirconate phase. XRD plots reveal that some amount of free zirconia is also present in each of the sample sets A,B,C,D and E from which studies of the calcination effect are being made. Vasiliu et al [45] had prepared  $Pb (Zr_xTi_{1-x})O_3$  with  $x= 0.53$  and had found that when the sintering temperature was about  $1200^{\circ}C$ , the  $C_T/a_T$  ratio was 1.017. Considering that the composition used in the present work with  $x= 0.5$  is more towards the tetragonal side of the PZT phase diagram and the additional tetragonality induced by some of the unreacted zirconia, the measured  $C_T/a_T$  ratio between 1.026-1.033 is fairly consistent with that of [45]. On increasing the calcination temperature and time the enhanced diffusion effects on the Zr and Ti ions caused the tetragonal  $PbTiO_3$  rich microregion to become increasingly rich in Zr content leading to lower tetragonality. It is also

possible that more Zr from the unreacted  $\text{ZrO}_2$  entered the solid solution and decreased its tetragonality.

The results obtained on varying the sintering temperature cannot however be explained adequately by the microcomposition fluctuation theory. It is true that on increasing the sintering temperature of samples calcined at  $860^\circ\text{C}$  for 1 hr from  $1100^\circ\text{C}$  to  $1260^\circ\text{C}$  the tetragonality decreases as does the composition fluctuation. But increasing the sintering temperature to  $1350^\circ\text{C}$  also increases the inhomogeneity strangely. Increasing the sintering time for PZT compositions calcined under identical conditions produce similar results. The corresponding increase in tetragonality is a sufficient indicator that Zr ions in the form of  $\text{ZrO}_2$  precipitate have come out of the PZT solid solution. The relative intensity of the monoclinic  $\text{ZrO}_2$  peaks is greatest in samples F and G which had been sintered at  $1260^\circ\text{C}$  for 4 and 7 hours respectively and in sample I which was sintered at  $1350^\circ\text{C}$ .

A PZ+Z packing powder was used both during calcination and sintering to prevent PbO volatilisation from the PZT compacts. In spite of it some amount of PbO vaporisation did occur leading to the precipitation of monoclinic  $\text{ZrO}_2$ . This was probably because of the high  $\text{ZrO}_2$  content of the packing powder, which had a lower PbO vapour pressure compared to that of pure  $\text{PbZrO}_3$ . Besides, the packing powder was kept in a sagger at the base of the

alumina crucible, which was sealed at the top with alumina powder. PZT compacts, buried beneath the PZ+Z powder with a platinum foil separating the two would have been a better arrangement. However due to the unavailability of platinum foils the latter arrangement could not be resorted to.

The lower tetragonality of PZT sintered at  $1350^{\circ}\text{C}$  (Set I), in spite of the precipitation of  $\text{ZrO}_2$  is due to a possible solid state diffusion of Ti ions from the samples to the atmosphere powder through the porous alumina substrate (Fig. 5.1D). Kingion et al [52] had reported that diffusion of Ti ions from PZT compacts to the packing powder occur at relatively fast rates when no platinum foil is placed between the powder and the compact.

All the precipitated  $\text{ZrO}_2$  however did not come from the  $\text{PbZrO}_3$  rich regions in the PZT solid solution. A small amount, certainly came from the decomposition of the small amount of  $\text{PbZrO}_3$  which had formed at a lower temperature and which subsequently did not dissolve into the solid solution later due to the fast heating rate .

## 6.2 SEM Analysis:

Scanning electron micrographs were taken to see the distribution of the second phase  $\text{ZrO}_2$  particles on sintered lead zirconate titanate compacts. The secondary and back scattered electron images confirm the presence of



a certain amount of unreacted zirconia on PZT compacts which were calcined at  $760^{\circ}\text{C}$ . (Fig.6.3) . The micrograph of PZT calcined at  $860^{\circ}\text{C}$  (Fig. 6.4) indicates a lower amount of unreacted  $\text{ZrO}_2$  which means that a higher calcination temperature promotes a higher entry of Zr ions from the unreacted phase to the solid solution leading to decrease in tetragonality and inhomogeneity.

The amount of unreacted  $\text{ZrO}_2$  decreases when the sintering temperature increases from  $1100^{\circ}\text{C}$  to  $1260^{\circ}\text{C}$ , for samples calcined at  $860^{\circ}\text{C}$  for 1 hour ( Fig. 6.5a-b). Though it was expected that all the  $\text{ZrO}_2$  would have gone into the solid solution well before sintering temperatures were reached, its <sup>low</sup> reactivity coupled with the low calcination time prevented the dissolution. The sudden increase in  $\text{ZrO}_2$  content in the sample sintered at  $1350^{\circ}\text{C}$  is due to the  $\text{ZrO}_2$  precipitation (Fig. 6.5 c) as discussed earlier. This phenomena is again revealed in the micrographs of (Fig. 6.6 a,b) where the same  $\text{Pb}(\text{Zr,Ti})\text{O}_3$  composition sintered for 4 hours at  $1260^{\circ}\text{C}$  shows a greater amount of second phase  $\text{ZrO}_2$  than the one sintered for 1 hr.

Grain sizes of the  $\text{Pb}(\text{ZrTi})\text{O}_3$  compacts prepared under various calcination and sintering conditions were measured by the line intercept method. The results are given in Table 6.2 No significant change in grain size occur with change in calcination conditions. The most perceptable increase in grain diameter occur on increasing the sintering time as the micrographs in Fig. 6.7 indicate .

For better representation both micrographs have been selected from regions in the sample where the presence of a second phase is comparatively low. The uncontrolled grain growth of PZT sintered at  $1260^{\circ}\text{C}$  for 7 hours is due to the non introduction of any additive.

### 6.3 Piezoelectric Properties:

Results show that the average value of the piezoelectric strain coefficient,  $d_{33}$  increases on increasing the calcination temperature/ time or the sintering temperature/ time. It has been reported in literature the piezoelectric constants of lead zirconate titanate ceramics are maximum near the morphotropic phase boundary ( $x=0.535$ ). The composition in the present work was chosen close to the MPB, on the tetragonal side ( $x=0.50$ ).

When the tetragonality decreases the ' $d_{33}$ ' values got higher obviously because a **greater** amount of the sample mass has a chemical composition closer to that **at** the MPB. The comparatively high values of ' $d_{33}$ ' obtained for set G where inhomogeneity is maximum does not fall in line with this reasoning, however. It can be explained on the basis of microcracking of large grain sized specimens during poling. At the microcracks or separation at grain boundaries, space charge is created leading to higher  $d_{33}$  values [65].

While measuring the strain constant it was observed that all macroscopic regions in the same sample discs did not give the same value.

It was decided to observe then whether the microscopic composition fluctuation measured by XRD analysis could be related to deviations in the values of ' $d_{33}$ '. From the pellets of a particular sample set, discs were cut and prepared for ' $d_{33}$ ' measurement. The discs were then selected randomly. Probes were connected at various points of the same discs and for each point 5 readings were taken. After about 180 readings for each set, standard deviations of the recorded values were calculated.

Using the standard deviations of the  $d_{33}$  values and the composition fluctuation as two separate independent variables, the coefficient of rank correlation ' $r$ ' between them was calculated [66]. ' $r$ ' was found to equal 0.7574. Using standard correlation coefficient tables [66 pg. 268] we can say with 95% accuracy that a strong correlation exists between composition fluctuations and deviations in measured values of ' $d_{33}$ '.

6.3 ii) The dynamic test method for measurement of resonant and antiresonant frequencies which is described in Chapter 1 was tried in measuring the frequencies of the prepared samples using an impedance analyser.

Though the nature of the frequency reactance plot ( Fig. 6.8) was exactly similar to that obtained, in standard piezoelectric specimens manufactured by American Piezoceramics Inc., Mackeyville, PA 17750, USA, values of the mentioned frequencies could not be obtained because the reactance was negative at all frequencies. The reason can be attributed to the low dielectric constant, which lowered the capacitance of the prepared samples ( 100-500 PF at 100 KHZ) compared to the 1.3 nF at the same frequency for the standard. The low capacitance was caused because of a less than ideal microstructure in the specimens. The calcination time was very low ( 1 hr) for most of the samples and the heating rate was sufficiently high upto the sintering temperature. Besides each set of sample had phases other than lead-zirconate-titanate present also. Good dielectric constants are obtained in piezoceramics only when the material has dense uniform grains with minimum porosity and no second phase. As the aim was primarily to characterise the inhomogeneity in the specimens heating schedules conducive to producing an ideal microstructure were not selected.

#### 6.4 Density and Porosity : .

The density and porosity data provided in table 6.4 indicate that the density increases significantly on

increasing the calcination temperature from  $760^{\circ}\text{C}$  to  $960^{\circ}\text{C}$ . Although increasing calcination time increased the densities, the rise was not so sharp as when temperature was increased. Robinson et al [67] showed that about 3% of the reactants remained unreacted even after a temperature of  $770^{\circ}\text{C}$  was reached in lead-zirconate- titanate specimens. These unreacted materials affect the sinterability according to [47]. The results in table 6.4 corroborate the work of Buckner et al [47].

However increasing the sintering temperature from  $1100^{\circ}\text{C}$  to  $1260^{\circ}\text{C}$  did not cause any increase in density and a further increase to  $1350^{\circ}\text{C}$  actually lowered the density. It is possible that the pore size increased after an optimum sintering temperature was reached. Increasing the sintering time from 4 to 7 hrs. at  $1260^{\circ}\text{C}$  also increased the porosity. Both samples I and G have shown significant  $\text{ZrO}_2$  precipitation. Therefore during the sintering of these samples significant  $\text{PbO}$  vapourisation had occurred. As the rate of evaporation of  $\text{PbO}$  was greater than the rate of recondensation the porosity increased with a subsequent decrease of density.

#### 6.5 Vickers' Hardness:

The data provided in Table 6.5 indicate that Vickers hardness increases dramatically with increase in the calcination temperature. A higher calcination time also promotes a greater hardness value. The composition

used in the present work had  $x=0.5$ . From [28] it is understood that when  $x=0.5$ , the mechanical properties of  $\text{Pb}(\text{Zr}_x\text{Ti}_{1-x})\text{O}_3$  solid solution get improved. Increasing the calcination promotes higher homogeneity i.e. a greater percentage of the sample mass has composition closer to the desired value. The Vickers hardness is therefore higher for samples of greater homogeneity.

However it becomes non-realistic to attribute the entire change in hardness data to changes in the composition fluctuation values in these ceramics. The Vickers indenter produces a dent in the sample; the dent being caused by some amount of plastic flow. Plastic deformation in ceramics involves a complex process of dislocation movement and slippage along with pulverisation and rotation of the fragments as they continue to adhere to each other. A less calcined specimen with a corresponding greater amount of unreacted constituent and weaker bonding between grains therefore has lower hardness value.

Samples which were sintered differently showed some interesting Vickers hardness results. Samples I and G had very high composition fluctuations, yet they showed higher hardness. These samples also had lower densities compared to other specimens. It is speculated that  $\text{ZrO}_2$  precipitation increased the Vickers hardness values.

## CHAPTER 7

### CONCLUSIONS AND SUGGESTIONS FOR FURTHER WORK

#### Conclusions:

1. The composition fluctuation at the B sites of the perovskite lattice type  $\text{Pb}(\text{Zr}_x\text{Ti}_{1-x})\text{O}_3$  [ $x=0.5$ ] were measured by the X-ray line profile technique with high accuracy. Increased temperature and time of calcination decreased the inhomogeneity. Increasing the sintering temperature initially lowered the inhomogeneity. However samples sintered at high temperatures and for long periods in a  $\text{ZrO}_2$  rich PZ+Z atmosphere showed high composition fluctuation.
2. Particles of zirconia were found to precipitate out at prolonged sintering times and high temperatures due to removal of  $\text{PbO}$  through the vapour phase. While this contributed to an increased composition fluctuation at the B sites it may also have been responsible for high Vickers hardness in some samples.
3. The  $d_{33}$  values of PZT samples increased on increasing the calcination time or temperature during fabrication. Increased sintering time or temperatures during processing also led to higher values of  $d_{33}$  in the samples.

The fluctuations in the measured  $d_{33}$  values correlated well with composition fluctuations in these ceramics.

4. The Vickers hardness of PZT ceramics increased on increasing the calcination time or temperature and sintering time or temperature during processing. In most cases an increased inhomogeneity led to lower Vickers hardness value. Deviations were observed in samples where considerable  $ZrO_2$  precipitation occurred. It is possible that the  $ZrO_2$  precipitation promoted a strengthening effect.

#### Suggestions:

1. The line profile analysis can also be used to calculate the composition fluctuation at the A sites of the perovskite lattice, for example 'y' for the composition  $(Pb_yBa_{1-y})(Zr_xTi_{1-x})O_3$ . In this case the broadening of the 001 peaks must be measured.

2. In the present investigation it was observed that Zirconia precipitation in PZT ceramics did not lower the  $d_{33}$  values of specimens. This observation has got important implications and needs careful research. It may be possible to enhance the mechanical properties of these ceramics by controlled precipitation of  $ZrO_2$  without decreasing the piezoelectric properties.



## REFERENCES

1. W.Cady, Piezoelectricity, McGraw-Hill, New York (1946) .
2. C. Kittel, Phys. Rev., 82, 729-32 (1951).
3. F. Jona, and G. Shirane, Ferroelectric Crystals, Macmillan, New York.
4. F. Jona, G. Shirane, F. Mazzi, and R. Pepinsky, Phys. Rev., 105, 849-56 (1957).
5. B. Jaffe, W.R. Cook, and H. Jaffe, Piezoelectric Ceramics, Academic Press, London and New York. (1971).
6. F.S. Galasso, Structure, Properties and Preparation of Pervoskite type Compounds, Pergamon Press, London (1969).
7. H.D. Megaw, Acta Crystallographica, 5, 739-49 (1952); 7, 187-94 (1954).
8. H.G. Baerwald, Phys. Rev., 105, 480-86 (1957).
9. H. Jaffe, and D.A. Belincourt, Proceedings of the IEEE, 53, 1372-86 (1965).
10. D.A. Belincourt, M. Omolik, and H. Jaffe, Proceeding of the IRE , 48, 220-29 (1960).
11. S.A. Mabud, J. of Appl. Cryst 3 , 211-216 (1980).
12. L.Hanh, K. Uchino, and S. Nomura, Jap. J. of Appl. Phys., 17 (4), 637-641 (1978).
13. K. Kakegawa, J. Mohri, T. Takahashi, H. Yamamura, and S. Shirasaki, Solid St. Comm., 24, 769-772 (1977).
14. T. Kala, Phys. Stat Solidi(a), 277 (1983).
15. P. Ari-gur, and L. Benguigui, J. Phys. D: Appl. Phys., 8, 1856-1862 (1975).
16. Y. Matsuo, and H. Sasaki, J. Amer.Cerm. Soc, 48(6), 289-91 (1965).

17. S.S. Chandratreya, R.M. Fulrath, and J.A. Pask, J. Amer. Cer. Soc., 64(7), 422-425 (1981).
18. T. Ohno, M. Takahashi, and N. Tsubouchi, J. Jpn. Soc., Powder Metall, 20, 154-59 (1973).
19. T. Yomaguchi, S.H. Cho, M. Hakomori, and H. Kuno, Ceramurgia Int. 2[2], 76-80 (1976).
20. S. Venkatramani, and J.V. Biggers. Am. Ceram. Soc. Bull. 59(4) 462-66 (1980).
21. B.L. Hankey, and J.V. Biggers, J. Amer. Ceram. Soc., 64(12) C-172-C-173 (1981).
22. W.M. Sperry, Ph.D. Thesis, Rutgers University (1969).
23. G.R. Anstis, P. Chantikul, B.R. Lawn, and D.B. Marshall, J. Amer. Ceram Soc, 64(7), 533-538 (1981).
24. P. Chantikul, G.R. Anstis, B.R. Lawn and D.B. Marshall, J. Amer. Ceram. Soc, 64 (9), 539-543 (1981).
25. S.W. Freiman, D. Mulville, and P. Mast, J. Mater. Sci., 8, 1527 - 1533 (1973).
26. A.G. Evans, and E.A. Charles, J. Amer Ceram. Soc., 59 (7-8), 371-72 (1976).
27. M.C. Shaw, The Science of Hardness Testing and Its Research Application, 1,1-15, American Society of Metals, Metals Park, Ohio.
28. R.C. Pohanka, and P.L. Smith, Electronic Ceramics ed, L.M. Levinson, Marcel Dekker Inc. (1988), pp 44-145
29. R. Rice, and S.W. Freiman, J. Amer. Ceram. Soc., 64(6), 350-354 (1980).
30. Y. Matsuo, and H. Sasaki, J. Amer. Ceram. Soc., 49, 229 (1966)

31. K. Okazaki, Am. Ceram. Soc. Bull. 63(9), 1150-1152, 1157. (1984).
32. R.C. Pohanka, S.W. Freiman, and R.W. Rice, Ferroelectrics, 28, 337 (1980).
33. B. G. Koepke, and K.D. McHenry, Ferroelectrics, 28, 343-346 (1980).
34. R.W. Rice, S.W. Freiman, and P.F. Becher, J. Amer. Ceram. Soc., 64(6), 345-50.
35. C. Cm. Hu, S.W. Freiman, R.W. Rice, and J.J. Mecholsky, J. Mater. Sci., 13, 2659-70 (1978).
36. R.W. Rice, and R.C. Pohanka, J. Amer. Ceram. Soc., 62 (11-12) 559-663 (1979).
37. B.J. Hockey, J. Amer. Ceram. Soc., 54(5), 223 (1971).
38. B. Molnar, and R.W. Rice, Am. Ceram. Soc. Bull. 52 505-509, (1973).
39. G.H. Haertting, Ceramic Materials for Electronics; Processing, Properties, and Applications, ed R.C. Buchanan, 139-225, (1986), Marcel Dekker Inc.
40. V.M. McNamara, J. Can. Ceram. Soc., 34, 103-20(1965).
41. D.M. Roy, R.R. Neugonkar, T.P.O'Holleran, and R.Roy, Am. Ceram. Soc. Bull, 56 (11), 1023-24 (1977).
42. Yu.L. Trct'yakov, and V.A. Fokin, Izv. Akad. Nauk SSSR, Neorg Mater, 18(10), 1645-49 (1982).
43. K. Kakegawa, K. Watanabe, J. Mohri, H. Yamamura, and S. Shirasaki., J. Chem. Soc. Jpn 3', 413-416 (1975).
44. K. Kakegawa, K. Arai, Y. Sasaki, and T. Tomizawa, J. Amer. Ceram. Soc. 71(1) C-49-C-52 (1988).

45. F. Vasilan. P. Gr. Lucuta, and F. Constantinescu,  
Phys. Stat. Sol (a), 80, 637-642(1983).
46. P.Gr. Lucuta, Fl. Constantinescu, and D. Barb, J.  
Amer. Ceram Soc. 68(10) 533-37 (1985).
47. D.A. Duckner, and P.D. Wilcox, J.Amer. Ceram.Soc.,  
51(3), 218-222 (1972).
48. C.E. Baungartner, J. Amer. Ceram Soc., 71(7), C-35C-C-353  
(1988).
49. S.S. Chiang, M. Nishioka, R.M. Fulrath, and J.A. Pask,  
Amer. Ceram Soc. , Bulletin, 60(4), 484-489 (1981).
50. T.L. Hankey, and J.V. Biggers, J.Amer. Ceram Soc., 65(5),  
C-71 and C-75 (1982).
51. E. Sawaguchi, J. Phys. Soc. Jpn., 8, 615, (1953).
52. A.I. Kingon, and J.B. Clark, J. Amer. Ceram Soc., 66(4),  
253-256 (1983).
53. R.B. Atkin, and R.M. Fulrath, J.Amer. Ceram Soc. 54(5), 265-70  
(1971).
54. R.L. Holman, and R.M. Fulrath, J. Amer. Ceram. Soc. 55(4)  
192-97. (1972).
55. A.I. Kingon, and J.B. Clark, J. Amer. Cer. Soc., 66(4),  
256-260 (1983).
56. H.P. Klug, and L.E. Alexander, X-ray diffraction Procedures  
for Polycrystalline and Amorphous materials, Second  
Edition. (1974), John Wiley and Sons.
57. B.E. Warren, X-ray Diffraction Pg. 260-262 (1969),  
Addison-Wesley Publishing Company Inc.
58. F.W. Jones, Proc. Royal. Soc. (London), 166A, 16 (1938).

59. H. Ekstein, and S. Siegel, Acta Crystallographica, 2,99 (1949).
60. W. Ruland, Acta Crystallographica, 18,581 (1965).
61. L.E. Alexander, J. Appl. Physics, 25, 155m (1954).
62. B.D. Cullity, Elements of X-ray Diffraction, Second Edition Addison- Wesley Publishing Company INC, New York (1978).
63. Md. K. Akhtar, M.Tech. Thesis, I.I.T., Kanpur (1989).
64. K.H. Hardtl, and H. Rau, Solid State Comm 7 ; 41-45 (1969).
65. S.S. Chiang, R.M. Flurath, and J.A. Pask, J. Amer. Ceram. Soc. 64(10),C-141-C-143 (1981).
66. W.Volk, Applied Statistics for Engineers, Second Edition, McGraw-Hill Book Company (1969).
67. A.E. Robinson, and T.A. Joyce, Trans. Brit. Ceram. Soc. 61(2) 85-93 (1962).



## Measurement scheme for piezoelectric ceramics

Constants	Specimen and orientation	Measurement scheme, or calculation method
$\epsilon_{11}^r, k_{11}, d_{11}$	Bar plated on faces perpendicular to $Z$ .	Resonance measurements of the length extensional mode.
$\epsilon_{11}^p$	Bar plated on faces perpendicular to $Z$ .	From above, using $\epsilon_{11}^p = (1 - k_{11}^2)\epsilon_{11}^r$ .
$\epsilon_{33}^r$	Bar plated on faces perpendicular to $Z$ .	Measurement of low-frequency capacitance.
$\epsilon_{33}^p$	Bar poled along $Z$ , but with plating on faces perpendicular to $X$ .	Overtone of thickness shear mode of the same bar as above, but with signal field along $X$ .
$\epsilon_{11}^r$	Bar poled along $Z$ , but with plating on faces perpendicular to $X$ .	Measurement of low-frequency capacitance.
$\epsilon_{11}^p$	Bar poled along $Z$ , but with plating on faces perpendicular to $X$ .	Measurement of high-frequency (clamped) capacitance.
$k_{11}$	Bar poled along $Z$ , but with plating on faces perpendicular to $X$ .	$k_{11}^2 = 1 - \epsilon_{11}^p/\epsilon_{11}^r$ .
$\epsilon_{33}^p$	Bar poled along $Z$ , but with plating on faces perpendicular to $X$ .	$\epsilon_{33}^p = \epsilon_{33}^p/(1 - k_{11}^2)$ .
$\epsilon_{11}^r, \epsilon_{11}^p$	Square plate with faces perpendicular to $Z$ .	Fundamental resonance frequencies of the two contour-extensional modes of a square plate.
$\epsilon_{13}^p$	Square plate with faces perpendicular to $Z$ .	$\epsilon_{13}^p = \epsilon_{13}^p - k_{11}^2 \epsilon_{11}^p$ .
$\epsilon_{33}^p, d_{11}, k_{11}$	Bar plated on faces perpendicular to $Z$ , and with length along $Z$ .	Resonance measurements of length extensional mode.
$\epsilon_{33}^p$	Bar plated on faces perpendicular to $Z$ , and with length along $Z$ .	$\epsilon_{33}^p = \epsilon_{33}^p/(1 - k_{11}^2)$ .
$\epsilon_{11}^r, k_{11}, d_{11}$	Disk with faces perpendicular to $Z$ .	Resonance measurements of planar extensional mode.
$k_1$	Disk with faces perpendicular to $Z$ .	Resonance measurements of thickness extensional mode.
$d_1$	Disk with faces perpendicular to $Z$ .	Measurement of response to hydrostatic pressure.
$d_{11}$	Disk with faces perpendicular to $Z$ .	$d_{11} = d_1 - 2d_{11}$ .
$c_{33}^p$	Disk with faces perpendicular to $Z$ .	Overtone $f_p$ of thickness extensional mode.
$\epsilon_{11}^p$	Calculation.	Calculated from $c_{33}^p, \epsilon_{33}^p, \epsilon_{11}^p$ and $\epsilon_{33}^p$ .
$\epsilon_{13}^p$	Calculation.	$\epsilon_{13}^p = \epsilon_{13}^p + d_{11}d_{11}/\epsilon_{33}^p$ .
$\epsilon_{33}^p$	Calculation.	$\epsilon_{33}^p = \epsilon_{33}^p \left[ 1 - \frac{k_1^2 + k_{11}^2 + 2Ak_1k_{11}}{1 - A^2} \right]$ ,
		where
or		$A = \frac{\sqrt{2\epsilon_{13}^p}}{\sqrt{\epsilon_{33}^p(\epsilon_{11}^p + \epsilon_{13}^p)}}$
	Plate with faces perpendicular to $Z$ .	Measurement of high-frequency (clamped) capacitance.

Note:  $\epsilon_{13}$ ,  $\epsilon_{11}$  and  $d_{11}$  are generally negative.  $k_1$  is taken to be positive when  $d_{11}$  is negative.

## APPENDIX . 3

## Lattice Parameter Calculation from Peak Position:

Sample Set

Chemical composition -  $\text{Pb}(\text{Zr}_{0.5}\text{Ti}_{0.5})\text{O}_3$ 

Phases Present - Tetragonal, Rhombohedral

Peak Positions : Reflection  $(002)_T$   $(200)_T$   $(200)_R$   $(102)_R$ 

$2\theta$	43.72	45.22	44.38	49.92
-----------	-------	-------	-------	-------

For Tetragonal

$$\sin^2\theta = \frac{\lambda^2}{4} \left[ \frac{h^2+k^2}{a^2} + \frac{l^2}{c^2} \right]$$

 $(002)_T$ 

$$\sin^2\theta = \frac{\lambda^2}{4} \left[ \frac{4}{c^2} \right]$$

$$c_T = 4.1373\text{\AA}.$$

 $(200)_T$ 

$$\sin^2\theta = \frac{\lambda^2}{4} \left[ \frac{4}{a^2} \right]$$

$$a_T = 4.0069.$$

For Rhombohedral

If h,k,l are miller indicies in rhombohedral phase, then the corresponding miller indices in hexagonal phase is given as,

$$H = h-k, \quad K = k-l \quad L = h+k+l.$$



(200)<sub>R</sub>:

$$H=2, K=0, L=2.$$

$$\sin^2 \theta = \frac{2}{4} \left[ \frac{4(H^2 + HK + K^2)}{3a_H^2} + \frac{L^2}{C_H^2} \right]$$

$$0.2404267 = \frac{16}{3a_H^2} + \frac{4}{C_H^2}$$

(102)<sub>R</sub>

$$H=1, K=-2 \text{ and } L=3$$

$$0.3001452 = \frac{4}{a_H^2} + \frac{9}{C_H^2}$$

Solving these two equations, we get

$$C_H = 7.0762 \text{ \AA}$$

$$a_H = 5.7636 \text{ \AA}$$

$$\text{As } a_R = \frac{1}{3} (3a_H^2 + C_H^2)^{1/2}$$

$$= 4.0788 \text{ \AA}$$

$$\sin(a_R/2) = \frac{3}{2[3 + (\frac{C_H}{a_H})^2]^{1/2}}$$

$$= 89.9066^\circ$$

$$= 90^\circ - \alpha_R = 0.09336^\circ$$

# APPENDIX 4

## CALCULATION OF COMPOSITION FLUCTUATION IN SAMPLE B (CALCINED 860°C/ 1 hr, SENTERED 1260°C/ 1 hr.)

hkl	$2\theta$ (deg)	$d$ (deg)	$B_{\bullet}$ (deg)	$\frac{d}{B_0}$	$\frac{B}{B_0}$	$B$ (deg)	$\frac{b}{B}$	$\frac{B}{B}$	$B$ (deg)
(100) T	22.12	.06251	0.42	0.1488	0.9825	0.4127	0.4259	0.6616	0.2730
(200) T	45.00	0.1456	0.47	0.3095	0.4275	0.2016	0.4716	0.6093	0.2605
(220) T	65.82	0.2292	0.62	0.3697	0.8581	0.5320	0.2251	0.6646	0.3536

$\beta$ (deg)	$\beta$ (rad)	$\beta \cos \theta$	$\sin \theta$	Slope $ \Delta \frac{a_T}{a} $	$a_T$ (nm)	$\Delta a_T$ (nm)	$\Delta x$	Percentage composition fluctuation
0.2730	$4.7647 \times 10^{-3}$	$4.6762 \times 10^{-3}$	0.1918					
0.2605	$4.5466 \times 10^{-3}$	$4.1999 \times 10^{-3}$	0.3826	0.001312	0.4026	$5.2821 \times 10^{-4}$	0.0211	4.22
0.3536	$6.1715 \times 10^{-3}$	$5.1811 \times 10^{-3}$	0.5433					